Flow and Heat Transfer of Non-Newtonian Maxwell Fluid over a Stretchable Rotating Disk

By

Jawad Ahmed

Department of Mathematics
Quaid-i-Azam University
Islamabad, Pakistan
2020

Flow and Heat Transfer of Non-Newtonian Maxwell Fluid over a Stretchable Rotating Disk

By

Jawad Ahmed

Supervised By

Prof. Dr. Masood Khan

Department of Mathematics
Quaid-i-Azam University
Islamabad, Pakistan
2020

Flow and Heat Transfer of Non-Newtonian Maxwell Fluid over a Stretchable Rotating Disk

By

Jawad Ahmed

A DISSERTATION SUBMITTED IN THE PARTIAL FULFILLMENT OF THE REQUIREMENT FOR THE DEGREE OF

DOCTOR OF PHILOSOPHY

IN

MATHEMATICS

Supervised By

Prof. Dr. Masood Khan

Department of Mathematics
Quaid-i-Azam University
Islamabad, Pakistan
2020

Author's Declaration

I, **Jawad Ahmed** hereby state that my PhD thesis titled ''**Flow and Heat Transfer of Non-Newtonian Maxwell Fluid over a Stretchable Rotating Disk**'' is my own work and has not been submitted previously by me for taking any degree from the Quaid-i-Azam University Islamabad, Pakistan or anywhere else in the country/world.

At any time if my statement is found to be incorrect even after my graduate the university has the right to withdraw my PhD degree.

Name of Student: **Jawad Ahmed**

Date: **16-11-2020**

Plagiarism Undertaking

I solemnly declare that research work presented in the thesis titled "**Flow and Heat Transfer of Non-Newtonian Maxwell Fluid over a Stretchable Rotating Disk**" is solely my research work with no significant contribution from any other person. Small contribution/help wherever taken has been duly acknowledged and that complete thesis has been written by me.

I understand the zero tolerance policy of the HEC and **Quaid-i-Azam University, Islamabad** towards plagiarism. Therefore, I as an Author of the above titled thesis declare that no portion of my thesis has been plagiarized and any material used as reference is properly referred/cited.

I undertake that if I am found guilty of any formal plagiarism in the above titled thesis even afterward of PhD degree, the University reserves the rights to withdraw/revoke my PhD degree and that HEC and the University has the right to publish my name on the HEC/University Website on which names of students are placed who submitted plagiarized thesis.

Student/Author Signature: *Jawad Ahmed*

Name: **Jawad Ahmed**

Certificate of Approval

This is to certify that the research work presented in this thesis entitled **Flow and Heat Transfer of Non-Newtonian Maxwell Fluid over a Stretchable Rotating Disk** was conducted by Mr. **Jawad Ahmed** under the kind supervision of **Prof. Dr. Masood Khan**. No part of this thesis has been submitted anywhere else for any other degree. This thesis is submitted to the Department of Mathematics, Quaid-i-Azam University, Islamabad in partial fulfillment of the requirements for the degree of Doctor of Philosophy in field of Mathematics from Department of Mathematics, Quaid-i-Azam University Islamabad, Pakistan.

Student Name: **Jawad Ahmed**   Signature: _____

External committee:

a) **External Examiner 1**:   Signature: _____
   Name: **Dr. Muhammad Sajid**
   Designation: Professor
   Office Address: Department of Mathematics & Statistics, Faculty of Basic & Applied Sciences, International Islamic University, Islamabad.

b) **External Examiner 2**:   Signature: _____
   Name: **Dr. Rahmat Ellahi**
   Designation: Associate Professor
   Office Address: Department of Mathematics & Statistics, Faculty of Basic & Applied Sciences, International Islamic University, Islamabad.

c) **Internal Examiner**   Signature: _____
   Name: **Dr. Masood Khan**
   Designation: Professor
   Office Address: Department of Mathematics, QAU Islamabad.
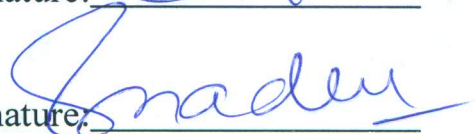
Supervisor Name: Signature: _____
Prof. Dr. Masood Khan

Name of Dean/ HOD   Signature: _____

Prof. Dr. Sohail Nadeem

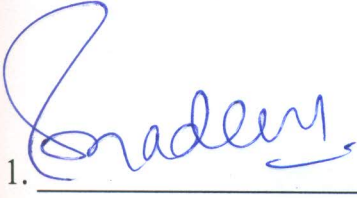# Flow and Heat Transfer of Non-Newtonian Maxwell Fluid over a Stretchable Rotating Disk
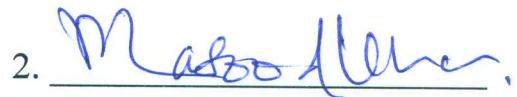
By

Jawad Ahmed

CERTIFICATE

A DISSERTATION SUBMITTED IN THE PARTIAL FULFILLMENT OF THE REQUIREMENTS FOR THE DEGREE OF

DOCTOR OF PHILOSOPHY IN MATHEMATICS

We accept this dissertation as conforming to the required standard

1. _____

Prof. Dr. Sohail Nadeem
(Chairman)

2. _____

Prof. Dr. Masood Khan
(Supervisor)

3. _____

Dr. Muhammad Sajid

Department of Mathematics & Statistics,
Faculty of Basic & Applied Sciences,
International Islamic University, Islamabad.

4. _____

Dr. Rahmat Ellahi

Department of Mathematics & Statistics,
Faculty of Basic & Applied Sciences,
International Islamic University, Islamabad.

Department of Mathematics
Quaid-i-Azam University
Islamabad, Pakistan
2020

Dedicated to

My beloved parents and my wife

Acknowledgement

In the name of **ALLAH**, the Most Glorious and the Most Merciful Lord, the creator and all praises to **ALLAH** who guide me in darkness, helps me in troubles and empowers me to view tentative blocks as stepping stones to the stars to reach the eventual stage with courage. I am nothing without my **ALLAH** but I can achieve everything with assistance. All of my reverence and commitment goes to our **Prophet Hazrat Muhammad SAWW** the source of humanity, kindness and guidance for the whole creatures and who advised the mankind to pursue knowledge from cradle to grave.

First and foremost I would like to express my special appreciation and thanks to my PhD advisor Prof. Dr. Masood Khan, you have been a tremendous mentor for me. I would like to thank you for encouraging my research and for allowing me to grow as a research scientist. Your advice on both research as well as on my career have been invaluable. In short, your tireless work, unique way of research and devotion to your profession cannot be expressed in words.

I would like to thank my mother and father, whose love, prayers and guidance are with me to follow my dreams. I am very thankful to my loving parents for their guidance, support and encouragement. I owe my heartiest gratitude for their assistance and never ending prayers for success. I highly commend the cooperative behavior of my brothers who endeavored for my edification and betterment. Most importantly, I wish to thank my loving supportive wife Saba Malik and my two wonderful children, Muhammad Ibrahim and Kulsoom Zahra, for sacrificing and helping in whatever way they could during this challenging period.

I gratefully acknowledge the Department of Mathematics, Quaid-i-Azam university Islamabad for this wonderful facilitation sources that made my PhD work possible. My sincere thanks also goes to chairman Department of Mathematics Prof. Dr. Sohail Nadeem, who provide me the opportunity for this milestone achievement.

Contents

Abstract

The rheology of complex fluids involving diverse non-Newtonian fluids has motivated investigations in this area. This is due to the fact that in industrial applications, complex fluids have become more and more important. On the other hand, swirling and/or rotating flows have fascinated researchers for centuries owing to their great technical and scientific importance. The research presented in this thesis is concerned with the swirling flows of a complex fluid. Particularly, in this work the governing equations of Maxwell fluid have been developed and explored numerically for a specific number of configurations.

The aim of this thesis is to develop and investigate the swirling flows for convective heat transport involving Maxwell fluids. The swirling and/or rotating systems are extensively used to model the flow and heat transfer associated with the internal-air systems of gas turbines, where disks rotate close to a rotating or a stationary surface. Further, these systems are used in chemical reactors, rotating-disk cleaners, transport engineering (automobile brakes), electro-chemistry (rotating-disk electrodes), etc. In view of such practical importance of these flows, in this thesis, we have focused on studying the numerical solutions of such flow problems arising in three different configurations of the rotating disk systems, viz. (i) flow over single stretchable rotating disk (under the influence of partial slip), (ii) thin film flow over a stretchable rotating disk, and (iii) flow between two stretchable rotating disks. These mentioned configurations have been investigated numerically for both steady and unsteady swirling flows along with heat transport phenomenon for Maxwell fluid model characterizing the relaxation time features. As the governing equations corresponding to these flows are highly nonlinear, and fully coupled which offer a significant level of complexity to get closed form analytic solutions. Thus, the popular and promising numerical techniques namely, Runge-Kutta Fehlberg (RK45), midrich scheme, and collation method bvp4c are adopted to acquire the numerical solutions of the considered problems.

In our study the behavior of the several influential parameters is studied by examining the velocity, temperature and concentration fields for a number of swirling flows of Maxwell fluid. Our study demonstrates that the impact of centrifugal force is perceived strongly in the vicinity of disk. It is noted that with boosting the disk rotation which in turn increase the radial and azimuthal velocity components result in a decrease in the axial velocity component. Moreover, the momentum boundary layer develops thinner by amplifying the Deborah number. Further, the rotation parameter plays a significant role in enhancing the fluid film thickness.

Chapter 1

Introduction

This chapter focuses on introduction of the thesis. Introduction comprises of a brief background of the physical problems and literature survey. Some basic physical laws, numerical methods and research objectives are also presented in this chapter.

1.1 Motivation

The classical Newton's model is unable to explain the flow of various fluids, for instance, large molecular weight polymers. Blood, lubricants, drilling mud, paints, slurries, nylon, toothpaste and colloids reveal a non-Newtonian behavior. We come across such type of fluids frequently in the plastics and chemical industry. Some effects, especially the rod-climbing, die swell when exiting a tube, drag reduction and self-siphoning can precisely be exhibited by these fluid models. To be more specific, the characteristics of non-Newtonian fluids are not categorized by the primitive theory of Navier-Stokes (NS). Usual non-Newtonian flow features comprise thixotropic (whose viscosity diminishes subject to the applied stress), pseudoplastic (whose viscosity is a reducing function of shear rate), dilatant (whose viscosity is an increasing function of shear rate), viscoelastic, rheopectic (whose viscosity rises subject to the applied stress) and visco-plastic. Some examples include clay, milk, some colloids, molten polystyrene, gelatin, rice/cornstarch suspensions,

etc. In a broader sense, the non-Newtonian fluids in existing literature are categorized in the subsequent kinds; the differential-type, the integral-type and the rate-type. In general, resultant differential equations verifying the flow of such liquids have greater order compared to the NS equations, and thus to get a unique solution, an additional condition is required.

To determine the impression of inhomogeneous flows, i.e., fluids whose material characteristics are a function of stress and shear rate, rate-type models are developed. The rate type fluids are reduced into the classical Navier-Stokes fluids as a special case. Such models are worthwhile in narrating the performance of geological fluids, biological fluids and edible goods owing to their intrinsic inhomogeneity. Lately, these fluids have attained extraordinary consideration. One of the simplest models was proposed by Maxwell [1] in 1867 due to its effectiveness for polymers allowing lower molecular weight. He addressed viscoelastic fluids that can incorporate the energy dissipation and have the remarkable capacity to save energy. Fluid stress relaxation features can be described by Maxwell fluid model. For concentrated polymer liquids, the relaxation-time parameter is chosen largely; otherwise, it is considered accordingly.

During last few years, the researchers have focused on the thermal features of Maxwell fluid motion due to its effectiveness for polymers allowing lower molecular weight. Fetecau and Fetecau [2] discussed the Maxwell fluid motion due to suddenly moved flat plate. They obtained the exact solution of the govering problem by using Laplace tramsformation. Tan and Xu [3] investigated the Maxwell fluid model to examine the viscoelastic property of the fluid with no-slip condition. The discrete inverse transform method was adopted to find the exact solution. Jamil and Fetecau [4] computed helical flows considering the Maxwell liquid. Here the flow was caused by the applied shear stress at plate. The analysis of heat transport in view of Cattaneo Christov model during the motion of Maxwell fluid was reported by Han *et al.* [5] . Mustafa [6] addressed analytically the motion of Maxwell fluid due to a rotating frame by utilizing the non-Fourier heat flux theory. Sui *et al.* [7] addressed heat and mass transfer mechanisms of upper-convected Maxwell nanofluid

over a stretched surface with Cattaneo-Christov double-diffusion and slip velocity. Afifya and Elgazery [8] focused on the influence of chemical reaction in the MHD boundary layer flow of Maxwell liquid over a stretched surface with nanoparticles. Liu and Guo [9] discussed the generalized Maxwell fluid during unsteady motion with coupling model. Cao *et al.* [10] studied the impression of heat source/sink on Maxwell nanoliquid during the stretched flow. Hsiao [11] reported a numerical study on a combined electrical MHD heat transfer thermal extrusion system in the radiative flow of Maxwell fluid with dissipation effects. Jusoh *et al.* [12] numerically investigated the flow and heat transfer of MHD three-dimensional Maxwell nanofluid over a permeable stretching/shrinking surface with convective boundary conditions.

A well-fascinated research area in fluid mechanics is perhaps the rotating disk geometry because of its evolving frequent applications in industry and engineering, including turbine system, jet motors, centrifugal filtration, electric-power generation, hard disks etc. For such a reason, the rotating disk liquid motion has been focused with enormous attention and been broadly scrutinized by several scientists since the grounding breaking study of Theodore Von Kármán [13] flow by virtue of the rotating disk. He studied the fluid movement caused by a rotating disk while away from the surface, the assumption of fluid at rest was considered. By adopting similarity transformations, the full system of Navier- Stokes equations was reduced into a system of nonlinear ordinary differential equations (ODEs). The mechanism by which flow field for von Kármán swirling flow arises can be better understand in the way that the fluid is considered at rest initially everywhere. When the disk starts rotating, then due to the no slip condition the development of boundary layer happened adjacent to rotating disk. The influence of centrifugal force produced due to rotation is to push the fluid radially outward inside the boundary layer. To balance radial flow, the fluid flows axially towards the disk surface fulfilling mass conservation law. Therefore inside the boundary layer, the velocity vector has the radial, tangential and axial components. The von Kármán swirling flow due to a rotating disk was investigated by many researchers with various perspectives considering different

fluid models. Shevchuk [14] studied the flow involving the rotating disk systems with heat and mass transfer charateristics. Turkyilmazoglu [15] discussed the MHD viscous fluid flow on rotating as well as stretching disk and concluded that near disk velocities increase dramatically with increasing rotation parameter. Ahmadpour and Sadeghy [16] obtained the exact solution in rotating Bingham flow and showed that by increasing the fluid's yield stress, the wall shear stress and the volumetric flow rate are decreased. The thermal features in flow caused by rotating disk of variable thickness were scrutinized by Xun *et al.* [17]. The von Kármán's transformation assisted to bring out the ordinary differential equations which were then solved with Runge–Kutta method coupled with multishooting technique. Mustafa *et al.* [18] carried out a numerical investigation on stagnation point in MHD three-dimensional flow induced by disk rotation in ferrofluid. Unsteady heat and mass transfer due to a rotating disk with the uniform magnetic field in the micropolar fluid flow of transient thermophoretic particle deposition were analyzed by Doh and Muthtamilselvan [19]. They concluded that with an increase of the magnetic parameter, micro-rotational tangential velocity decreases. The flow of second grade fluid by a rotating disk with the heat and mass transfer analysis was discussed by Hayat *et al.* [20]. The effects of homogeneous-heterogeneous reactions and heat generation/absorption were taken into consideration. Their result revealed that growing viscoelastic parameter causes to enhance the surface drag and rate of heat transport. In another paper, the same author (Hayat *et al.* [21]) drew attention towards the impact of entropy generation, heat source/sink and thermal radiations in Sisko fluid flow resulting from a rotating disk. Junaid *et al.* [22] considered the rotating disk configuration to explore the thermal features in dissipative nanofluid flow. The Brownian motion and thermophoresis aspects were studied by utilizing Buongiorno model. It was concluded that the magnetic field strength opposes the flow field in the radial, azimuthal and axial directions, respectively. The rotating disk flow in third grade nanofluid using Buongiorno model, chemical reaction and heat generation was investigated by Hayat *et al.* [23]. Their outcomes showed that with increasing Brownian motion, the temperature and concentration fields were increased.

Tabbasum and Mustafa [24] modeled the rough rotating disk geometry for Reiner-Rivlin fluid flow with partial slip and temperature jump conditions.

The process of developing a uniform liquid thin layer on a disk rotating horizontally is known as spin coating. This procedure is widely applicable in spin coating industry and has a lot of applications in various industry and technology sectors. To name a few; magnetic disk coatings, head lubricants, photoresist for defining patterns in microcircuit fabrication, flat screen display coatings, anti reflection coatings etc. The innovative idea on thin film flow over a rotating disk was firstly reported by Emslie *et al.* [25]. By considering the balance between viscous and centrifugal forces during the disk rotation process allow them to simplify the governing equations. They concluded that the film uniformity retains as it thin more and more continuously. In electronic industry, the applicability of the spin coating process was explored through experimental interpretations and theoretical investigations by Washo [26]. Jenekhe [27] and Flack *et al.* [28] extended the work of Emslie *et al.* [25] by incorporating the mass transfer and non-Newtonian fluid models. The resulted lubrication equations were tackled with finite difference scheme. Wang *et al.* [29] studied numerically the problem of liquid thin film developed over an accelerating rotating disk. The asymptotic solution in the case of values of accelerating, thin and thick parameters was also obtained. Andersson *et al.* [30] acquired both the numerical as well as asymptotic solution for rotating disk thin film flow with magnetic field properties. Kumari and Nath [31] discussed the liquid thin film in an unsteady magnetohydrodynamic flow occurs by disk rotation. The Navier–Stokes equations together with energy equation were transformed and the solution was obtained numerically and asymptotically. Their results showed that the film thickness and the surface shear stresses in the radial and tangential directions increase with accelerating disk for a fixed value of magnetic field. The phenomenon of non-uniform disk rotation with planar disk interface in two layers thin film flow with uniform transverse magnetic field was attempted by Dandapat and Singh [32].

Generally the system of disks rotating at different speeds is used to modeled the

air systems for internal cooling, for example, co-rotating turbines, rotor-stator system, contra-rotating disks etc. are the prominent applications. Therefore, with a view toward the significance of such type of rotating flows between two disks, numerous scientists and researchers are still involved in studying the rotating flow regimes features. The foremost investigation to study the fluid motion between double rotating disk was described by Batchelor [33] by revealing the extension of classical von Kármán classical flow problem for dual rotating disks. The fluid flow by dual rotating disks was considered by Lance and Rogers [34] with several conditions. Turkyilmazoglu [35] inquired the fluid motion within double rotating disks at a constant distance apart. The von Kármán similarity transformations assisted in bringing out the governing ODEs which are solved numerically. The MHD flow of nanofluid consisting of magnetite-Fe_3O_4 nanoparticles between two stretchable rotating disks was discussed by Hayat *et al.* [36]. The effects of temperature jump and velocity slip were considered and concluded that slip parameter causes to reduce the fluid tangential flow. In another article, Hayat *et al.* [37] studied the Jaffrey swirling flow in the gap of doubly rotating disks with the impact of homogeneous-heterogeneous reactions and thermal stratification. Recently, Das and Sahoo [38] focused their research in second grade liquid motion occupied the region among dual rotating disks.

Nanoscience and nanotechnologies are widely seen as having huge potential to bring benefits to many areas of research and applications like nanofluids and nanocomposites. Nowadays, study of nanofluids has been a subject of widespread interest in view of its improved thermal conductivity [39]. Nanofluids comprise of nanoparticles like Ag(silver), Cu(copper), CuO(copper oxide), Al_2O_3(alumina oxide), Fe_3O_4(iron oxide), CNT(carbon nanotube), TiO_2(titanium oxide), having sizes of $1-100$ nm suspended in the base fluids such as water, alcohol, carboxymethyl cellulose(CMC) etc. Some applications of nanoparticles were comprehensively reported by the several authors $[40-43]$. It has been shown through experiments that the addition of these ultrafine solid metal particles in base fluids brings out a significant improvement in the thermal conductivity. A large amount of research has been conducted to explore the nanofluids physical properties and has assisted

6

to better enlighten the basic mechanism of nanofluids. For instance, the nanometer-size particles suspension and their scattering and adhesion characteristics on the solid surfaces can give the materials having required optical and structural properties [44]. Nanofluids play a vital role in cooling process of inkjets and equipment [45, 46]. The usages of nanofluids are very wide in applications to the various fields such as, nuclear reactor cooling , electronics, aerospace, vehicles, cancer therapy power generation etc.

The term "nanofluids" was first used by Choi [47] in 1995, who revealed that nanofluids possess enhanced thermal conductivity and thermal transport features of common liquids can be improved with the suspension of nanoparticles. Buongiorno [48] built up a significant two phase investigation regarding the heat transfer mechanism in nanofluids flow by proposing the two-slip mechanisms, namely Brownian diffusion and thermophoresis. A model that characterizes the impacts of particle size, viscosity, volume fraction and thermal conductivity on heat transfer enhancement was proposed by Tiwari and Das [49]. A large number of problems related to nanofluids flow were studied by utilizing these two models. Kuznetsov and Nield [50] solved the problem of two-dimensional nanoliquid flow with natural convection past a vertical plate. Oztop and Nada [51] deliberated the nanoparticles fluid motion inside a rectangular enclosure along with heat transfer analysis. Lin and Jiang [52] explored numerically the effectiveness of nanofluids parameters in a circular rotating groove geometry.

The occurrence of heat transfer is very common natural phenomenon and it happens because of thermal difference between the objects or different parts of same body. Several researchers have been inspired to investigate its occurrence and existence. The classical law for heat conduction proposed by Fourier [53] is the basis to study the heat transfer characteristics in different conditions. On the other hand, the major drawback of this law is the contribution of parabolic energy equation which specifies that an initial disturbance is instantly affected by the system under consideration. In literature, this feature is physically unrealistic and is called "paradox of heat conduction". This situation is overwhelmed by numerous researchers by proposing the modifications in Fourier's law.

The revision in Fourier's model by introducing relaxation time heat flux was proposed by Cattaneo [54]. The hyperbolic energy equation is yielded through aforementioned modification which allows the heat transport via thermal waves propagation at finite speed. Cattaneo's modification was further improved by Christov [55] by introducing the thermal relaxation time with Oldroyd's upper-convected derivatives for the material-invariant formulation. In literature, this amendment is known as Cattaneo–Christov heat flux model. The uniqueness criterion for the solution of Cattaneo–Christov equation was evidenced by Ciarletta and Straughan [56]. The Cattaneo-Christov heat flux model on thermal characteristics in flow of viscoelastic fluid was studied by Han *et al.* [57]. A comprehensive explanation regarding the involved parameters was deliberated on flow and thermal behaviors and comparison was made between Fourier's law and the Cattaneo–Christov heat flux theory. Mustafa [58] applied the model of Cattaneo-Christov pertaining to thermal field to examine the flow of rotating Maxwell fluid. He concluded that relaxation time parameter has an inverse relation with fluid temperature. Hayat *et al.* [59, 60] studied the effectiveness of chemical reaction under various flow geometries. Nagendramma *et al.* [61] showed the characteristics of heat generation/absorption in chemically reactive flow of 3D Casson fluid by applying the Cattaneo-Christov heat flux theory. Some recent investigations in this direction can be seen in Refs. [62 − 67].

Chemical reactions are identified as homogeneous and heterogeneous processes relying on whether they arise in bulk of fluid (homogeneous) or happen on some catalytic surfaces (heterogeneous). Homogeneous and heterogeneous reactions occur in various chemical reacting systems including combustions, biochemical and catalysis. The boundary layer flow involving these reactions were studied by Chaudhary and Merkin [68]. In another paper, Merkin [69] used the idea of heterogeneous and homogeneous processes in flow of viscous liquid over a stretched surface. He examined the homogeneous reaction through cubic autocatalysis and considered first-order process for heterogeneous reaction. Khan and Pop [70] assessed the flow behavior in two dimensional stagnation point due to a permeable surface with homogeneous-heterogeneous reactions. Numerically equations were tackled

8

and showed that the flow characteristics were affected by the mass transfer parameter. Abbas *et al.* [71] studied the influence of homogeneous-heterogeneous reactions in the viscous fluid flow over a stretching/shrinking sheet. Khan *et al.* [72] reported numerically the three-dimensional Sisko fluid flow with the heterogeneous-homogeneous reactions and Cattaneo-Christov heat flux model. Rauf *et al.* [73] studied the Powel-Eyring fluid for chemically reactive flow with double diffusive Cattaneo-Christov heat and mass flux theories. Recently, Hashim *et al.* [74] made investigation on dual solutions on reactive Carreau fluid.

1.2   Basic Conservation Laws

The foundational axioms of fluid dynamics based on classical mechnains are the conservation laws, namely, conservation of mass, conservation of linear momentum and conservation of energy. They are expressed using the Reynolds transport theorem. The conservation laws may be applied to a region of the flow called a control volume(CV). These conservation laws are used to solve the fluid dynamics problems and may be written in integral or differential form.

1.2.1   The Mass Conservation

This law dictates that the mass is conserved within the control volume for constant density fluids. Thus the total mass leaving the system plus the mass accumulating within the control volume (CV) must be equal to the total mass entering to the control volume(CV). In mathematical form, we can write it as

$$\int_{\Omega(t)} \left(\frac{\partial \rho}{\partial t} + \nabla \cdot (\rho \mathbf{V}) \right) d\Omega = 0, \tag{1.1}$$

with the relation hold for any $\Omega(t)$. If we place an infinitesimal $\Omega(t)$ at every point in the flow, then the integrand must vanishes and results in the form of continuity equation

given by

$$\frac{\partial \rho}{\partial t} + \nabla \cdot (\rho \mathbf{V}) = 0, \tag{1.2}$$

which is embodiment of the mass conservation principle for fluid flow.

The steady flow version is

$$\nabla \cdot (\rho \mathbf{V}) = 0. \tag{1.3}$$

The density is assumed to be constant for an incompressible flow and thus results in

$$\nabla \cdot \mathbf{V} = 0. \tag{1.4}$$

1.2.2   The Momentum Conservation

The momentum conservation can be described by Newton's second law which states that time rate of change of momentum of a material volume is equal to sum of external forces acting on the volume. Mathematically,

$$\int_{\Omega(t)} \left(\frac{\partial \rho \mathbf{V}_\alpha}{\partial t} + (\rho \mathbf{V}_\alpha \mathbf{V}_\beta)_{,\beta} \right) d\Omega = \int_{\Omega(t)} (\rho \mathbf{B} + \boldsymbol{\tau}_{\alpha\beta,\beta}) \, d\Omega. \tag{1.5}$$

On simplification, we have

$$\frac{\partial \rho \mathbf{V}_\alpha}{\partial t} + (\rho \mathbf{V}_\alpha \mathbf{V}_\beta)_{,\beta} = \rho \mathbf{B} + \boldsymbol{\tau}_{\alpha\beta,\beta}. \tag{1.6}$$

Expressing in more convenient form

$$\rho \left[\frac{\partial \mathbf{V}}{\partial t} + (\mathbf{V} \cdot \nabla)\mathbf{V} \right] = div\boldsymbol{\tau} + \rho \mathbf{B}. \tag{1.7}$$

1.2.3 The Energy Conservation

The thermodynamics first law is the statement of this principle. Writing this mathematically as

$$\rho c_p \frac{dT}{dt} = \boldsymbol{\tau} \cdot \mathbf{L} - div\mathbf{q}, \tag{1.8}$$

where $\boldsymbol{\tau}$ is the Cauchy stress tensor, c_p the specific heat, $\mathbf{L}$ the velocity gradient, $\mathbf{q}$ the energy flux and T the fluid temperature. Further, the left hand side of Eq. (1.8) depicts the internal energy and $\boldsymbol{\tau} \cdot \mathbf{L}$ represents the viscous dissipation.

The energy flux can be defined as

$$\mathbf{q} = -k\nabla T, \tag{1.9}$$

where k being the fluid thermal conductivity.

1.2.4 The Concentration Conservation

According to this law, the rise in the total mass of species C in CV is equal to the net mass flow into CV plus the development rate of species in CV. In the presence of chemical reaction, it can be represented as

$$\frac{\partial C}{\partial t} + \mathbf{V} \cdot \nabla C = -\nabla \cdot \mathbf{j} + R, \tag{1.10}$$

where $\mathbf{j}$ is the normal flux and R the source/sink for concentration.

Usually $\mathbf{j}$ can be represented in terms of Fick's law given as

$$\mathbf{j} = -D\nabla C, \tag{1.11}$$

with D as mass diffusivity.

1.2.5 The Energy Conservation for Nanofluid

The energy conservation in case of an incompressible nanofluid is given by

$$\rho c_p \frac{dT}{dt} = -h_p \nabla \cdot \mathbf{j}_p - div\mathbf{q}_p. \tag{1.12}$$

where the terms $h_p, \mathbf{j}_p$ and $\mathbf{q}_p$ respectively, denote the specific enthalpy, diffusive mass flux and thermal flux for nanofluids.

The mathematical expressions for $\mathbf{j}_p$ and $\mathbf{q}_p$ are given as

$$\mathbf{q}_p = -k\nabla T + h_p \mathbf{j}_p, \tag{1.13}$$

$$\mathbf{j}_p = \rho_p D_B \nabla C - \rho_p D_T \frac{\nabla T}{T_\infty}, \tag{1.14}$$

where D_B and D_T, respectively, denote the Brownian motion and thermophoresis diffusion coefficients and ρ_p the nanofluid density.

In view of Eqs. (1.13) and (1.14), Eq. (1.12) simplifies into the following form

$$\rho c_p \frac{dT}{dt} = k\nabla^2 T + \rho_p c_p D_B \left(\frac{D_T}{D_B T_\infty} \nabla T \cdot \nabla T + \nabla C \cdot \nabla T \right). \tag{1.15}$$

1.2.6 The Concentration Conservation for Nanofluid

The nanofluid concentration equation is expressed in the following form

$$\frac{\partial C}{\partial t} + \mathbf{V} \cdot \nabla C = -\frac{1}{\rho_p} \nabla \cdot \mathbf{j}_p. \tag{1.16}$$

Incorporating Eq. (1.14), we arrive at

$$\frac{\partial C}{\partial t} + \mathbf{V} \cdot \nabla C = \frac{D_T}{T_\infty} \nabla^2 T + D_B \nabla^2 C. \tag{1.17}$$

1.3 The Rate Type Maxwell Fluid Model

Because of fluids diversity in nature, open literature contain numerous proposed fluid models. Among these a special attention is received by the rate type fluid models. Particularly, the rate type Maxwell model [1] has been utilized for those problems which shows the small dimensionless relaxation time. However, the relaxation time for concentrated polymeric liquids can be larger. It is well recognized by the Maxwell that some fluids have the capacity of storing energy and as a mean of dissipating energy. The stress relaxation characteristics have been considered in this subclass of rate Maxwell fluid model. This model is narrated with the following constitutive equation

$$\boldsymbol{\tau} + p\mathbf{I} - \mathbf{S} = 0, \tag{1.18}$$

where $\mathbf{I}$ portrays the identity tensor, p the fluid pressure and $\mathbf{S}$ the Maxwell fluid extra stress tensor defined by

$$\mu\mathbf{A}_1 = \left(1 + \lambda_1 \frac{D}{Dt}\right)\mathbf{S}, \tag{1.19}$$

where λ_1 is the fluid relaxation time, μ the dynamic viscosity, $\mathbf{A}_1 = \nabla\mathbf{V} + (\nabla\mathbf{V})^{t_1}$ with t_1 being transpose is the Rivlin-Ericksen tensor and $\frac{D}{Dt}$ the upper convected derivative defined by

$$\frac{D\mathbf{S}}{Dt} = \frac{\partial\mathbf{S}}{\partial t} + (\mathbf{V}\cdot\nabla)\mathbf{S} - (\nabla\mathbf{V})^{t_1}\cdot\mathbf{S} - \mathbf{S}\cdot(\nabla\mathbf{V}). \tag{1.20}$$

1.4 Solution Methodologies

1.4.1 Runge-Kutta-Fehlberg Method

Runge-Kutta Fehlberg (RK45-Fehlberg) method is the numerical algorithm to numerically integrate the initial value problems (IVPs). The German mathematician Erwin Fehlberg established this method being one of the large class of RK methods. However, RK45-Fehlberg is a mathematical approach with an error estimator of order $O(h^4)$ and $O(h^5)$,

respectively. In order to get the required accuracy during the computation of the results of the problem, two step sizes are used. A comparison is made at each mesh point related to large step size. If the required accuracy is not obtained then the step size h should be kept smaller as compared to the previous size. The process shall be continued till up to the desired accuracy. Once the results of two iterations are matched, then such approximation shall be accepted. However, if the results are more accurate than the required accuracy, then the step size shall be increased accordingly. Let an IVP is defined as

$$\frac{dy}{dx} = F(x, y), \quad y(x_0) = y_0. \tag{1.21}$$

The function $F(x, y)$ and the values x_0 and y_0 must be known in order to obtain the approximate continuous solution of Eq. (1.21). Thus the following six functional values are expressed as

$$W_1 = hF(x_j, \ y_j), \tag{1.22}$$

$$W_2 = hF\left(x_j + \frac{1}{4}h, \ y_j + \frac{1}{4}W_1\right), \tag{1.23}$$

$$W_3 = hF\left(x_j + \frac{3}{8}h, \ y_j + \frac{3}{32}W_1 + \frac{9}{32}W_2\right), \tag{1.24}$$

$$W_4 = hF\left(x_j + \frac{12}{13}h, \ y_j + \frac{1932}{2197}W_1 - \frac{7200}{2197}W_2 + \frac{7296}{2197}W_3\right), \tag{1.25}$$

$$W_5 = hF\left(x_j + h, \ y_j + \frac{439}{216}W_1 - 8W_2 + \frac{3680}{513}W_3 - \frac{845}{4104}W_4\right), \tag{1.26}$$

$$W_6 = hF\left(x_j + \frac{1}{2}h, \ y_j - \frac{8}{27}W_1 + 2W_2 - \frac{3544}{2565}W_3 + \frac{1859}{4104}W_4 - \frac{11}{40}W_5\right). \tag{1.27}$$

An approximate solution of the initial value problem (IVP) is furnished by a Runge-Kutta method of fourth order:

$$y_{j+1} = y_j + \frac{25}{216}W_1 + \frac{1408}{2565}W_3 + \frac{2197}{4101}W_4 - \frac{1}{5}W_5, \tag{1.28}$$

where the value of functions W_1, W_3, W_4, and W_5 are used. It is noted here that W_2 is not utilized in expression (1.28). Runge-Kutta method of fifth order is used for the better value of solution:

$$z_{j+1} = y_j + \frac{16}{135}W_1 + \frac{6656}{12825}W_3 + \frac{28561}{56430}W_4 - \frac{9}{50}W_5 + \frac{2}{55}W_6. \tag{1.29}$$

The optimal step size sh can be determined by multiplying the scalar s times the current step size h. The scalar s is

$$s = \left(\frac{tol\ h}{2\,|z_{j+1} - y_{j+1}|}\right)^{1/4} \approx 0.84 \left(\frac{tol\ h}{|z_{j+1} - y_{j+1}|}\right)^{1/4}, \tag{1.30}$$

where tol is the specified error control tolerance. To apply RK45-Fehlberg method, the higher order ODEs system is reduced into the first order ODEs system with the introduction of new variables defined by

$$F = x_1,\ F' = x_1' = x_2,\ F'' = x_2' = x_3,\ F''' = x_3', \tag{1.31}$$

with conditions

$$x_1(0) = F(0),\ x_2(0) = F'(0),\ x_2(\infty) = F'(\infty). \tag{1.32}$$

1.4.2   Bvp4c Matlab Builtin Scheme

An iteration-based technique bvp4c in Matlab is applied to solve the boundary value problem. The technique practices the Lobatto IIIa collocation formula, which produces a C1-continuous solution. The residuality of solutions controls the error and mesh selection. It is safe to say that this is a residual-type technique, whose efficiency relies on the initial guess provided as well as the boundary conditions. Shampine *et al.* [75] further discussed this technique in detail in his book.

To apply this scheme, the higher order ODEs are converted into a system of first order

ODEs. Bvp4c utilizes a collocation process for the solution of BVPs of the form

$$y'(x) = F(x, y, p_1), \quad a \le x \le b, \tag{1.33}$$

subject to following general boundary conditions

$$g(y(a), y(b), p_1) = 0, \tag{1.34}$$

where the vector p_1 is for the unknown parameters. It is well known that the $\tilde{S}(x)$ (approximate solution) is a continuous function comprising of polynomial of third degree on the subinterval $[x_n, x_{n+1}]$ of the mesh $a = x_0 < x_1 < ... < x_N = b$ satisfying the given conditions

$$g\left(\tilde{S}(a), \ \tilde{S}(b)\right) = 0, \tag{1.35}$$

and it also satisfies the differential equations (collocates) at both ends and the midpoint of each subinterval

$$\tilde{S}'(x_n) = f\left(x_n, \ \tilde{S}(x_n)\right), \tag{1.36}$$

$$\tilde{S}'((x_n + x_{n+1})/2) = f\left((x_n + x_{n+1})/2, \ \tilde{S}((x_n + x_{n+1})/2)\right), \tag{1.37}$$

$$\tilde{S}'(x_{n+1}) = f\left(x_{n+1}, \ \tilde{S}(x_{n+1})\right). \tag{1.38}$$

The fundamental technique of bvp4c, which is called Simpson's method, is famous and is perceived in a number of codes. It can be revealed that an isolated solution $y(x)$ will have approximation $\tilde{S}(x)$ of order four i.e, $\left\|y(x) - \tilde{S}_2(x)\right\| \le C^\star h^4$, where the the maximum of the step intervals $h_i = x_{i+1} - x_n$ is denoted with h and constant with $C^\star$. With bvp4c following the $\tilde{S}(x)$ for computation on a mesh, it can be evaluated for any x, or set of x values in $[a, b]$ with the bvpval function. The error estimation and mesh selection in this

routine are based on residual of $\tilde{S}(x)$ given by

$$r(x) = \tilde{S}'(x) - f\left(x, \ \tilde{S}(x)\right). \tag{1.39}$$

1.4.3 BVP Midrich Scheme (Midpoint Method)

The numerical solution of two point boundary value problem can also be computed on the Maple software with very helpful and efficient methods like traprich, trapdefer, midrich and middefer. The methods, traprich and trapdefer are based on trapezoid methods that use Richardson extrapolation enhancement or deferred correction enhancement, respectively. However the methods midrich and middefer are midpoint methods with the same enhancement schemes. The numerical assessment is executed with the help of Maple software. The mid point collocation method is described by the following general algorithm

$$y'(x) = F(x, y(x)), y(x_o) = y_o. \tag{1.40}$$

The expression for explicit midpoint method (modified Euler method) is given by

$$y_{n+1} = y_n + hF\left(x_n + \frac{h}{2}, \ y_n + \frac{h}{2}F(x_n, y_n)\right), \tag{1.41}$$

where h denotes the step size and $x_n = x_o + nh$. The implicit midpoint method strategy is expressed as

$$y_{n+1} = y_n + hF\left(x_n + \frac{h}{2}, \ y_n + \frac{1}{2}(y_n, y_{n+1})\right), \quad n = 0, 1, 2, ... \tag{1.42}$$

The mid point procedure has local error of order $O(h^3)$ and the global error is of $O(h^2)$ at each step. The algorithm error decay faster as $h \to 0$ with more computational intensive and the solution shall be more stable.

1.5 Scope of Research

As mentioned earlier in this chapter, understanding of rotating-disk boundary-layer flow is important from both scientific and industrial point of views. The overall objective of the present thesis is to develop the mathematical formulation and investigation of the behavior of a non-Newtonian Maxwell fluid in the laminar boundary layer created on a stretchable rotating disk. The effects of the heat and mass transfer mechanisms in non-Newtonian flows are of special interest. Further, the study gives more insights into the various physical aspects of the rotating-disk geometry like thin film flow and flow between two rotating disks. In order to demonstrate the outcomes physically, several numerical procedures assist to carry out the numerical simulation of the flow problems. Thus, this study embarks on the following objectives:

- Mathematical formulations of Maxwell fluid flow over a stretchable rotating disk, thin film over a rotating disk as well as flow between two stretchable rotating disks are carried out.

- The study further analyzes the heat and mass species transfer with the focus on the various physical effects.

- The physical interpretation of governing rotating disk flow problems are assessed graphically viz numerical computations.

1.6 Contribution in Thesis

The present work attempts to investigate the flow and heat transfer of non-Newtonian Maxwell fluid caused by stretchable rotating disk. The diverse efforts have been devoted to model and explore Maxwell fluid flow due to stretchable rotating disk, unsteady thin film flow as well as the flow confined between the gaps of two stretchable rotating disks. Indeed, prior to this work there had been no existing studies concerning the flow of Maxwell fluid model in the regime of stretchable rotating disk. Gaining a better understanding of flow

of Maxwell fluid in the presence of heat and mass transfer with various situations will allow better control of such flow situation.

Thus, the development of mathematical models and their numerical simulations under various physical aspects are the foremost contributions of this thesis. The substantial contents of this thesis have already been published. The work in this thesis is organized as follows:

Chapter 2: This chapter is devoted to the mathematical formulation of three dimensional steady flow of Maxwell nanofluid caused by stretching as well as rotating disk. The novel aspects of thermophoresis and Brownian motion features are examined by utilizing Buongiorno's model. Further, the impact of linear Rosseland radiation on heat transfer characteristics is studied. The systems of partial differential equations for Maxwell fluid flow are formulated by using the concept of boundary layer approximations. The problem is non-dimensionalized by way of von Karaman hypothesis. Bvp midrich scheme is used to numerically integrate the resultant nonlinear problem. The outcomes have been reported in "*Chines Journal of Physics, 62 (2019) 86-98*".

Chapter 3: This chapter investigates the efficiency of the Cattaneov-Christov model during the steady motion of Maxwell fluid affected by stretchable rotating disk. Further, the mechanism of heat transfer is controlled with the influence of temperature dependent thermal conductivity. The mass transfer phenomenon is observed under the action of first order chemical reaction. The governing nonlinear ODEs are solved numerically with Runge-Kutta-Fehlberg (RKF45) procedure using Maple software. The validity of numerical outcomes is also presented through comparison tables. The graphical discussion on the profiles of temperature, velocity and concentration is demonstrated against arising parameters. The findings of this chapter are published in "*Journal of the Brazilian Society of Mechanical Sciences and Engineering, 40 (2018) 573*".

Chapter 4: The objective of this chapter is to study the heat and mass transfer characteristics of magnetohydrodynamic (MHD) Maxwell fluid flow exposed to convectively heated rotating disk. The aspects of homogeneous-heterogeneous reactions and nonlin-

ear radiations are also examined. Appropriate conversion variables assisted to bring out the nonlinear system of ODEs. The numerically approach namely Runge-Kutta-Felberg (RKF45) is implemented to solve the system of equations. The significant features of this study are published in "***Applied Mathematics and Mechanics (English Edition) 39(9) (2018) 1295-1310***".

Chapter 5: The inspiration of this chapter is to understand motion of Maxwell nano-liquid near the stagnation-point region subject to shrinking/stretching rotating disk inspired with revised Buongiorno's nanofluid model. A built-in numerical procedure bvp4c is implemented for the numerical integration of the governing nonlinear problem. The numerical data for the Nusselt number is displayed in table. The role of pertinent parameters on the flow, temperature and concentration fields have been portrayed in detail. The contents pertaining to this chapter can be seen in "***Journal of Molecular Liquids 287 (2019) 110853***".

Chapter 6: In this chapter, our main concern is the development of mathematical model for unsteady thin film flow of Maxwell nanofluid by considering the magnetic field and non-linear thermal radiation. The motion of thin film is produced due to both radial stretching and rotating velocities of the disk. Further, the tabular and graphical analysis are observed by solving the arising problem for film thickness, Nusselt and Sherwood numbers, velocity, temperature and concentration distributions. The analysis done in this chapter is published in "***Physics Letters A, 383 (2019) 1300-1305***".

Chapter 7: The transient thin film motion of a Maxwell nanofluid influenced by magnetic field, nonlinear thermal radiations, Joule heating and Arrhenius chemical reaction with activation energy is studied theoretically in this chapter. The resultant equations have been tackled numerically with bvp4c scheme. The main observations are revealed in "***Applied Physics A: Materials Science and Processing, 125 (2019) 161***".

Chapter 8: The single rotating disk configuration is extended in this chapter to the case where Maxwell fluid is flowing between the gap of two axially stretchable rotating disks. Two disparate situations, such as, when the direction of rotation of both disks is

same as well as opposite are addressed. A builtin numerical scheme bvp4c is executed to obtain the solution of governing nonlinear problem. The graphical and tabular features of the velocity, pressure, temperature and concentration fields are demonstrated against influential parameters. The consequences presented in this chapter are published in "***Journal of the Brazilian Society of Mechanical Sciences and Engineering, 41 (2019) 97***".

Chapter 9: This chapter explores the effectiveness of homogenous-heterogeneous chemical reactions in Maxwell fluid flow between two coaxially stretchable rotating disks. Further, the thermal energy mechanism is carried out with Cattaneo-Christov model. A finite difference algorithm based scheme, namely bvp4c is implemented for numerical results. The effects of active parameters are portrayed graphically for the radial, axial and azimuthal velocities as well as temperature and concentration fields. The highlights of this chapter are published in "***Journal of Thermal Analysis and Calorimetry, 139 (2020) 3185-3195***".

Chapter 10: The main findings of this thesis as well as suggestions for further work are presented in this chapter.

Chapter 2

Von Kármán Swirling Flow of Maxwell Nanofluid over a Rotating Disk

In this chapter, the classical von Kármán swirling flow problem due to a rotating disk is modeled and studied for the rate type Maxwell nanofluid together with heat and mass transfer mechanisms. The model under consideration predicts the relaxation time characteristics. The novel aspects of thermophoresis and Brownian motion features are investigated by employing an innovative Buongiorno's model. The analysis further explores the impact of linear Rosseland radiation on heat transfer characteristics. The dimensionless form of system of ODEs is derived through similarity approach adopted by von Kármán. The system of equations is then integrated numerically in domain $[0,\infty)$ by using bvp midrich scheme in Maple software. The obtained results intimate that a higher rotation raises the radial and angular velocity components. Moreover, the nano-particles concentration enhances with Brownian motion parameter. Further, the heat transfer rate at the disk surface diminishes with thermophoresis parameter. The achieved numerical computations of velocity profile, Nusselt number and surface drag coefficient are matched in limiting cases with previously published literature and an outstanding agreement is observed.

2.1 Rheological Development

Without body forces, the relations for mass conservation, linear momentum, energy and nano-particles concentration are

$$\nabla \cdot \mathbf{V} = 0, \tag{2.1}$$

$$\rho \frac{d\mathbf{V}}{dt} = \nabla \cdot \mathbf{S} - \nabla p, \tag{2.2}$$

$$\frac{dT}{dt} = \tau^* D_B \left(\frac{D_T}{D_B T_\infty} \nabla T \cdot \nabla T + \nabla C \cdot \nabla T \right) + \alpha \nabla^2 T, \tag{2.3}$$

$$\frac{dC}{dt} = \frac{D_T}{T_\infty} \nabla^2 T + D_B \nabla^2 C, \tag{2.4}$$

where $(C, T, \mathbf{V})$ denote the fluid concentration, fluid temperature and velocity vector, respectively, p the liquid pressure, D_T the thermophoretic diffusion coefficient, ρ the liquid density, α the thermal diffusivity, τ^* the ratio of effective heat capacities, D_B the Brownian diffusion coefficient and $\mathbf{S}$ the Maxwell fluid extra stress tensor expressed by

$$\mathbf{S} + \lambda_1 \frac{D\mathbf{S}}{Dt} = \mu \mathbf{A}_1. \tag{2.5}$$

For steady three dimensional axisymmetric flow, velocity, temperature, concentration and the stress fields are assumed as

$$\mathbf{V} = [u(r, z), \ v(r, z), \ w(r, z)], \ T = T(r, z), \ C = C(r, z), \ \mathbf{S} = \mathbf{S}(r, z), \tag{2.6}$$

where (u, v, w) symbolize the velocity components in the radial, azimuthal and axial directions, respectively. Having in mind the expressions (2.5) and (2.6), Eqs. (1.1) and (1.2) take the following compact forms

$$\frac{\partial}{\partial z}(w) + \frac{1}{r}\frac{\partial}{\partial r}(ru) = 0, \tag{2.7}$$

$$u\frac{\partial u}{\partial r} - \frac{v^2}{r} + w\frac{\partial u}{\partial z} = \nu \left(\frac{\partial^2 w}{\partial r \partial z} + \frac{2}{r}\frac{\partial u}{\partial r} - \frac{2u}{r^2} + \frac{\partial^2 u}{\partial z^2} + 2\frac{\partial^2 u}{\partial r^2} \right) - \frac{1}{\rho}\frac{\partial p}{\partial r}$$

$$- \lambda_1 \left(u^2 \frac{\partial^2 u}{\partial r^2} + w^2 \frac{\partial^2 u}{\partial z^2} + 2uw\frac{\partial^2 u}{\partial r \partial z} - \frac{2uv}{r}\frac{\partial v}{\partial r} - \frac{2vw}{r}\frac{\partial v}{\partial z} + \frac{uv^2}{r^2} + \frac{v^2}{r}\frac{\partial u}{\partial r} \right), \tag{2.8}$$

$$u\frac{\partial v}{\partial r} + w\frac{\partial v}{\partial z} + \frac{uv}{r} = \nu\left(\frac{\partial^2 v}{\partial r^2} - \frac{v}{r^2} + \frac{1}{r}\frac{\partial v}{\partial r} + \frac{\partial^2 v}{\partial z^2}\right)$$

$$-\lambda_1\left(u^2\frac{\partial^2 v}{\partial r^2} + w^2\frac{\partial^2 v}{\partial z^2} + 2uw\frac{\partial^2 v}{\partial r\partial z} + \frac{2uv}{r}\frac{\partial u}{\partial r} + \frac{2vw}{r}\frac{\partial u}{\partial z} - \frac{2u^2v}{r^2} - \frac{v^3}{r^2} + \frac{v^2}{r}\frac{\partial v}{\partial r}\right), \qquad (2.9)$$

$$u\frac{\partial w}{\partial r} + w\frac{\partial w}{\partial z} = -\frac{1}{\rho}\frac{\partial p}{\partial z} + \nu\left(\frac{\partial^2 u}{\partial r\partial z} + \frac{\partial^2 w}{\partial r^2} + \frac{1}{r}\frac{\partial u}{\partial z} + \frac{1}{r}\frac{\partial w}{\partial r} + 2\frac{\partial^2 w}{\partial z^2}\right)$$

$$-\lambda_1\left(u^2\frac{\partial^2 w}{\partial r^2} + 2uw\frac{\partial^2 w}{\partial r\partial z} + w^2\frac{\partial^2 w}{\partial z^2} + \frac{v^2}{r}\frac{\partial w}{\partial r}\right). \qquad (2.10)$$

Presenting dimensionless variables

$$[u^*,\ v^*,\ w^*] = \left[\frac{u}{R\Omega}, \frac{v}{R\Omega}, \frac{w}{\delta\Omega}\right],\ [\ r^*,\ z^*,\ T^*,\ p^*] = \left[\frac{r}{R}, \frac{z}{\delta}, \frac{T-T_\infty}{T_\infty}, \frac{p}{\rho\left(R\Omega\right)^2}\right]. \qquad (2.11)$$

In view of these non-dimensional variables, we can write the continuity and momentum equations as:

$$\frac{\partial}{\partial z^*}\left(w^*\right) + \frac{1}{r^*}\frac{\partial}{\partial r^*}\left(r^*u^*\right) = 0, \qquad (2.12)$$

$$u^*\frac{\partial u^*}{\partial r^*} - \frac{v^{*2}}{r^*} + w^*\frac{\partial u^*}{\partial z^*} = \frac{1}{Re}\left(2\frac{\partial^2 u^*}{\partial r^{*2}} + \frac{\partial^2 w^*}{\partial r^*\partial z^*} + \frac{2}{r^*}\frac{\partial u^*}{\partial r^*} - \frac{2u^*}{r^{*2}}\right) - \frac{\partial p^*}{\partial r^*}$$

$$+ \frac{1}{Re}\left(\frac{R}{\delta}\right)^2\frac{\partial^2 u^*}{\partial z^{*2}} - \lambda_1\Omega\left(u^{*2}\frac{\partial^2 u^*}{\partial r^{*2}} + w^{*2}\frac{\partial^2 u^*}{\partial z^{*2}} + 2u^*w^*\frac{\partial^2 u^*}{\partial r^*\partial z^*}\right.$$

$$\left. - \frac{2u^*v^*}{r^*}\frac{\partial v^*}{\partial r^*} - \frac{2v^*w^*}{r^*}\frac{\partial v^*}{\partial z^*} + \frac{u^*v^{*2}}{r^{*2}} + \frac{v^{*2}}{r^*}\frac{\partial u^*}{\partial r^*}\right), \qquad (2.13)$$

$$u^*\frac{\partial v^*}{\partial r^*} + w^*\frac{\partial v^*}{\partial z^*} + \frac{u^*v^*}{r^*} = \frac{1}{Re}\left(\frac{\partial^2 v^*}{\partial r^{*2}} - \frac{v^*}{r^{*2}} + \frac{1}{r^*}\frac{\partial v^*}{\partial r^*}\right)$$

$$+ \frac{1}{Re}\left(\frac{R}{\delta}\right)^2\left(\frac{\partial^2 v^*}{\partial z^{*2}}\right) - \lambda_1\Omega\left(u^{*2}\frac{\partial^2 v^*}{\partial r^{*2}} + w^{*2}\frac{\partial^2 v^*}{\partial z^{*2}} + 2u^*w^*\frac{\partial^2 v^*}{\partial r^*\partial z^*}\right.$$

$$\left. + \frac{2u^*v^*}{r^*}\frac{\partial u^*}{\partial r^*} + \frac{2v^*w^*}{r^*}\frac{\partial u^*}{\partial z^*} - \frac{2u^{*2}v^*}{r^{*2}} - \frac{v^{*3}}{r^{*2}} + \frac{v^{*2}}{r^*}\frac{\partial v^*}{\partial r^*}\right), \qquad (2.14)$$

$$\frac{1}{\left(R/\delta\right)^2}\left(u^*\frac{\partial w^*}{\partial r^*} + w^*\frac{\partial w^*}{\partial z^*}\right) = -\frac{\partial p^*}{\partial z^*} + \frac{1}{Re}\frac{1}{\left(R/\delta\right)^2}\left(\frac{\partial^2 w^*}{\partial r^{*2}} + \frac{1}{r^*}\frac{\partial w^*}{\partial r^*}\right)$$

$$+ \frac{1}{Re}\left(\frac{1}{r^*}\frac{\partial u^*}{\partial z^*} + 2\frac{\partial^2 w^*}{\partial z^{*2}} + \frac{\partial^2 u^*}{\partial r^*\partial z^*}\right)$$

24

$$-\lambda_1 \Omega \frac{1}{(R/\delta)^2}\left(2u^*w^*\frac{\partial^2 w^*}{\partial r^*\partial z^*} + w^{*2}\frac{\partial^2 w^*}{\partial z^{*2}} + \frac{v^{*2}}{r^*}\frac{\partial w^*}{\partial r^*} + u^{*2}\frac{\partial^2 w^*}{\partial r^{*2}}\right). \tag{2.15}$$

Within the boundary layer, the inertial and viscous terms have the same order of magnitude and these terms give us

$$\frac{1}{Re}\left(\frac{R}{\delta}\right)^2 = O(1), \quad \left(\frac{\delta}{R}\right)^2 = O\left(\frac{1}{Re}\right), \quad \lambda_1\Omega = O(1). \tag{2.16}$$

Here $Re = \frac{R^2\Omega}{\nu}$ is the Reynolds number. In limit $Re \to \infty$, Eqs. (2.12) to (2.15) asymptotically become

$$\frac{\partial}{\partial z^*}(w^*) + \frac{1}{r^*}\frac{\partial}{\partial r^*}(r^*u^*) = 0, \tag{2.17}$$

$$u^*\frac{\partial u^*}{\partial r^*} - \frac{v^{*2}}{r^*} + w^*\frac{\partial u^*}{\partial z^*} = -\lambda_1\Omega\left(u^{*2}\frac{\partial^2 u^*}{\partial r^{*2}} + w^{*2}\frac{\partial^2 u^*}{\partial z^{*2}}\right.$$
$$+2u^*w^*\frac{\partial^2 u^*}{\partial r^*\partial z^*} - \frac{2u^*v^*}{r^*}\frac{\partial v^*}{\partial r^*} - \frac{2v^*w^*}{r^*}\frac{\partial v^*}{\partial z^*} + \frac{u^*v^{*2}}{r^{*2}} + \frac{v^{*2}}{r^*}\frac{\partial u^*}{\partial r^*}\left.\right) - \frac{\partial p^*}{\partial r^*} + \frac{\partial^2 u^*}{\partial z^{*2}}, \tag{2.18}$$

$$u^*\frac{\partial v^*}{\partial r^*} + w^*\frac{\partial v^*}{\partial z^*} + \frac{u^*v^*}{r^*} = \frac{\partial^2 v^*}{\partial z^{*2}} - \lambda_1\Omega\left(u^{*2}\frac{\partial^2 v^*}{\partial r^{*2}} + w^{*2}\frac{\partial^2 v^*}{\partial z^{*2}}\right.$$
$$+2u^*w^*\frac{\partial^2 v^*}{\partial r^*\partial z^*} + \frac{2u^*v^*}{r^*}\frac{\partial u^*}{\partial r^*} + \frac{2v^*w^*}{r^*}\frac{\partial u^*}{\partial z^*} - \frac{2u^{*2}v^*}{r^{*2}} - \frac{v^{*3}}{r^{*2}} + \frac{v^{*2}}{r^*}\frac{\partial v^*}{\partial r^*}\left.\right), \tag{2.19}$$

$$0 = -\frac{\partial p^*}{\partial z^*}. \tag{2.20}$$

The above equations in dimensional form then can be written as

$$\frac{\partial}{\partial z}(w) + \frac{1}{r}\frac{\partial}{\partial r}(ru) = 0, \tag{2.21}$$

$$u\frac{\partial u}{\partial r} + w\frac{\partial u}{\partial z} - \frac{v^2}{r} = -\frac{1}{\rho}\frac{\partial p}{\partial r} + \nu\frac{\partial^2 u}{\partial z^2}$$
$$-\lambda_1\left(u^2\frac{\partial^2 u}{\partial r^2} + w^2\frac{\partial^2 u}{\partial z^2} + 2uw\frac{\partial^2 u}{\partial r\partial z} - \frac{2uv}{r}\frac{\partial v}{\partial r} - \frac{2vw}{r}\frac{\partial v}{\partial z} + \frac{uv^2}{r^2} + \frac{v^2}{r}\frac{\partial u}{\partial r}\right), \tag{2.22}$$

$$u\frac{\partial v}{\partial r} + w\frac{\partial v}{\partial z} + \frac{uv}{r} = \nu\frac{\partial^2 v}{\partial z^2}$$

25

$$-\lambda_1 \left(u^2 \frac{\partial^2 v}{\partial r^2} - \frac{v^3}{r^2} + \frac{v^2}{r}\frac{\partial v}{\partial r} + w^2 \frac{\partial^2 v}{\partial z^2} + 2uw\frac{\partial^2 v}{\partial r \partial z} + \frac{2uv}{r}\frac{\partial u}{\partial r} + \frac{2vw}{r}\frac{\partial u}{\partial z} - \frac{2u^2 v}{r^2} \right), \qquad (2.23)$$

$$0 = -\frac{\partial p}{\partial z}, \qquad (2.24)$$

where $\nu = \frac{\mu}{\rho}$ denotes the kinematic viscosity.

2.2 Model Sketch
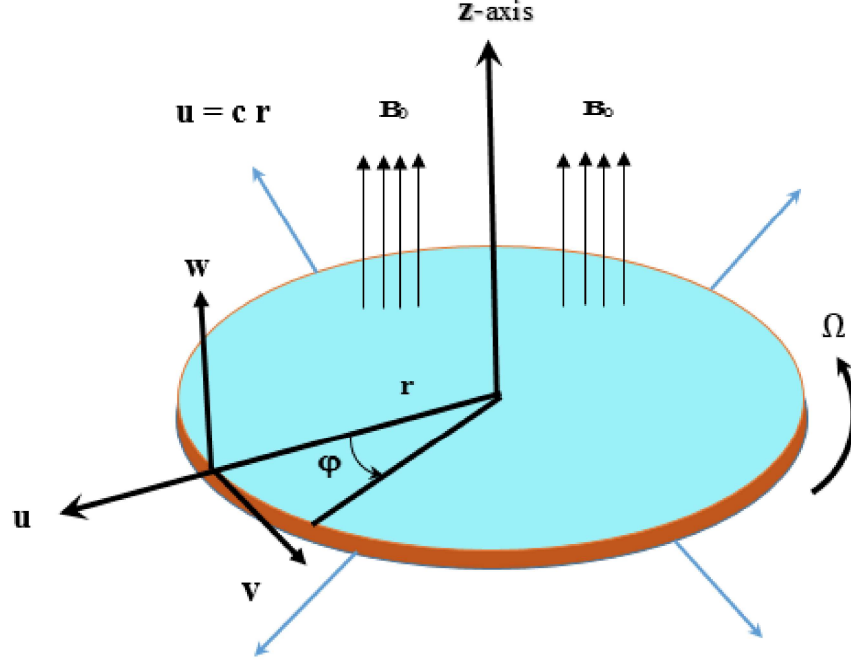
Fig. 2.1: Schematic of the physical system.

2.3 Problem Formulation

We have investigated a non-Newtonian incompressible Maxwell nano-fluid model over a rotating disk geometry. The transport phenomena for mass and heat with radiations are explored by considering the nanoparticles. The disk has the stretching velocity $u = cr$ as well as rotating velocity $v = \Omega r$ in the radial and tangential directions, respectively. To better understand the flow configuration, cylindrical coordinates system (r, φ, z) is considered as shown in **Fig. 2.1**. At disk surface, the nano-particles concentration C_w and temperature T_w are maintained constants, while the ambient values are C_∞ and T_∞.

The above stated assumptions lead to a set of equations describing momentum, energy, and concentration conservation for the Maxwell nano-fluid flow given by

$$\frac{\partial}{\partial z}(w) + \frac{1}{r}\frac{\partial}{\partial r}(ru) = 0, \tag{2.25}$$

27

$$u\frac{\partial u}{\partial r} - \frac{v^2}{r} + w\frac{\partial u}{\partial z} = \nu\frac{\partial^2 u}{\partial z^2} - \lambda_1 \left[\begin{array}{c} u^2\frac{\partial^2 u}{\partial r^2} + w^2\frac{\partial^2 u}{\partial z^2} + 2uw\frac{\partial^2 u}{\partial r\partial z} - \frac{2uv}{r}\frac{\partial v}{\partial r} \\ -\frac{2vw}{r}\frac{\partial v}{\partial z} + \frac{uv^2}{r^2} + \frac{v^2}{r}\frac{\partial u}{\partial r} \end{array} \right], \tag{2.26}$$

$$u\frac{\partial v}{\partial r} + w\frac{\partial v}{\partial z} + \frac{uv}{r} = \nu\frac{\partial^2 v}{\partial z^2} - \lambda_1 \left[\begin{array}{c} u^2\frac{\partial^2 v}{\partial r^2} + w^2\frac{\partial^2 v}{\partial z^2} + 2uw\frac{\partial^2 v}{\partial r\partial z} + \frac{2uv}{r}\frac{\partial u}{\partial r} \\ +\frac{2vw}{r}\frac{\partial u}{\partial z} - \frac{2u^2 v}{r^2} - \frac{v^3}{r^2} + \frac{v^2}{r}\frac{\partial v}{\partial r} \end{array} \right], \tag{2.27}$$

$$u\frac{\partial T}{\partial r} + w\frac{\partial T}{\partial z} = D_B\tau^* \left[\frac{D_T}{D_B T_\infty}\left(\frac{\partial T}{\partial z}\right)^2 + \frac{\partial T}{\partial z}\frac{\partial C}{\partial z} \right] + \alpha\left(\frac{\partial^2 T}{\partial z^2}\right) - \frac{1}{\rho c_p}\frac{\partial q_{\text{rad}}}{\partial z}, \tag{2.28}$$

$$u\frac{\partial C}{\partial r} + w\frac{\partial C}{\partial z} = \frac{D_T}{T_\infty}\left(D_B\frac{T_\infty}{D_T}\frac{\partial^2 C}{\partial z^2} + \frac{\partial^2 T}{\partial z^2}\right). \tag{2.29}$$

Utilization of the Rosseland approximation leads to simplest form of radiative heat flux as

$$q_{\text{rad}} = -\frac{4\sigma^*}{3k^*}\frac{\partial T^4}{\partial z}, \tag{2.30}$$

where k^* and σ^* are the mean absorption and Stephan-Boltzmann constants, respectively. Expressing T^4 in Taylor series about T_∞ and omitting the terms for higher-order to obtain

$$q_{rad} = -\frac{16\sigma^* T_\infty^3}{3k^*}\frac{\partial T}{\partial z}. \tag{2.31}$$

Using Eq. (2.31), Eq. (2.28) can be expressed as

$$u\frac{\partial T}{\partial r} + w\frac{\partial T}{\partial z} = D_B\tau^* \left[\frac{D_T}{D_B T_\infty}\left(\frac{\partial T}{\partial z}\right)^2 + \frac{\partial T}{\partial z}\frac{\partial C}{\partial z} \right] + \left(\alpha + \frac{16\sigma^* T_\infty^3}{3\rho c_p k^*}\right)\frac{\partial^2 T}{\partial z^2}. \tag{2.32}$$

2.3.1 Boundary Conditions

The physical boundary conditions of the stated problem are:

(i) On the disk surface ($z = 0$)

$$(u, v, w) = (cr, \Omega r, 0), \;\; (T, C) = (T_w, C_w). \tag{2.33}$$

(ii) Matching with quiescent free stream ($z \to \infty$)

$$(u, v) = (0, 0), \;\; (T, C) = (T_\infty, C_\infty), \tag{2.34}$$

where c represents the stretching rate and Ω the swirling rate

2.3.2 Similarity Analysis

Introducing the following similarity transformations for conversion of governing continuity, momentum, energy and nano-particles concentration equations into ordinary differential equations

$$(u, v, w, \eta) = \left(crF(\eta),\ crG(\eta),\ \sqrt{cv}H(\eta),\ \sqrt{\frac{c}{v}}z\right),\ \theta(\eta) = \frac{T - T_\infty}{T_w - T_\infty},\ \phi(\eta) = \frac{C - C_\infty}{C_w - C_\infty}.$$
(2.35)

Utilizing the above transformations, Eqs. $(2.25 - 2.27)$, (2.29) and $(2.32 - 2.34)$ can be simplified as

$$H' + 2F = 0,$$
(2.36)

$$F^2 - G^2 + HF' = F'' - \beta_1 \left(H^2 F'' + 2FF'H - 2HGG'\right),$$
(2.37)

$$2FG + HG' = G'' - \beta_1 \left(H^2 G'' + 2FG'H + 2HGF'\right),$$
(2.38)

$$(1 + Rd)\theta'' + \Pr\theta' \left(Nb\phi' - H\right) + \Pr Nt\ \phi'^2 = 0,$$
(2.39)

$$\phi'' + \frac{Nt}{Nb}\theta'' - ScH\phi' = 0,$$
(2.40)

with conditions

$$[(F, G, H, \theta, \phi) = (1, \omega, 0, 1, 1)\ \text{at}\ \eta = 0],$$

$$[(F, G, \theta, \phi) = (0, 0, 0, 0)\ \text{as}\ \eta \to \infty],$$
(2.41)

where the rotation strength parameter is denoted by $\omega \left(= \frac{\Omega}{c}\right)$ which measures the ratio of swirl to stretch rates. Further, Pr the Prandtl number, Nt the thermophoresis parameter, β_1 is the Deborah number, Rd the radiation parameter, Sc the Schmidt number and Nb the Brownian parameter. These dimensionless quantities are defined as

$$\Pr = \frac{v}{\alpha},\ Nt = \frac{\tau^* D_T \left(T_w - T_\infty\right)}{T_\infty v},\ \beta_1 = \lambda_1 c,\ Rd = \frac{16\sigma^* T_\infty^3}{3kk^*},$$

$$Sc = \frac{v}{D_B},\ Nb = \frac{\tau^* D_B \left(C_w - C_\infty\right)}{v}.$$
(2.42)

2.3.3 Physical Quantities

The engineering interest quantities are the Nusselt number Nu_r and the Sherwood number Sh_r. Physically Nu_r is the surface heat transfer rate and Sh_r implies the mass transfer rate of the nano-particles concentration. The mathematical expressions of these quantities are given as

$$Nu_r = -\left[1 + \frac{16\sigma^* T_\infty^3}{3\rho c_p k^*}\right] \frac{R}{(T_w - T_\infty)} \left(\frac{\partial T}{\partial z}\right)|_{z=0}, \tag{2.43}$$

$$Sh_r = -\frac{R}{(C_w - C_\infty)} \left(\frac{\partial C}{\partial z}\right)|_{z=0}, \tag{2.44}$$

Where R is the characteristic radius.

The dimensionless expressions are given by

$$Re^{-1/2}\, Nu_r = -\left(1 + Rd\right)\theta'(0),\ \ Re^{-1/2}\, Sh_r = -\phi'(0), \tag{2.45}$$

where $Re = \left(\frac{R^2 c}{\nu}\right)$ is the Reynolds number.

2.4 Results and Discussion

The differential system in Eqs. (2.36) to (2.40) with conditions (2.41) are highly non-linear in nature. Therefore, we employ the numerical technique called bvp midrich scheme which calls midpoint collocation method. The validity of our numerical outcomes is proved by making a comparison in limiting cases with previously publish works. The numerical results of $(G'(0), F'(0))$ (radial and angular skin frictions) and $\theta'(0)$ (Nusselt number) are shown in **tables (2.1-2.5)**. The values are compared with those reported by Turkyilmazoglu [15], Mustafa *et al.* [18] and Shevchuk [14]. A tremendous similarity is perceived here with the consequences of the aforesaid authors.

In this section, velocity components namely radial $F(\eta)$, angular $G(\eta)$ and axial $H(\eta)$, temperature $\theta(\eta)$ and concentration $\phi(\eta)$ fields are examined for the parameters governed from the emerging mathematical formulation. The parameters include rotation parameter ω, Deborah number β_1, Prandlt number Pr, radiation parameter Rd, thermophoresis parameter Nt, Brownian motion parameter Nb and Schmidt number Sc. The influence of these parameters are

graphically shown through **Figs**. **(2.2-2.8)**. The quantities of physical interest include the skin friction and Nusselt number and are computed in **tables** (**1-5**).

For fixed Deborah number $\beta_1 = 0.1$, the curves of radial $F(\eta)$, azimuthal $G(\eta)$ and axial velocity $H(\eta)$ at various estimation of rotation parameter ω are sketched in **Figs. 2.2(a-d)**. The case $\omega = 0$ implies pure stretching without rotation. The radial velocity component in **Fig. 2.2(a)** is observed in an increasing manner with growing rotation velocity. As ω enhances the stretching rate c becomes smaller than the rotation rate Ω, so near the disk surface the radial velocity component excel its stretching rate. Physically boosting the rotation, the centrifugal force becomes stronger which exert pressure on the fluid particles to move in radial direction. The radial velocity is seen in a decreasing trend as we move away from the disk surface which indicates that the influence of centrifugal force is limited at the neighborhood of the disk. Therefore, within this argument growing rotation also increases the angular velocity component $G(\eta)$ which is shown in **Fig. 2.2(b)**. The axial velocity component $H(\eta)$ reveals a diminishing trend with rotation parameter ω. The main reason behind is that stronger rotation rate augments the pushing of fluid particles in radial direction and this deficiency is compensated by the particles that are drawn towards the disk in the negative axial direction due to disk stretching as portrayed in **Fig. 2.2(c)**. **Fig. 2.2(d)** depicts that without dissipation and Joule heating, $\theta(\eta)$ decreases with increasing rotation rate which leads to heat loss.

The effect of Deborah number β_1 , at specific value of rotation ω, versus velocity components is presented in **Figs**. **2.3(a-c)**. For the value $\beta_1 = 0$, the Maxwell fluid model reduces to viscous fluid. Physically, Deborah number β_1 is defined as the ratio between material relaxation time and material observation time. If $\beta_1 > 1.0$, elastic effects are dominant while for $\beta_1 < 0.5$, viscous effects prevail. For any values other than these two extremes, the material would depict viscoelastic behavior. So, an increasing value of Deborah number β_1 indicates larger the stress relaxation thus observation time become shorter. Hence solid like response is exhibited by the fluid. Therefore the fluid motion is retarded by enhancing the Deborah number which in turn decreases the radial $F(\eta)$, axial $H(\eta)$, and azimuthal $G(\eta)$ velocity components. The corresponding momentum boundary layer become thinner with Deborah number.

Fig. 2.4(a) summarizes the impact of Prandtl number Pr on temperature distribution $\theta(\eta)$. Here the some typical Prandtl number $Pr(= 0.71)$ is assumed for air, and $Pr(= 6.1 - 6.8)$

for water. For growing Prandtl number implies the reduction in temperature and the heat penetration depth becomes thinner. By definition, Prandtl number Pr approximates the ratio between momentum to thermal diffisivities. The reason can be attributed for rising value of Prandtl number yields the enhancement in momentum diffusivity. The upshot of Rd for $\theta(\eta)$ is inspected through **Fig. 4(b)**. It reveals that the $\theta(\eta)$ rises due to increasing radiation parameter Rd. Greater value of radiations implies more heat gained by the fluid which causes temperature enhancement.

The immpression of parameters Nt and Nb on temperature $\theta(\eta)$ is scrutinized in **Figs. 2.5(a,b)**. Here the liquid concentration and temperature boost up with flourishing the Nt. In fact, thermal conductivity becomes more strengthen with larger thermophoresis parameter. So the role of thermophoresis parameter is critical in placing the nano-particles over rotating disk flow. The uplifting Brownian motion leads to boost temperature distribution. It is the characteristic of the Brownian motion of fluid particles that they move in an unsystematic way which produced more heat and thus causes an enhancement in liquid temperature.

Figs. 2.6(a,b) are drawn to visualize the strength of Nt and Nb on $\phi(\eta)$ field. It is evident from **Fig. 2.6(a)** that when the value of thermophoretic parameter intensifies from $Nt = 0.0$ to $Nt = 0.9$, the concentration boundary layer $\phi(\eta)$ raises. **Fig. 2.6(b)** illustrates the characteristics of Bownian motion Nb for nano-particles concentration field. We observe that the concentration profile decays with growing Brownian motion parameter. Physically, when we boost the Brownian motion parameter then the nano-particles get more speed in various directions, so an increase in random motion of liquid particles lead to a decrease in concentration boundary layer thickness.

The impact of varying Schmidt number Sc on concentration profile $\phi(\eta)$ is visualized in **Fig. 2.7**. We observe a declination in nano-particles concentration $\phi(\eta)$ and associated boundary layer thickness. Actually, Sc has inverse relationship with the Brownian parameter Nb. So an increasing value of Sc leads to small diffusivity and thus the concentration asymptotically decreases.

Fig. 2.8(a) depicts the variation in Nusselt number $-\theta'(0)$ versus Brownian motion parameter Nb for various values of Nt when $Rd = 1.0$ and 1.5. The heat transfer rate is found to be decayed by gradual estimation of Nt. Further, the enhancing radiations promotes the heat

transfer rate. **Fig. 2.8(b)** captured the mass transfer rate (Sherwood number) $-\phi'(0)$ againts Nt for different Schmidt number Sc when $Nb = 0.2$ and 0.4. It reveals that the elevating Sc yields the higher rate of mass transfer. It is remarkable that rising parameters Nb and Nb encourage the mass transfer rate.

Table 2.1: A comparison for $F'(0)$ of several ω when $Pr = 1$ and $Nb = \beta_1 = Nt = 0 = Rd = Sc$.

Rotation Parameter	$F'(0)$		
ω	Turkyilmazoglu [15]	Mustafa *et al.* [18]	Present results
0	-1.1737	-1.1737	-1.1739
1	-0.9483	-0.9483	-0.9485
2	-0.3262	-0.3263	-0.3264
5	3.1937	3.1937	3.1937
10	12.7209	12.7206	12.7209
20	40.9057	40.9056	40.9057

Table 2.2: A comparison for $G'(0)$ of several ω when $Pr = 1$ and $\beta_1 = Nt = Nb = Rd = Sc = 0$.

Rotation parameter	$-G'(0)$		
ω	Turkyilmazoglu [15]	Mustafa *et al.* [18]	Present results
0	0.0000	0.0000	0.0000
1	1.4870	1.4870	1.4870
2	3.1278	3.1278	3.11278
5	9.2535	9.2536	9.2536
10	22.9134	22.9139	22.9136
20	60.0129	59.6895	60.0127

Table 2.3: A Comparison of $-\theta'(0)$ of several ω when $Pr = 1$ and $\beta_1 = Nt = Nb = Rd = Sc = 0$.

Rotation parameter	$-\theta'(0)$		
ω	Turkyilmazoglu [15]	Mustafa *et al.* [18]	Present results
0	0.8520	0.8520	0.8525
1	0.8785	0.8757	0.8759
2	0.9304	0.9304	0.9305
5	1.1291	1.1292	1.1291
10	1.4259	1.4260	1.4259
20	1.8944	1.8743	1.8944

Table 2.4: A comparison of $F'(0)$, $-G(0)$, and $-H(\infty)$ with table (5.6) in Ref. [14] for $\omega = 1$, and $\beta_1 = 0$.

$F'(0)$		$-G'(0)$		$-H(\infty)$	
Ref. [14]	Observe	Ref. [14]	Observe	Ref. [14]	Observe
0.5102	0.5102136	0.6159	0.6159096	0.8845	0.8842967

Table 2.5: A comparison of $-\theta'(0)$ with table (8.1) in Ref. [41] for $\omega = 1$, and $\beta_1 = Rd = 0$.

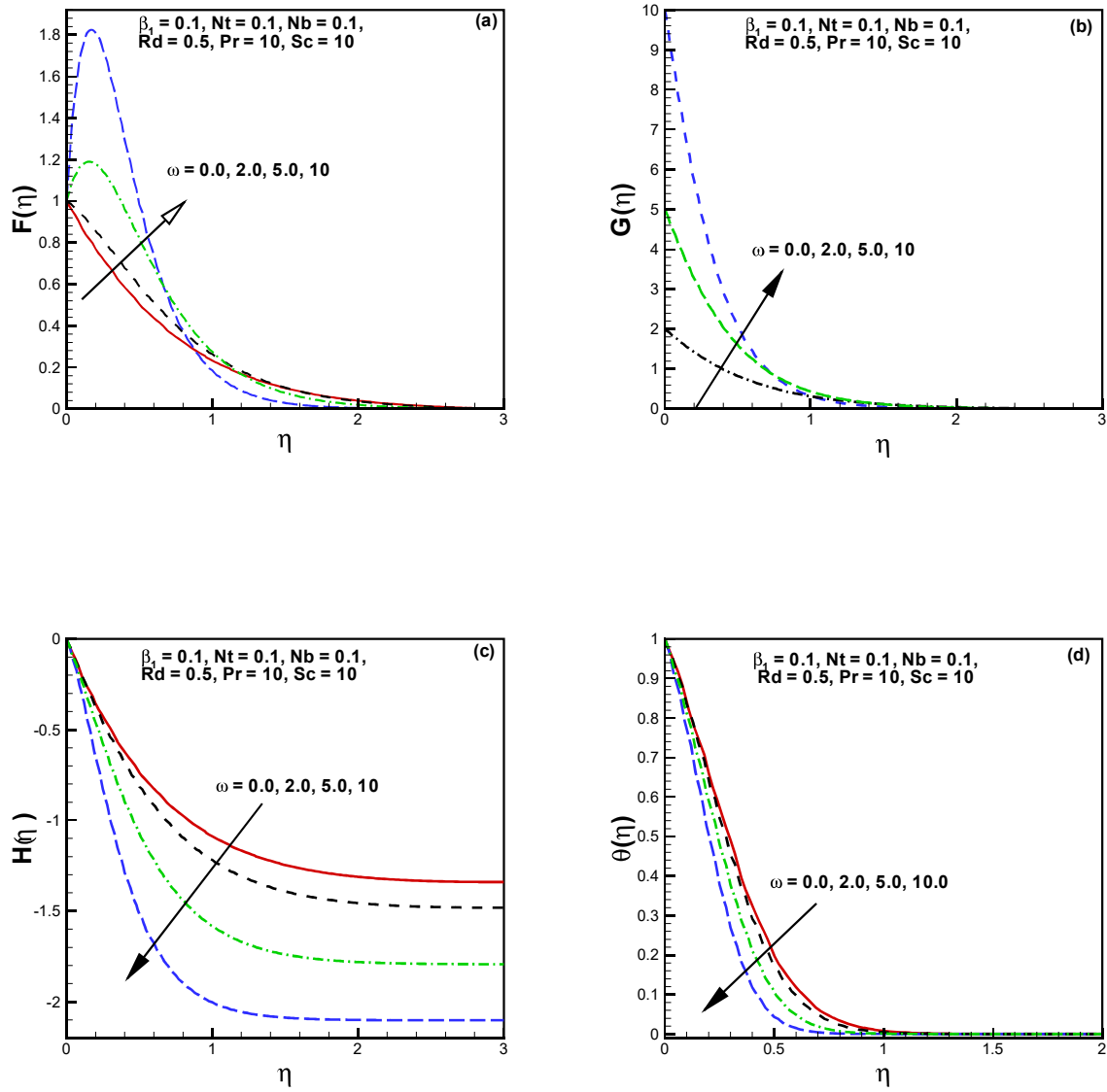|		$-\theta'(0)$			
		$n_* = 0$			
Pr	Ref. [14]	Present	Pr	Ref. [14]	Present
1.0	0.3963	0.3963237	9.0	1.0873	1.087272
1.05	0.4070	0.4069937	10.0	1.1341	1.13409
1.1	0.4173	0.4173379	11.0	1.1779	1.177838
1.5	0.4906	0.4905428	13.0	1.2579	1.257853
2.0	0.5653	0.5652200	15.0	1.3300	1.330212
2.28	0.6016	0.6015237	17.0	1.3958	1.396129
2.4	0.6162	0.6161445	19.0	1.4567	1.457005
2.5	0.6280	0.6279489	20.0	1.4855	1.485833
3.0	0.6826	0.682547	50	2.0909	2.090888
4.0	0.7753	0.7753006	100	2.6871	2.687124
5.0	0.8533	0.8532698	500	4.7351	4.732268
7.0	0.9818	0.9818099	1000	6.0162	5.985911

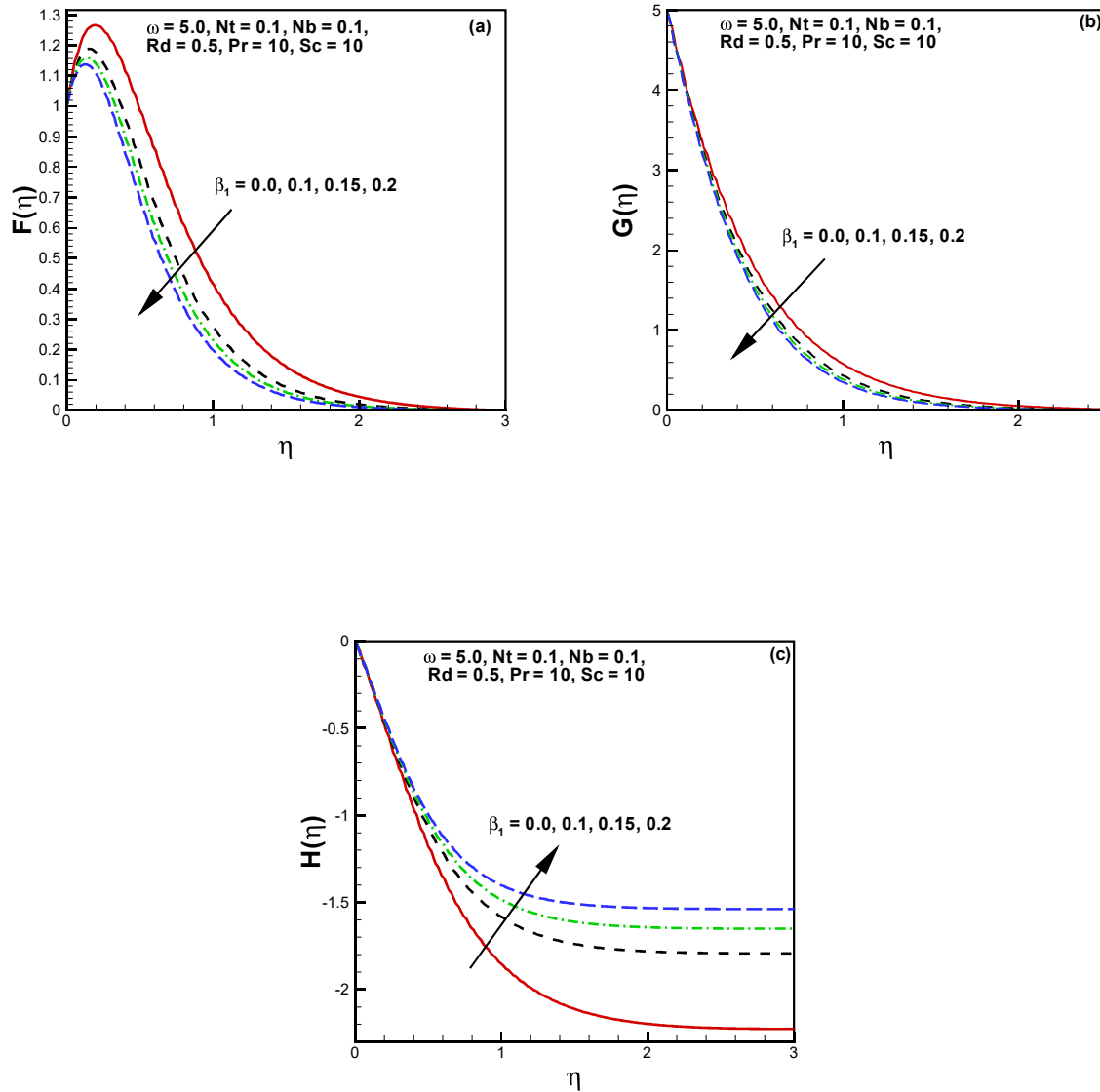**Fig. 2.2:** F, G, H and θ for ω .

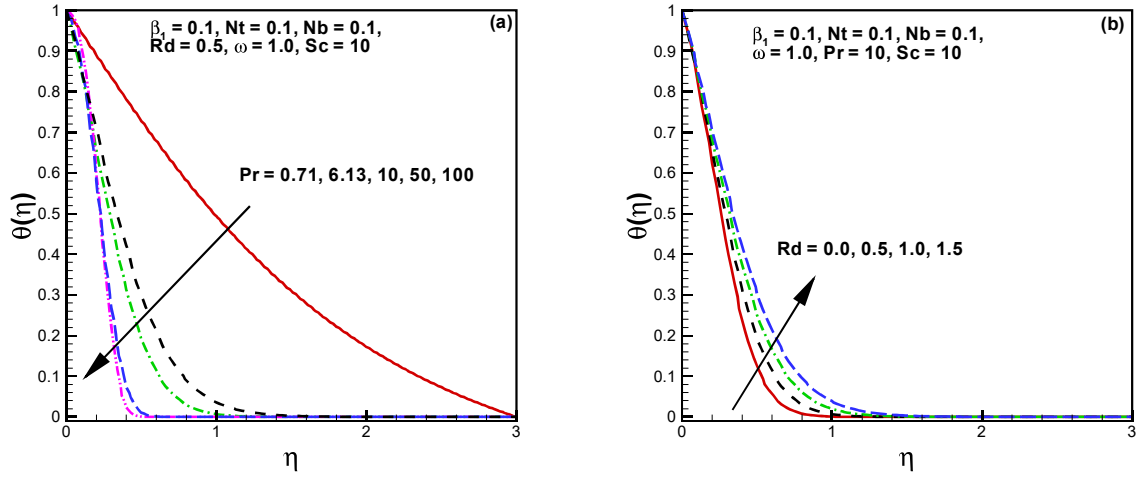**Fig. 2.3:** F, G and H for β_1 .

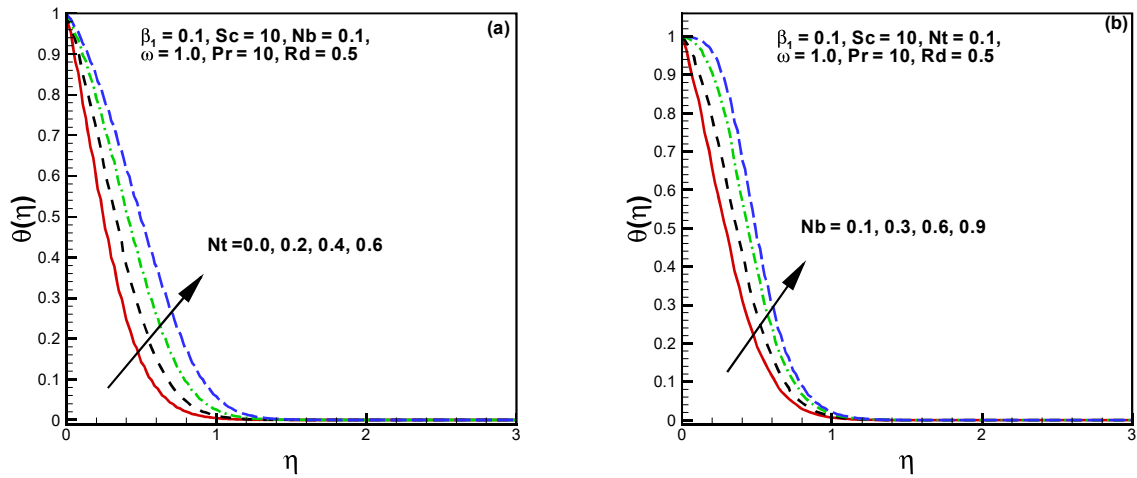**Fig. 2.4:** θ for Pr and Rd.

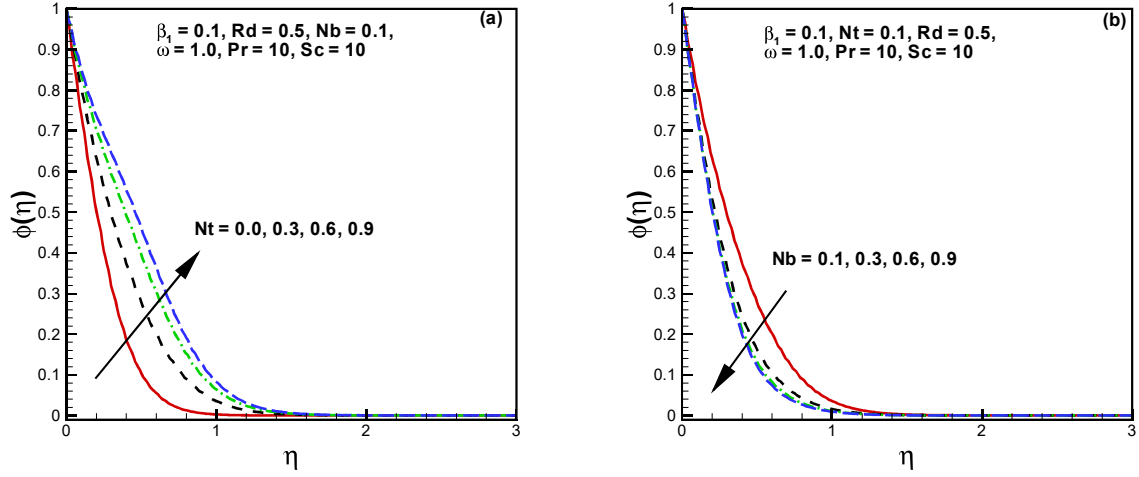**Fig. 2.5:** θ for Nt and Nb.

39

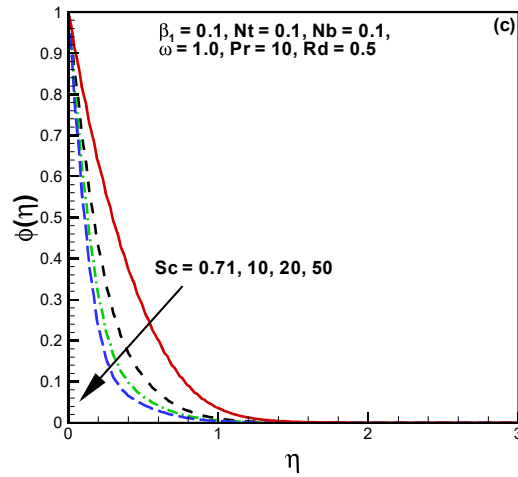**Fig. 2.6:** ϕ for Nt and Nb.

Fig. 2.7: ϕ for Sc.

40
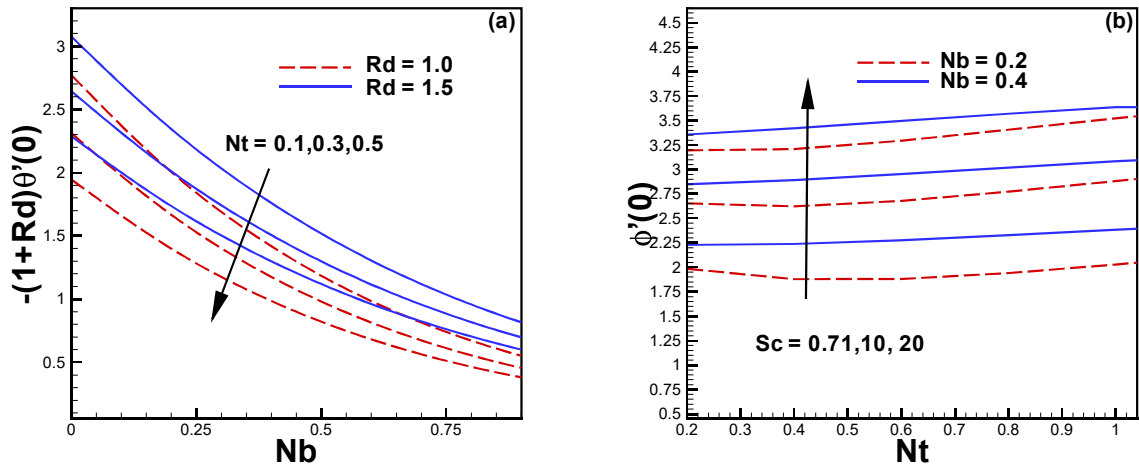
Fig. 2.8: Nu_r for Nt and Sh_r for Sc.

Chapter 3

Impact of Modified Fourier Law in Chemically Reactive Maxwell Fluid Flow

This chapter reports the influence of modified Fourier's law of thermal conduction on Maxwell fluid swirling triggered by a rotating disk. The application of the first-order chemical reaction with temperature-dependent heat conductivity is employed in mass and heat transport analysis. Moreover, a uniform rotation and stretching of disk disrupt the fluid motion. A numerical scheme, specifically the Runge-Kutta-Fehlberg (RKF45) method on Maple is used to carry out analysis of the problem. The impacts of the governing parameters are illustrated via graphs and displayed as the velocity, temperature, and concentration profiles. The results obtained infer that due to the Lorentz force the velocity components lessen; however, temperature of the fluid is enhanced. Furthermore, for large values of the thermal-relaxation parameter, the fluid temperature reduces significantly. The concentration field is also observed to be decreasing for the chemical reaction parameters and Schmidt number.

3.1 Problem Formulation

An incompressible steady Maxwell fluid flow due to a rotating stretchable disk is considered with magnetic beam projected along z-axis. The flow configuration is modeled in cylindrical coordinates. It is assumed that disk is rotating with velocity $v = \Omega r$ and stretching with velocity $u = cr$ along $-\varphi$ and $-r$ directions, respectively, and is depicted through **Fig**. **2.1**. Features of heat transfer configuration are modeled with the modified version of Fourier's law of heat conduction along with applications of temperature dependent thermal conductivity. In modified Fourier's law of heat conduction, a time factor has been introduced to replace the parabolic heat distribution into hyperbolic heat distribution. Furthermore, the impact of homogeneous first order chemical reaction is incorporated in the mass transfer phenomenon. With this effect, a direct relation exists between the rate of chemical reaction and species concentration. The heat flux $\mathbf{q}$ in case of modified Fourier law with variable thermal conductivity satisfies the following relationship:

$$\mathbf{q} + \delta_E \left(\frac{\partial \mathbf{q}}{\partial t} + \mathbf{V} \cdot \nabla \mathbf{q} - \mathbf{q} \cdot \nabla \mathbf{V} + (\nabla \cdot \mathbf{V}) \mathbf{q} \right) = -k(T)\nabla T, \tag{3.1}$$

where the thermal relaxation time is represented by δ_E and the variable thermal conductivity by $k(T) = k_\infty \left(1 + \varepsilon \frac{T - T_\infty}{T_w - T_\infty} \right)$ with ε the thermal conductivity. The above assumptions lead to the following continuity, momentum, energy (Eliminating $\mathbf{q}$ from Eqs. (1.8) and (3.1)) and concentration equations

$$\frac{\partial}{\partial z}(w) + \frac{1}{r}\frac{\partial}{\partial r}(ru) = 0, \tag{3.2}$$

$$u\frac{\partial u}{\partial r} - \frac{v^2}{r} + w\frac{\partial u}{\partial z} = \nu\frac{\partial^2 u}{\partial z^2} - \lambda_1 \left[\begin{array}{c} u^2\frac{\partial^2 u}{\partial r^2} + w^2\frac{\partial^2 u}{\partial z^2} + 2uw\frac{\partial^2 u}{\partial r\partial z} \\ -\frac{2uv}{r}\frac{\partial v}{\partial r} - \frac{2vw}{r}\frac{\partial v}{\partial z} + \frac{uv^2}{r^2} + \frac{v^2}{r}\frac{\partial u}{\partial r} \end{array} \right] - \frac{\sigma B_0^2}{\rho}\left(u + w\lambda_1\frac{\partial u}{\partial z} \right), \tag{3.3}$$

$$u\frac{\partial v}{\partial r} + w\frac{\partial v}{\partial z} + \frac{uv}{r} = \nu\frac{\partial^2 v}{\partial z^2} - \lambda_1 \left[\begin{array}{c} u^2\frac{\partial^2 v}{\partial r^2} + w^2\frac{\partial^2 v}{\partial z^2} + 2uw\frac{\partial^2 v}{\partial r\partial z} \\ +\frac{2uv}{r}\frac{\partial u}{\partial r} + \frac{2vw}{r}\frac{\partial u}{\partial z} - \frac{2u^2v}{r^2} - \frac{v^3}{r^2} + \frac{v^2}{r}\frac{\partial v}{\partial r} \end{array} \right] - \frac{\sigma B_0^2}{\rho}\left(v + w\lambda_1\frac{\partial v}{\partial z} \right), \tag{3.4}$$

$$u\frac{\partial T}{\partial r} + w\frac{\partial T}{\partial z} + \delta_E \left[\begin{array}{c} u^2\frac{\partial^2 T}{\partial r^2} + w^2\frac{\partial^2 T}{\partial z^2} + 2uw\frac{\partial^2 T}{\partial r\partial z} \\ + \left(w\frac{\partial u}{\partial z} + u\frac{\partial u}{\partial r} \right)\frac{\partial T}{\partial r} + \left(w\frac{\partial w}{\partial z} + u\frac{\partial w}{\partial r} \right)\frac{\partial T}{\partial z} \end{array} \right] = \frac{1}{\rho c_p}\frac{\partial}{\partial z}\left(k(T)\frac{\partial T}{\partial z} \right), \tag{3.5}$$

$$u\frac{\partial C}{\partial r} + w\frac{\partial C}{\partial z} = D\left(\frac{\partial^2 C}{\partial z^2}\right) - K_r\left(C - C_\infty\right), \tag{3.6}$$

with conditions (2.33, 2.34) (cf. Chapter **2**)

$$\left[(u, v, w, T, C) = (cr, \ \omega r, \ 0, \ T_w, \ C_w) \text{ at } z = 0\right],$$

$$\left[(u, v, T, C) = (0, \ 0, \ T_\infty, \ C_\infty) \text{ as } z \to \infty\right], \tag{3.7}$$

where the velocity components in $r-$, $\varphi-$ and $z-$ directions are respectively, $u, v,$ and w. The swirl rate is denoted by Ω and the stretching rate by c. Using the transformations (2.35) (cf. Chapter **2**), Eqs. (3.2) to (3.7) reduce into following dimensionless forms

$$H' + 2F = 0, \tag{3.8}$$

$$F'' - HF' + G^2 - F^2 - \beta_1\left(2FF'H - 2HGG' + H^2F''\right) - M\left(F + \beta_1 HF'\right) = 0, \tag{3.9}$$

$$G'' - HG' - 2FG - \beta_1\left(2HGF' + H^2G'' + 2FG'H\right) - M\left(G + \beta_1 HG'\right) = 0, \tag{3.10}$$

$$(1 + \varepsilon\theta)\theta'' + \varepsilon\theta'^2 - \Pr\lambda_E\left(H^2\theta'' + H\ H'\theta'\right) - \Pr H\ \theta' = 0 \tag{3.11}$$

$$\frac{1}{Sc}\phi'' - H\phi' - \gamma\phi = 0, \tag{3.12}$$

$$F(0) = 1,\ G(0) = \omega,\ H(0) = 0,\ \theta(0) = 1,\ \phi(0) = 1,$$

$$F(\infty) = 0,\ G(\infty) = 0,\ \theta(\infty) = 0,\ \phi(\infty) = 0, \tag{3.13}$$

where $\beta_1 = \lambda_1 c$ is the Deborah number (For $\beta_1 = 0$, the Maxwell model reduces to case of viscous fluid model), $M = \frac{\sigma B_0^2}{c\rho}$ the magnetic field, $\Pr = \frac{\nu}{\alpha}$ the Prandtl number, $\lambda_E = c\ \delta_E$ the thermal relaxation parameter, $\gamma = \frac{K_r}{c}$ the chemical reaction parameter, $Sc = \frac{v}{D_B}$ the Schmidt number and $\omega = \frac{\Omega}{c}$ the rotation parameter.

3.1.1   Mass Transfer Rate

At the disk wall, the mass transfer rate can be evaluated by Sherwood number Sh_r. Sherwood number can be defined physically by Fick's law which can be expressed as

$$Sh_r = -\frac{R}{(C_w - C_\infty)} \left(\frac{\partial C}{\partial z}\right) |_{z=0}, \tag{3.14}$$

and dimensionless form is

$$Re^{-1/2} \; Sh_r = -\phi'(0), \tag{3.15}$$

3.2 Numerical Solution Procedure

Runge-Kutta Fehlberg method (RKF45) in Maple software is employed to obtain the numerical solution of governing non-linear problem (3.8) to (3.13). A detail discussion can be seen in section **(1.4.1)**

The stability analysis of RK method is one of the interesting part regarding the numerical solution of ODEs. In error perspective, too much time for computation and round-off error occur when too small step size is used. For the opposite case, one should also deliberate and inquire about the step size upper bound. Such a bound encountered frequently and reaches with the method grows unstable numerically, the qualitative correspondence between produce numerical and exact solution no longer take place due to the happening of some bifurcation. The customary criterion for confirming that a numerical method is stable is called absolute stability. Runge-Kutta and other numerical methods' Absolute-stability analysis is explained by a linear model problem

$$y' = \lambda y, \tag{3.16}$$

$$y(a) = \alpha, \; a \leq x, \tag{3.17}$$

where λ is complex. The analytical solution is

$$y(x) = \alpha e^{\lambda(x-a)}. \tag{3.18}$$

At $y = 0$ for $Real(\lambda) < 0$, the problem has a stable fixed point. The problem is generalized as for the system of ODEs

45

$$y' = Ay, \qquad\qquad (3.19)$$

$$y(a) = \alpha, \ \alpha \leq x, \qquad\qquad (3.20)$$

where A is a matrix with distinct eigenvalues all lying in the negative half plane so that again we have a stable fixed point at $y = 0$.

The region of absolute stability shown in **Fig. 3.1** is indicated by the values (non-negative and real) of step size for a method and λ (complex) for which $y_n \to 0$ as $n \to \infty$, i.e., for which the fixed point at the origin is stable. For $|S| \leq 1$, the step size h and λ values set should be appropriate. Where S is the stability function for the Jacobian eigenvalue of the RK map evaluated at the fixed point. The modulus of the stability function is an alternative for the system of ODEs which is given by spectral radius of the Jacobian of the RK map at the fixed point.
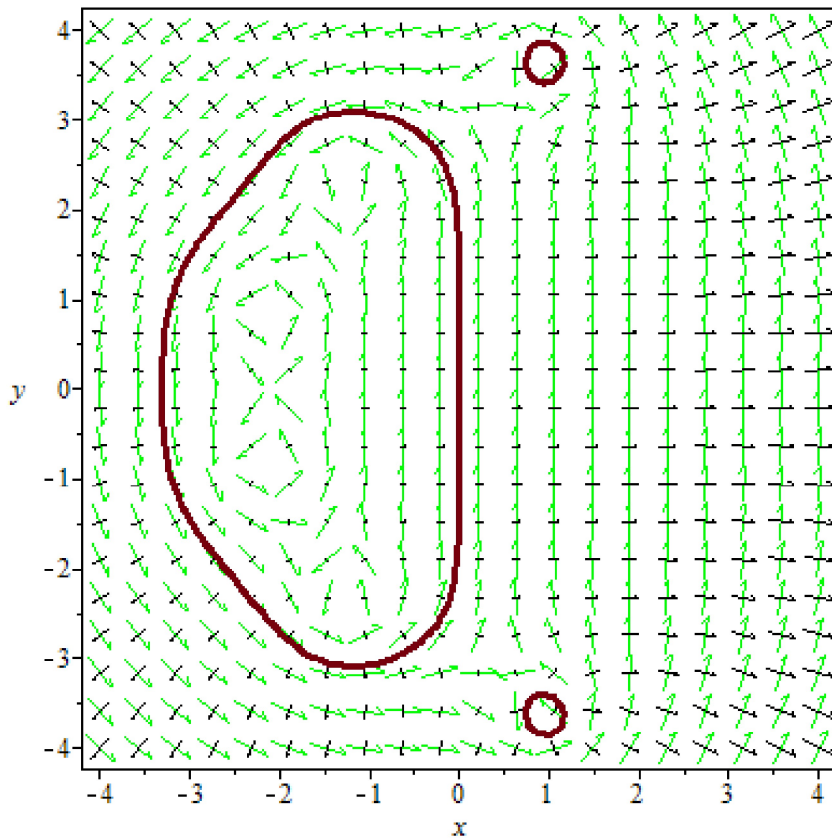
Fig. 3.1: Stability region of RK method.

3.3 Physical Interpretation

Numerical consequences to this exploration are affirmed in terms of profiles for the velocity, temperature and concentration for numerous pertinent parameters. Physical parameters for present investigation comprise of the rotation parameter ω, Deborah number β_1, magnetic number M, chemical reaction parameter γ, Prandtl number Pr, thermal relaxation time parameter λ_E, thermal conductivity parameter ε and Schmidt number Sc,. The influence of these dimensionless numbers on the radial $F(\eta)$, axial $H(\eta)$, and azimuthal $G(\eta)$ velocity components, temperature $\theta(\eta)$, concentration distributions $\phi(\eta)$ and Sherwood number $-\phi'(0)$ are graphically plotted through graphs **3.2(a-d)** to **3.6(a,b)**.

The effect of magnetic parameter M on the velocity components in radial $F(\eta)$, axial $H(\eta)$, azimuthal $G(\eta)$ directions and temperature $\theta(\eta)$ contours are captured with numeric algorithm through **Figs. 3.2(a-d)**. The implementation of magnetic flux can perform a significant part in regulating the fluid motion and thermal transport mechanism in many conducting fluids. **Figs 3.2(a,b)** manifest the deviation of velocity field in radial and azimuthal directions for the growth in M with fixed $\beta_1 = 0.1$ and considering two cases of rotation parameter $\omega = 2.0$ and 4.0. It is remarkable to mention here that strengthen magnetic field effects have a strong tendency to slow down the fluid motion, which in turn reduces the thickness of momentum boundary layer. Physically, this phenomenon is realistic since M is the proportion of electromagnetic force to the viscous force, in this fashion, enhancement in values of M yields depreciating the viscous force which in turns reduces the velocity. **Fig. 3.2(c)** reveals that the decreasing value of magnetic field M leads to magnify the $H(\eta)$ which means that boosting value of magnetic field M is to slow down the fluid motion in the negative axial direction. It is noteworthy that the velocity components have higher value in case of rotation parameter $\omega = 4.0$ as compared to $\omega = 2.0$. Physically, rotation parameter ω is the ratio of swirl Ω to stretch c rates. So higher value of rotation parameter ω implies stronger the rotation rate Ω which as a consequence produces the strong centrifugal force. The ability of this force is to push the fluid particles in radial direction. Therefore, the radial $F(\eta)$ as well as the azimuthal $G(\eta)$ components grow due to enhancing the rotation ω. To compensate this, a downward fluid flow towards the disk surface occurs which is depicted in **Fig. 3.2(c)**. **Fig. 3.2(d)** demonstrates the variation in temperature profile

$\theta(\eta)$ with magnetic parameter M for rotation $\omega = 2.0$ and 4.0. It is apparent from this figure, that an upsurge is viewed in fluid temperature $\theta(\eta)$ for increasing M. Further, we noticed that fluid temperature reduces for the lower estimation of parameter $\omega = 2.0$.

Figs. 3.3(a,b) represent the influence of β_1 on radial and circumferential motion. As β_1 upsurges, the velocity components in radial as well azimuthal directions move towards the stretching wall. This indicates that boundary layer develops narrow by enlarging β_1. It is obvious to remark here that the achievement of temperature for fluid is higher with boosting the rotation parameter ω. **Fig. 3.3(c)** plots the velocity profile component $H(\eta)$ in axial direction for various values of Deborah number β_1. Here the values of azimuthal velocity are moving from negative to zero by enlarging the Deborah number β_1 which implies that fluid flowing towards negative $z-$direction due to the rotation and stretching are slow down by uplifting the value of Deborah number. The temperature field increases with boosting the Deborah number which is shown in **Fig. 3.3(d)**. Further, the velocity components have lower value for rotation $\omega = 2.0$ as compared to $\omega = 4.0$ while a reverse mode is examined in case of temperature field $\theta(\eta)$.

The Pr impact on $\theta(\eta)$ is visualized in **Fig. 3.4(a)** for constant thermal conductivity $(\varepsilon = 0)$ and variable thermal conductivity $(\varepsilon = 0.5)$. It is clear that all physically possible values for Prandtl number can be tackled by current numerical scheme. Prandtl number Pr compares the hydrodynamic thickness and thermal boundary layers. Air and other gases have low Prandtl number attributed to their low viscosity while viscoelastic fluids and water generally possess a high value of Prandtl number. An escalation in Pr suggests a decline in thermal diffusivity. Consequently, the boundary layer concerning temperature becomes thin with the augmentation in Pr. Apparently at the surface, the temperature slope elevates by raising the Prandtl number Pr. Actually, larger value of Prandtl number implies that liquids have more effective transfer of convective heat than conductive heat and therefore, more heat transfer rate occurs. It is noteworthy here that a significant improvement in fluid temperature is observed when $(\varepsilon = 0.5)$ as compared to $(\varepsilon = 0)$ which is quite realistic physically.

The heat flux relation by Cattaneo–Christov is the generalization of Fourier's law where the constitutive expressions of the heat flux and liquid temperature contain the velocity vector. This specifies that heat flux not only is associated with temperature gradient but also with fluid velocity. **Fig. 3.5(b)** displays the relationship between relaxation time parameter λ_E and

temperature distribution $\theta(\eta)$ subject to constant thermal conductivity ($\varepsilon = 0$) and variable thermal conductivity ($\varepsilon = 0.5$). The value $\lambda_E = 0$ signifies that the heat flux model is reduced to classical Fourier's law. Obviously shown from this figure that $\theta(\eta)$ has the inverse relationship with the thermal relaxation time λ_E. This conclusion confirms the result with that of Han *et al.* [57]. Physically, flourishing the thermal relaxation parameter, more time is required to material particles for transferring of heat to its neighboring particles. In simple words, material reveals a non conducting property for higher value of thermal relaxation parameter, thus reducing the fluid temperature. So, it can be established that profile for $\theta(\eta)$ is higher in Fourier's law in comparison with Cattaneo-Christov expression. Furthermore, the influence ($\varepsilon = 0.5$) is to elevate the fluid temperature.

Fig. 3.5(a) predicts the characteristics of concentration field $\phi(\eta)$ with gradual increment in chemical reaction parameter γ. Obviously, it can be observed that curves for species concentration $\phi(\eta)$ decay for escalating values of γ. This is coupled with a minor shrinkage in fluid concentration. In fact, the chemical reaction parameter γ having larger values yield a reduction in the chemical molecular diffusivity. The characteristics of Schmidt number Sc on concentration profile $\phi(\eta)$ with distinct values are sketched in **Fig. 3.5(b)**. We observe a significant reduction in species concentration by pushing the values of Schmidt number Sc while other parameters are kept fixed. Physically, larger values of Sc will lead to a decline in molecular diffusivity of the fluid resulting a reduction in the species diffusion rate. While reverse influence can be observed in case of lesser values of Sc since they associate to greater molecular diffusivities. Consequently, with the development of Schmidt number Sc the concentration boundary layer thickness remarkably contracts.

Table. 3.1: A comparison of $F'(0)$ with various values of ω when $Pr = 1$ and $\beta_1 = 0$.

$M = 0$	ω	0	1	2	5
Turkyimazoglu [15]	$F'(0)$	-1.173720738	-0.948313756	-0.326243978	3.193732989
Present results		-1.173721815	-0.948314491	-0.326244272	3.193732981
$M = 2$	ω	0	1	2	5
Turkyimazoglu [15]	$F'(0)$	-1.830489674	-1.663452548	-1.175347018	1.8929454707
Present results		-1.830489679	-1.663452553	-1.175347021	1.892945470

Table. 3.2: A comparison of $-G'(0)$ with various values of ω when $Pr = 1$ and $\beta_1 = 0$.

$M = 0$	ω	0	1	2	5
Turkyimazoglu [15]	$-G'(0)$	0.000000000	1.486952682	3.127828177	9.253541181
Present results		0.000000000	1.486952819	3.127828198	9.253541178
$M = 2$	ω	0	1	2	5
Turkyimazoglu [15]	$-G'(0)$	0.000000000	2.023944904	4.113493830	11.140599491
Present results		0.000000000	2.023944903	4.113493827	11.140599489

Table. 3.3: A comparison of $-H(\infty)$ with various values of ω when $Pr = 1$ and $\beta_1 = 0$.

$M = 0$	ω	0	1	2	5
Turkyimazoglu [15]	$-H(\infty)$	1.502994055	1.573076556	1.728826487	2.252086899
Present results		1.502952500	1.573049479	1.728816732	2.252086675
$M = 2$	ω	0	1	2	5
Turkyimazoglu [15]	$-H(\infty)$	1.038474418	1.074894633	1.173952491	1.640958245
Present results		1.038474351	1.074894568	1.173952446	1.640958240

Table. 3.4: A comparison of $-\theta'(0)$ with various values of ω when $Pr = 1$ and $\beta_1 = \lambda_E = \varepsilon = 0$.

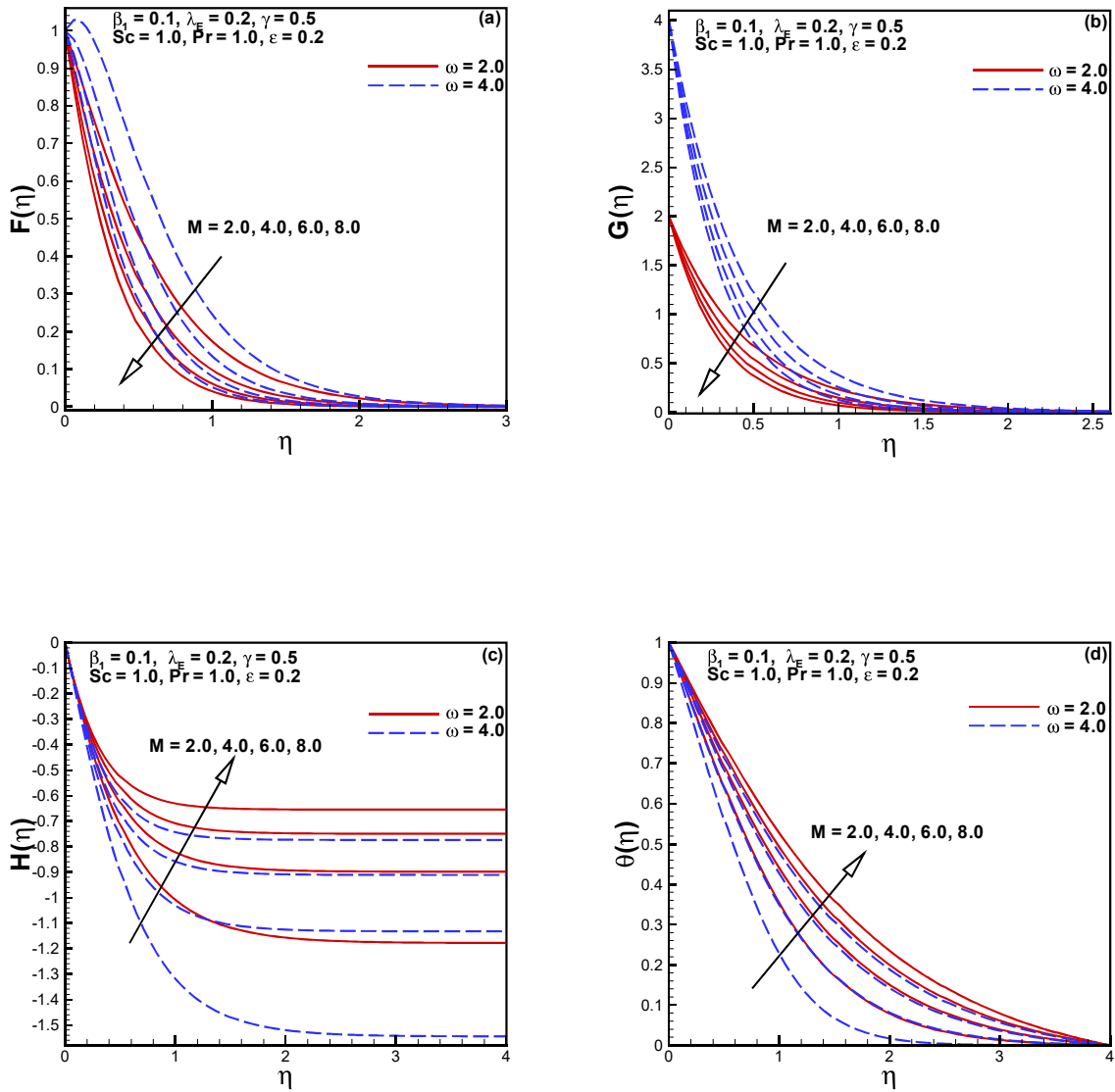| $M = 0$	ω	0	1	2	5
Turkyimazoglu [15]	$-\theta'(0)$	0.851991421	0.875662139	0.930411191	1.129140492
Present results		0.851993748	0.875663350	0.9304115178	1.129140496
$M = 2$	ω	0	1	2	5
Turkyimazoglu [15]	$-\theta'(0)$	0.726086562	0.742212295	0.785365438	0.980285183
Present results		0.726188988	0.742289416	0.785400968	0.980286049

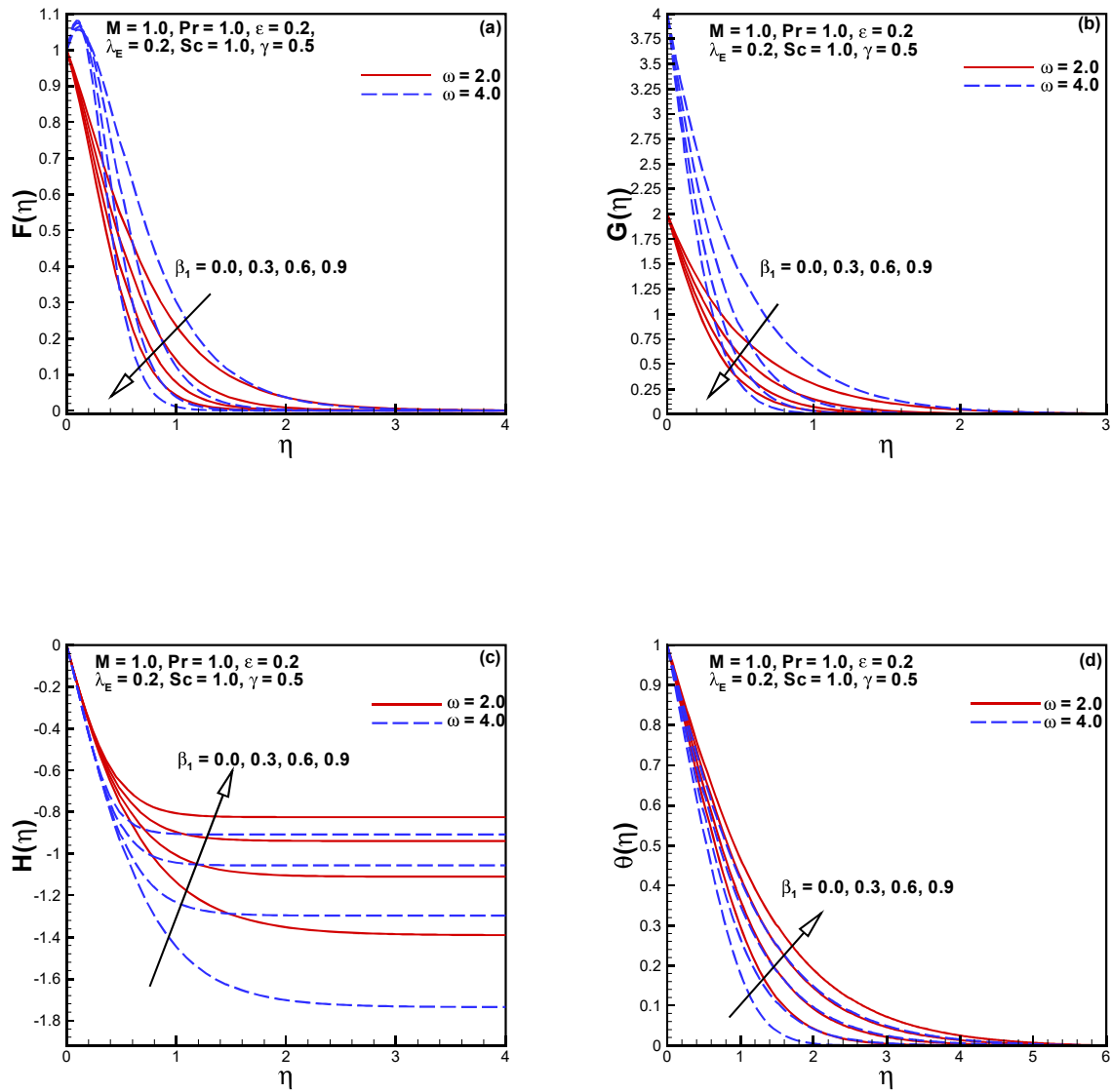**Fig. 3.2:** F, G, H and θ for M.

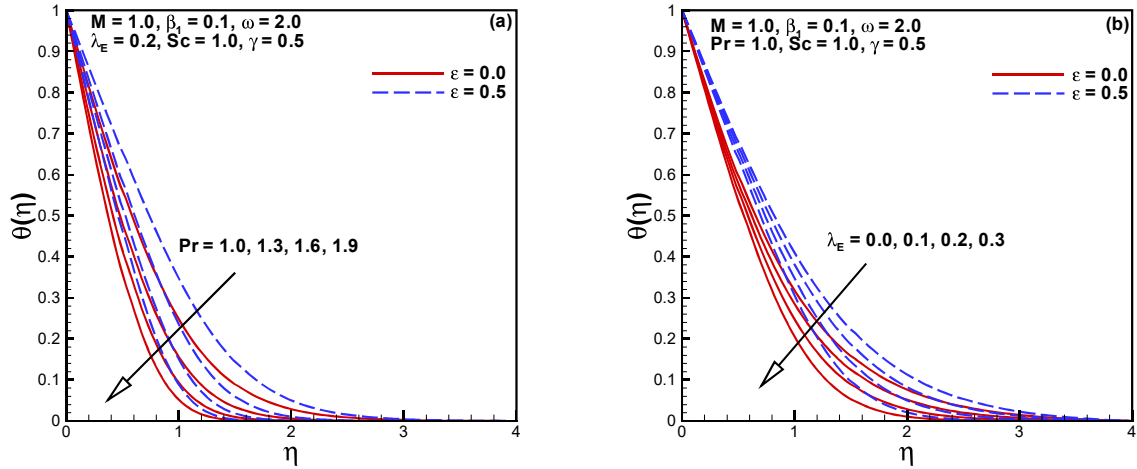**Fig. 3.3:** F, G, H and θ for β_1.

53

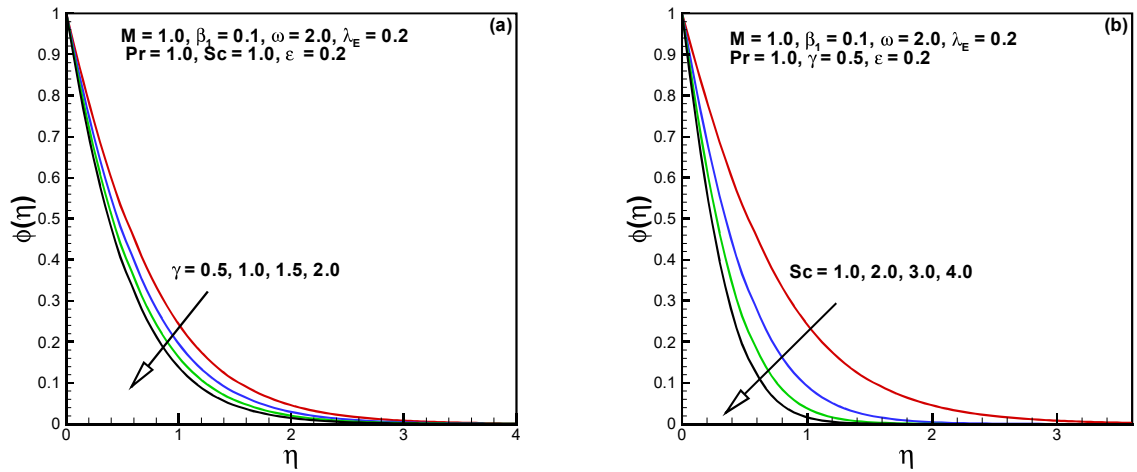**Fig. 3.4:** θ for Pr and λ_E.

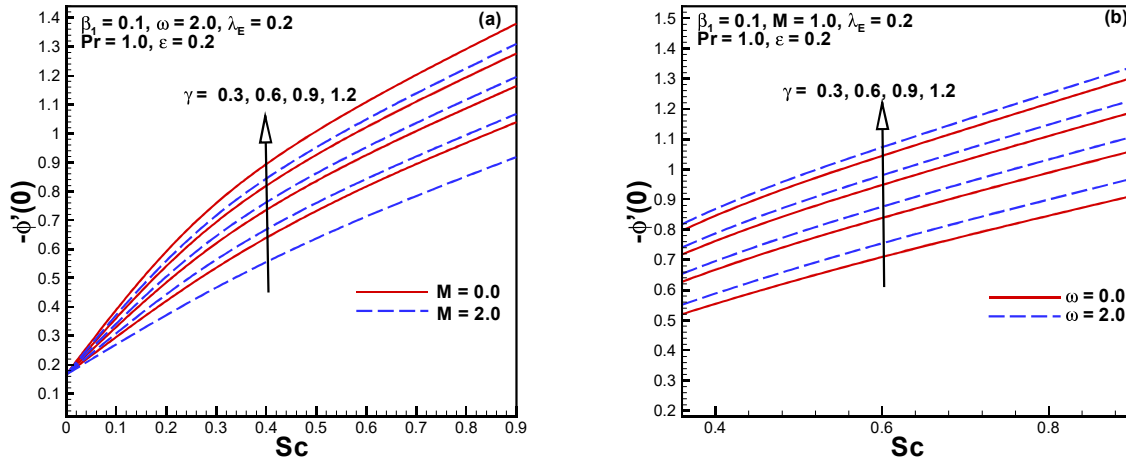**Fig. 3.5:** ϕ for γ and Sc.

Fig. 3.6: $-\phi'(0)$ for γ.

Chapter 4

Radiative Heat Transfer in Reactive Maxwell Fluid Flow

The transportation of heat and mass in magnetohydrodynamic (MHD) Maxwell fluid flow over a convectively heated stretchable rotating disk is scrutinized here. To regulate the fluid temperature at the surface, a simple isothermal model of homogeneous-heterogeneous reactions is employed. The impact of nonlinear thermal radiative heat flux on thermal transport features is studied. The transformed nonlinear system of ODEs are solved numerically with efficient method namely Runge-Kutta-Felberg (RKF45) integration scheme using Maple software. Achieved results are validated with previous studies in excellent way. Major outcomes reveal that magnetic flux reduces the flow components while enhance the fluid temperature. Also, the presence of radiative heat flux is to raise the temperature of fluid. Further the strength of homogeneous-heterogeneous reactions is very useful to diminish the concentration of reaction.

4.1   Physical Model and Governing Equations

A three dimensional Maxwell fluid flow due to a rotating stretchable disk subject to uniform magnetic field B_0 applied in the axial direction is studied. The supposition of small magnetic Reynolds number leads to ignore the induced magnetic field. Moreover, the heat transfer features are characterized through non-linear radiative heat flux. Here we assume cylindrical coordinates

system to understand the flow description as indicated in **Fig. 2.1**.

The disk surface temperature is because of convective heating process characterized by the coefficient of heat transport h_f and temperature of the hot fluid T_f. The homogeneous-heterogeneous reactions and catalyst surface are taken as inspired by Chaudhary and Merkin [68]. Homogeneous reaction for cubic autocatalysis is

$$A + 2B \rightarrow 3B, \ \text{rate} = k_c ab^2, \tag{4.1}$$

and for isothermal first-order reaction of the form, we have

$$A \rightarrow B, \ \text{rate} = k_s a, \tag{4.2}$$

where A and B denote chemical species, a and b be their concentrations and k_c and k_s are the rate constants. We further presume that the process of these reactions is isothermal. In the absence of viscous dissipation and Joule heating, the governing equations for steady three dimensional flow of a Maxwell fluid with magnetic field are

$$\frac{\partial}{\partial z}(w) + \frac{1}{r}\frac{\partial}{\partial r}(ru) = 0, \tag{4.3}$$

$$u\frac{\partial u}{\partial r} + w\frac{\partial u}{\partial z} - \frac{v^2}{r} = \nu\frac{\partial^2 u}{\partial z^2} - \lambda_1\left[w^2\frac{\partial^2 u}{\partial z^2} + 2uw\frac{\partial^2 u}{\partial r\partial z}\right.$$

$$\left. -\frac{2uv}{r}\frac{\partial v}{\partial r} - \frac{2vw}{r}\frac{\partial v}{\partial z} + \frac{uv^2}{r^2} + \frac{v^2}{r}\frac{\partial u}{\partial r} + u^2\frac{\partial^2 u}{\partial r^2}\right] - \frac{\sigma B_0^2}{\rho}\left(u + w\lambda_1\frac{\partial u}{\partial z}\right), \tag{4.4}$$

$$u\frac{\partial v}{\partial r} + w\frac{\partial v}{\partial z} + \frac{uv}{r} = \nu\frac{\partial^2 v}{\partial z^2} - \lambda_1\left[u^2\frac{\partial^2 v}{\partial r^2} + w^2\frac{\partial^2 v}{\partial z^2} + 2uw\frac{\partial^2 v}{\partial r\partial z}\right.$$

$$\left. +\frac{2uv}{r}\frac{\partial u}{\partial r} + \frac{2vw}{r}\frac{\partial u}{\partial z} - \frac{2u^2v}{r^2} - \frac{v^3}{r^2} + \frac{v^2}{r}\frac{\partial v}{\partial r}\right] - \frac{\sigma B_0^2}{\rho}\left(v + w\lambda_1\frac{\partial v}{\partial z}\right), \tag{4.5}$$

$$u\frac{\partial T}{\partial r} + w\frac{\partial T}{\partial z} = -\frac{1}{\rho c_p}\frac{\partial q_{\text{rad}}}{\partial z} + \alpha\left(\frac{\partial^2 T}{\partial z^2}\right), \tag{4.6}$$

$$u\frac{\partial a}{\partial r} + w\frac{\partial a}{\partial z} = d_A\left(\frac{\partial^2 a}{\partial z^2}\right) - k_c ab^2, \tag{4.7}$$

$$u\frac{\partial b}{\partial r} + w\frac{\partial b}{\partial z} = d_B\left(\frac{\partial^2 b}{\partial z^2}\right) + k_c ab^2, \tag{4.8}$$

57

where d_A and d_B are diffusion coefficients. The relevant conditions are

$$u = U_w = cr, \ v = \Omega r, \ w = 0, -k\frac{\partial T}{\partial z} = h_f\left(T_f - T\right), \ d_A\frac{\partial a}{\partial z} = k_s a, \ d_B\frac{\partial b}{\partial z} = -k_s a \text{ at } z = 0,$$

$$u = 0, \ v = 0, \ T \to T_\infty, \ a \to a_\circ, \ b \to 0 \text{ as } z \to \infty, \tag{4.9}$$

where c is the stretching rate, Ω the swirl rate and $a_\circ$ the positive dimensional constant.

4.1.1 Non-Dimenzionalization and Parameterization

Introducing the following similarity variables

$$\frac{a}{a_\circ} = g(\eta), \ \frac{b}{a_\circ} = h(\eta). \tag{4.10}$$

where dimensionless concentration of homogeneous bulk fluid is $g(\eta)$ and dimensionless concentration of heterogeneous catalyst at the surface is $h(\eta)$. By using the above similarity transformations and along with Eq. (2.35) (cf. Chapter **2**), Eqs. (4.3) to (4.5), (4.7), (4.8), (4.11) and (4.12) reduce into following dimensionless forms

$$H' + 2F = 0, \tag{4.11}$$

$$F'' - F^2 + G^2 - HF' - \beta_1\left(H^2 F'' + 2FF'H - 2HGG'\right) - M\left(F + \beta_1 HF'\right) = 0, \tag{4.12}$$

$$G'' - 2FG - HG' - \beta_1\left(H^2 G'' + 2FG'H + 2HGF'\right) - M\left(G + \beta_1 HG'\right) = 0, \tag{4.13}$$

$$\left(1 + \frac{4}{3}Rd\right)\theta'' + \frac{4}{3}Rd\left[(\theta_w - 1)^3\left(3\theta^2\theta'^2 + \theta^3\theta''\right) + 3\left(\theta_w - 1\right)^2\left(2\theta\theta'^2 + \theta^2\theta''\right)\right.$$

$$\left. + 3\left(\theta_w - 1\right)\left(\theta'^2 + \theta\theta''\right)\right] - \Pr\theta' H = 0, \tag{4.14}$$

$$\frac{1}{Sc}\phi'' - H\phi' - k_1\phi\psi^2 = 0, \tag{4.15}$$

$$\frac{\delta_1}{Sc}\psi'' - H\psi' + k_1\phi\psi^2 = 0, \tag{4.16}$$

$$F = 0, \ G = \omega, \ H = 0, \ \theta' = -\gamma_1\left[1 - \theta\right], \ \phi' = k_2\phi, \ \delta_1\psi' = -k_2\phi, \text{ at } \eta = 0,$$

$$F \to 0, \ G \to 0, \ \theta \to 0, \ g \to 1, \ h \to 0 \text{ as } \eta \to \infty, \tag{4.17}$$

where $\omega = \frac{\Omega}{c}$ denotes the rotation parameter. Further, M is the magnetic field, β_1 the Deborah number, Rd the radiation parameter, θ_w the temperature ratio parameter, Pr the Prandtl number, γ_1 the Biot number, k_1 the homogenous reaction, Sc the Schmidt number and k_2 the heterogeneous reaction. These dimensionless quantities are, respectively, defined as

$$M = \frac{\sigma B_0^2}{c\rho}, \ \beta_1 = \lambda_1 c, \ Rd = \frac{4\sigma^* T_\infty^3}{3kk^*}, \ \theta_w = \frac{T_f}{T_\infty}, \ Pr = \frac{\nu}{\alpha},$$

$$\gamma_1 = \frac{h_f}{k}\sqrt{\frac{\nu}{c}}, \ k_1 = \frac{k_c a_\circ^2}{c}, \ Sc = \frac{v}{D_A}, \ k_2 = \frac{k_s}{D_A}\sqrt{\frac{\nu}{c}}. \tag{4.18}$$

We assumed that the diffusion coefficients of chemical species A and B are of the same magnitude. This hypothesis leads to explore the study where the diffusion coefficients d_A and d_B are equal i.e. $\delta_1 = 1$ (see [58]). Actually, this assumption gives the relation

$$\phi(\eta) + \psi(\eta) = 1. \tag{4.19}$$

Thus Eqs. (4.15) and (4.16) turn into

$$\frac{1}{Sc}\phi'' - k_1\phi(1-\phi)^2 - H\phi' = 0, \tag{4.20}$$

with conditions

$$k_2\phi(0) = \phi'(0), \ \phi(\infty) \to 1. \tag{4.21}$$

4.1.2   Heat Transfer Performance

The efficiency of heat transport over the disk surface can be estimated by Nusselt number Nu_r. Physically, Fourier's law is utilized to define Nusselt number Nu_r. The mathematical expression of this quantity is given as

$$Nu_r = \frac{Rq_w}{k(T_f - T_\infty)}, \tag{4.22}$$

with

$$q_w = -k\left[1 + \frac{16\sigma^* T^3}{3kk^*}\right]\left(\frac{\partial T}{\partial z}\right)|_{z=0}. \tag{4.23}$$

In non-dimensional form, we can write

$$Re^{-1/2} \, Nu_r = -\left(1 + \frac{4}{3}Rd\left\{1 + (\theta_w - 1)\,\theta(0)\right\}^3\right)\theta'(0), \qquad (4.24)$$

4.2 Physical Interpretation

To compute the numerical solution of proposed problem (4.11) to (4.14), (4.17), (4.20) and (4.21), Runge-Kutta-Fehlberg (RKF45) integration scheme is implemented. This section is focused on physical explanation of involved parameters in flow, heat and mass transfer distributions. The above stated numerical computation is carried out for magneto Maxwell fluid due to stretchable rotating disk. The heat transfer characteristics are investigated with non-linear thermal radiation effects. Homogeneous-heterogeneous reactions are considered on the fluid volume concentration. The impact of parameters like rotation $0.0 \leq \omega \leq 6.0$, magnetic field $0.0 \leq M \leq 3.0$ are examined on $F(\eta), \; G(\eta), \; H(\eta)$ velocity components and temperature field $\theta(\eta)$. Effects of radiation parameter $0.0 \leq Rd \leq 0.6$, Biot number $0.0 \leq \gamma_1 \leq 2.0$, on temperature distribution $\theta(\eta)$ are inspected. Homogeneous reaction strength $0.2 \leq k_1 \leq 0.8$, heterogeneous (surface) reaction strength parameter $0.1 \leq k_2 \leq 0.7$, magnetic field $0.0 \leq M \leq 3.0$ and Schmidt number $1.0 \leq Sc \leq 2.5$ are studied on volume concentration $g(\eta)$.

Figs. 4.1(a-d) are displayed to investigate the role of ω on the velocity components and temperature field. Figs. 4.1(a,b) show that the radial and azimuthal velocity components represented by $F(\eta)$ and $G(\eta)$, respectively, increase with varying value of rotation parameter ω. The rotation parameter ω is ratio of swirl rate Ω to stretch rate c. Thus, it gives us measure of swirl rate to stretch rate. When rotation ω starts flourishing, this means the swirl rate becomes larger compared to stretch rate. The case $\omega = 0$ implies the stretching without rotation. For the special choice of magnetic parameter $(M = 1.0)$ and Deborah number $(\beta_1 = 0.1)$, radial and azimuthal velocity components represented by $F(\eta)$ and $G(\eta)$, respectively, grow up. The main reason behind it is that an increase in ω strengthen the centrifugal force which pumps the fluid radially outward. It is further observed that the change in radial and azimuthal velocities due to rotation diminishes gradually when moves away from the disk. Physically this trend was expected because the influence of centrifugal force is limited at the disk vicinity. The

usual enhancement in the angular component of velocity with flourishing rotation near the disk surface can be visualized in **Fig. 4.1(b)**. **Fig. 4.1(c)** depicts a decreasing trend in the axial velocity component $H(\eta)$ with stronger rotation rate. This happens because with accelerated rotation rate, the fluid particles are forced to move in radial direction and this is compensated by the particles which are drawn towards the disk surface in the negative axial direction. It is appeared from **Fig. 4.1(d)** that the fluid temperature decreases as the rotation parameter becomes strengthen without Joule heating and dissipation effects.

The influence of M on the flow and thermal curves at a prescribed rotation parameter ω and Deborah number β_1 are sketched in **Fig. 4.2(a-d)**. It is obvious that as the magnetic field M turns into powerful, the velocity curves reduce considerably in all directions. Contrary to velocity profile, the temperature field $\theta(\eta)$ rises, which is because of the fact of growth in skin-friction which offers obstruct to fluid particles. Thus, heat is generated in the fluid by the occurrence of magnetic field in vertical direction. Physically, a resistive force called the Lorentz force is developed due to presence of the applied magnetic field in the electrically conducting fluid. The feature of this force is to retard the flow over the disk at the expense of enhancing its temperature. This is portrayed by the decline in the radial, tangential and axial velocity components and uplift in the temperature field as M develops which is depicted in **Fig. 4.2(a-d)**.

Fig. 4.3(a) elaborates the curves of thermal field $\theta(\eta)$ for various values of radiative parameter Rd. The thermal field $\theta(\eta)$ and their associated thickness of boundary layer are risen for enhancement in the values of Rd. As expected, the existence of radiative parameter implies to absorb more heat by the fluid that corresponds to higher temperature. The features of local Biot number γ_1 with various values on fluid temperature are displayed in **Fig. 4.3(b)**. Physically, a gradual increment in the Biot number γ_1 effects in the larger convection at disk surface which elevates the fluid temperature. Furthermore, thermal boundary layer thickness significantly pronounced by the stronger Biot number γ_1.

Fig. 4.4(a) reveals the actions of parameter k_1, denoting homogeneous reaction strength, on fluid concentration $g(\eta)$. Concentration profile reduces while consequent boundary layer develops thicker as the homogeneous reaction k_1 strengthens. **Fig. 4.4(b)** shows the variation of concentration profile for numerous values of heterogeneous (surface) reaction strength parameter k_2, the magnitude of concentration profile $\phi(\eta)$ reduces with uplifting the strength of

heterogeneous reaction k_2. This happens from the reason that augmentation in either k_1 or k_2 suggests the consumption of reactants in the flow field which corresponds a reduction in fluid volume concentration $g(\eta)$.

Ratio between viscosity and mass diffusivity is called Schmidt number Sc. **Fig. 4.5(a)** elaborates the plots of concentration profile with growing rating of Sc. It is observed that larger Schmidt number leads to fall in concentration profile. As expected, an escalate in Sc agrees to diminish the mass diffusivity and as a result fluid concentration reduces. The impression of parameter M on $g(\eta)$ is observed in **Fig. 4.5(b)**. The increasing values for magnetic field reduces the concentration profile due to the resistive force which is developed in the walk of magnetic force.

Tables 1 and **2** are organized for the authentication of present numerical computations. For this we have calculated the numerical values for radial $F'(0)$, angular skin friction $-G'(0)$, vertical velocity $-H(\infty)$ and Nusselt number $-\theta'(0)$ in limiting cases for different values of rotation parameter ω with magnetic field ($M = 0, M = 2$). The attained outcomes match in outstanding way with those of Turkyimazoglu [15] which confirms the accuracy of applied numerical scheme. The numerical computations of local Nussetl number Nu_r is included in **Table 3**. It appears that heat transport $-\left(1 + Rd\left\{1 + (\theta_w - 1)\,\theta(0)\right\}^3\right)\theta'(0)$ enhances with an increase in physical parameters like rotation $0.0 \leq M \leq 6.0$, thermal radiation $0.1 \leq R_d \leq 0.4$, Biot number $0.5 \leq \gamma_1 \leq 2.0$ and temperature ratio $1.2 \leq \theta_w \leq 1.8$. A decreasing trend is observed for Prandtl number ($1.0 \leq \mathrm{Pr} \leq 7.0$).

Table 4.1: A comparison of $F'(0)$ and $-G'(0)$ with various values of ω for $M = 0$ and $M = 2$ when $\beta_1 = 0$.

M	ω	$F'(0)$		$-G'(0)$	
		Turkyimazoglu [15]	Present results	Turkyimazoglu [15]	Present results
0	0	-1.173720738	-1.173721815	0.000000000	0.000000000
	1	-0.948313756	-0.948314491	1.486952682	1.486952819
	2	-0.326243978	-0.326244272	3.127828177	3.127828198
	5	3.193732989	3.193732981	9.253541181	9.253541178
2	0	-1.830489674	-1.830489679	0.000000000	0.000000000
	1	-1.663452548	-1.663452553	2.023944904	2.023944903
	2	-1.175347018	-1.175347021	4.113493830	4.113493827
	5	1.8929454707	1.892945470	11.140599491	11.140599489

Table 4.2: A comparison of $-H(\infty)$ and $-\theta'(0)$ with various values of ω for $M = 0$ and $M = 2$ when $Pr = 1$ and $\beta_1 = Rd = \gamma_1 = \theta_w = Sc = k_1 = k_2 = 0$.

M	ω	$-H(\infty)$		$-\theta'(0)$	
		Turkyimazoglu [15]	Present results	Turkyimazoglu [15]	Present results
0	0	1.502994055	1.502952500	0.851991421	0.851993748
	1	1.573076556	1.573049479	0.875662139	0.875663350
	2	1.728826487	1.728816732	0.930411191	0.9304115178
	5	2.252086899	2.252086675	1.129140492	1.129140496
2	0	1.038474418	1.038474351	0.726086562	0.726188988
	1	1.074894633	1.074894568	0.742212295	0.742289416
	2	1.173952491	1.173952446	0.785365438	0.785400968
	5	1.640958245	1.640958240	0.980285183	0.980286049

Table 4.3: The data for $Re^{-1/2} Nu_r$ against M, Rd, γ_1, θ_w, and Pr by keeping $\omega = 6.0$, $\beta_1 = 0.1$, $Sc = 5.0, k_1 = 0.5 = k_2$.

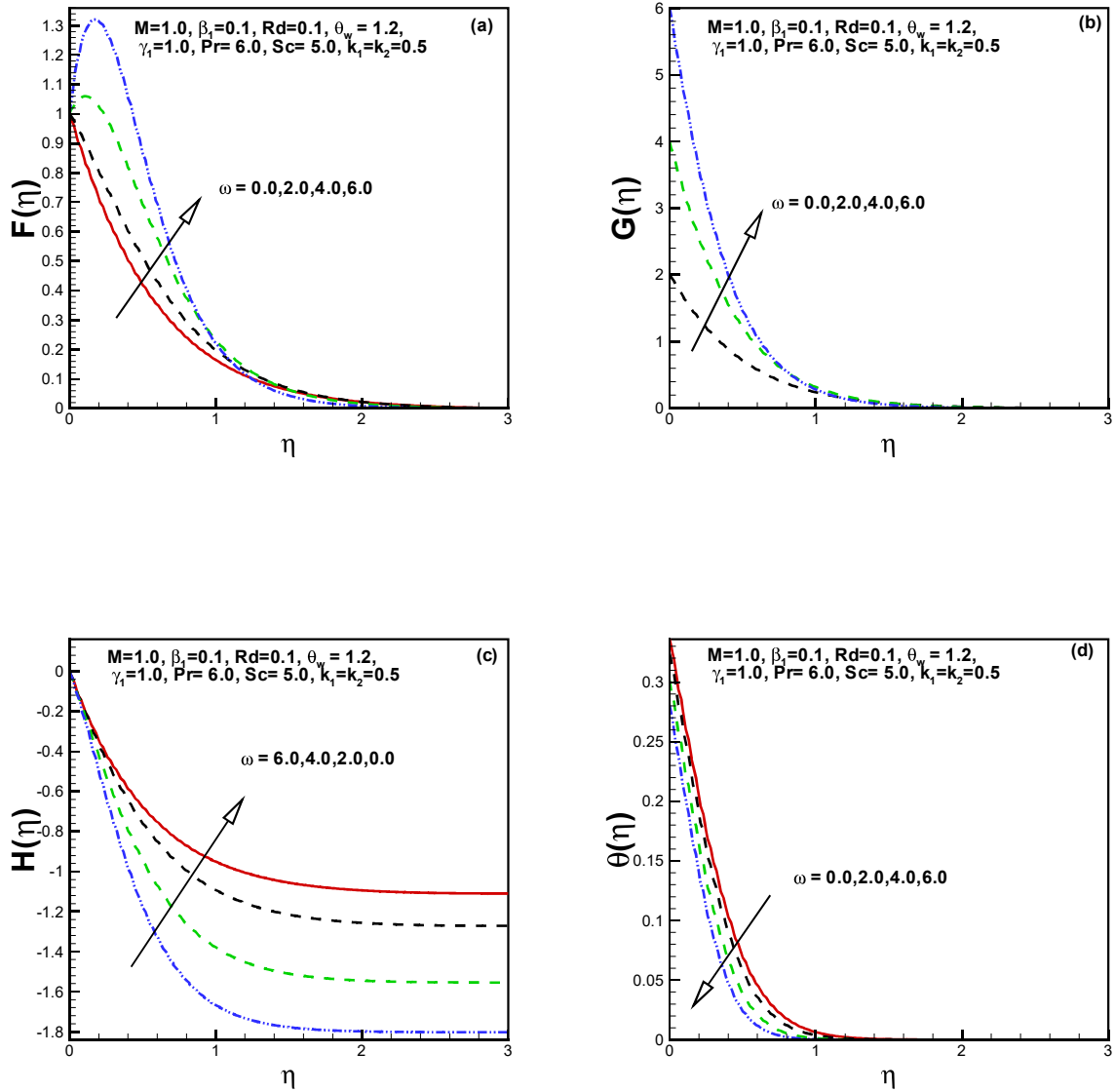| M	Rd	γ_1	θ_w	Pr	$Re^{-1/2} Nu_r$
0.0	0.1	2.0	1.5	7.0	1.715876272
2.0					1.663501612
4.0					1.612027607
6.0					1.563631490
1.0	0.1				1.689795665
	0.2				2.081612049
	0.3				2.422306755
	0.4				2.716546067
	0.1	0.5			0.599964479
		1.0			1.052505870
		1.5			1.406015906
		2.0			1.689795665
		1.0	1.2		0.893105670
			1.4		0.991436334
			1.6		1.122285799
			1.8		1.290299610
			1.2	1.0	0.500598705
				3.0	0.750051509
				5.0	0.841728890
				7.0	0.893105670

Fig. 4.1: F, G, H and θ for ω .
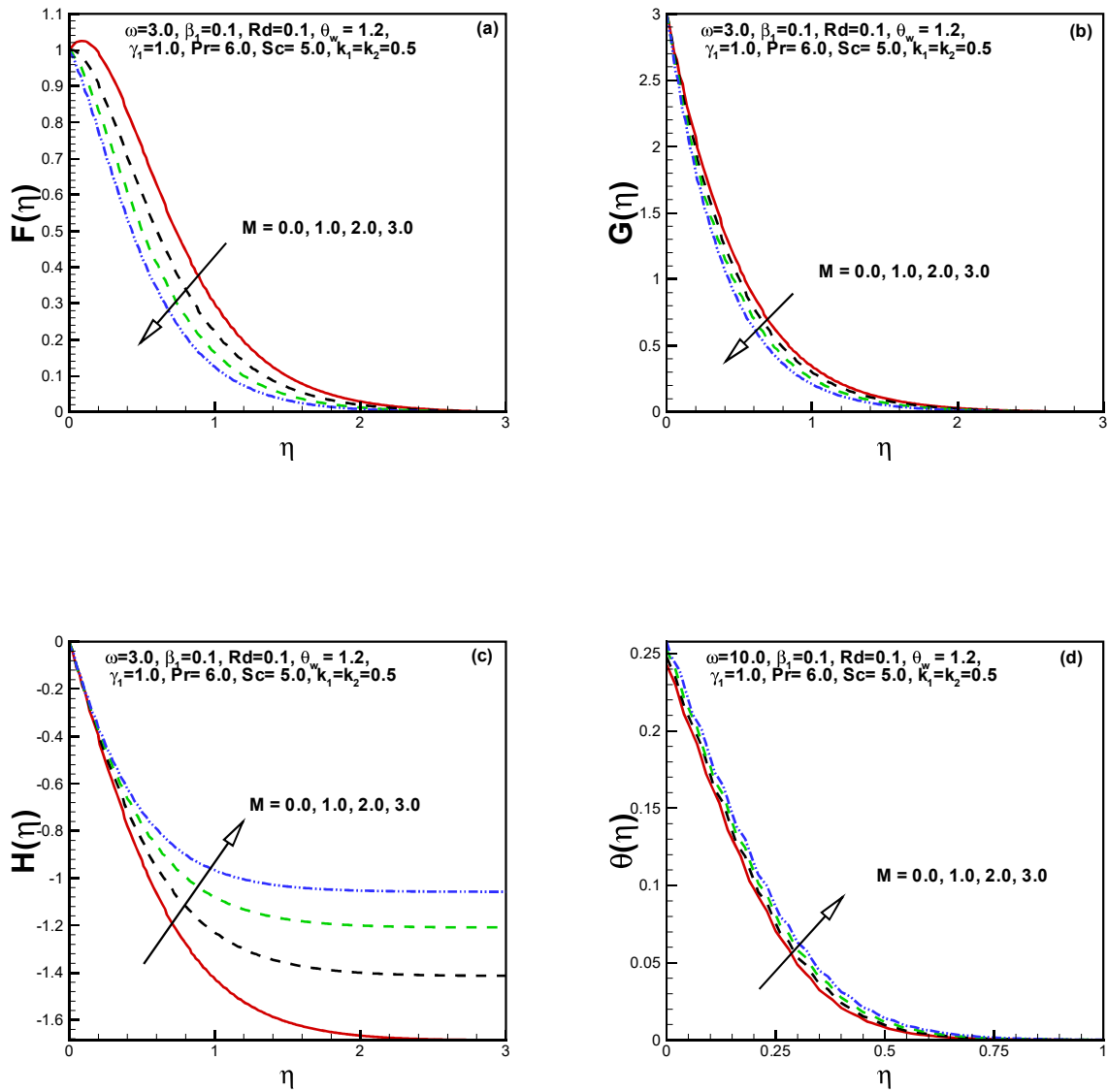
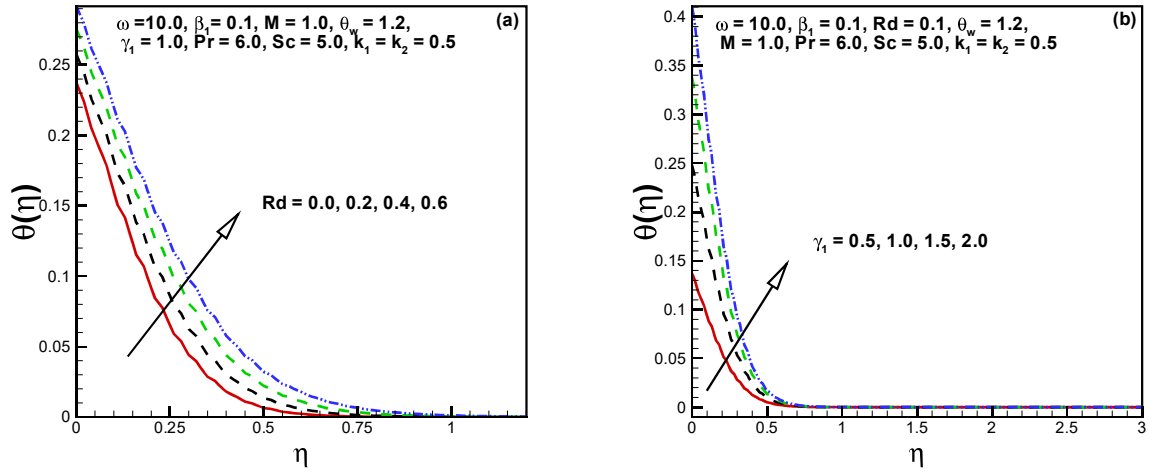**Fig. 4.2:** F, G, H and θ for M.
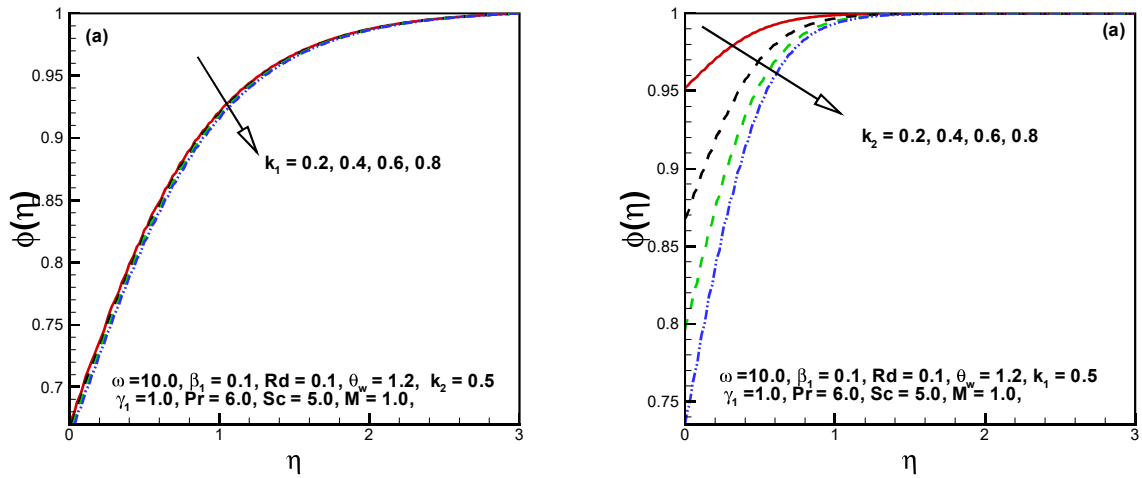
Fig. 4.3: θ for Rd and γ_1.

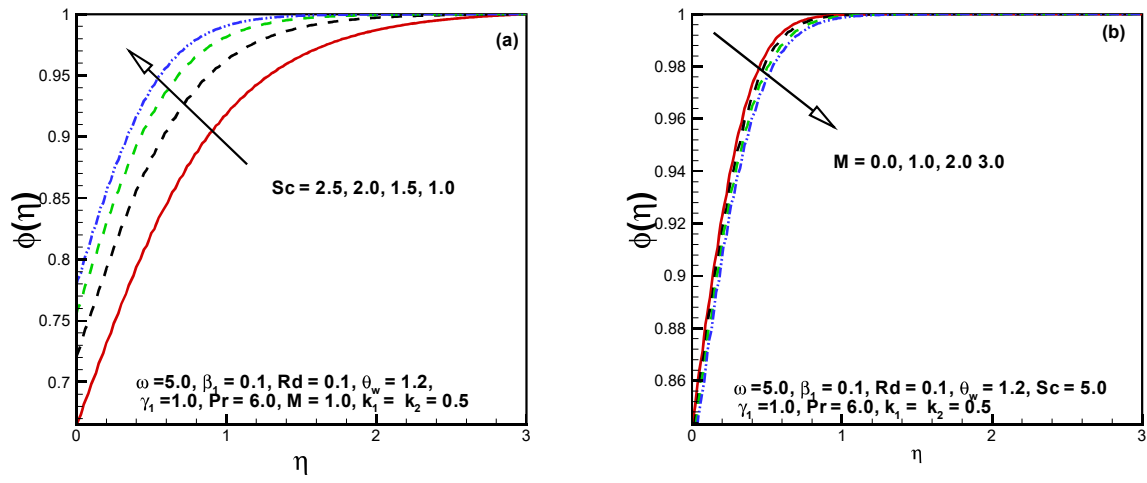**Fig. 4.4:** g for k_1 and k_2.

Fig. 4.5: g for Sc and M.

Chapter 5

Stagnation Point Flow of Maxwell Nanofluid

The concern here is to investigate the stagnation-point flow of Maxwell nanofluid over a porous radially stretching/shrinking rotating disk. An innovative revised Buongiorno's nanofluid model is used to track the thermophoresis and Brownian movement of the nanoparticles. The influences of variable thermal conductivity and heat source/sink are deliberated on nanofluid heat transfer features. Von Kármán similarity variables have been utilized to obtain the system of nonlinear ODEs comprising of continuity, momentum, energy and concentration equations. A built-in numerical procedure bvp4c is implemented for the numerical integration of the governing nonlinear problem. The results for the flow problem have been executed for the several physical parameters like rotation parameter, stretching/shrinking parameter, velocity ratio parameter, thermal conductivity parameter, suction/injection parameter, thermophoresis and Brownian motion parameters, heat source/sink parameter, Prandtl and Schmidt numbers. Based on the obtained results, it is evident that the radial velocity becomes higher with increasing value of velocity ratio parameter while reverse conduct is noticed for azimuthal velocity. Further, the heat transfer rate increases with decreasing value of thermophoresis parameter.

5.1 Problem Formulation

The schematic view of the porous rotating disk geometry is shown in **Fig. 2.1**. We consider the axisymmetric stagnation-point motion of Maxwell nanofluid develops from shrinking/stretching disk besides rotating. All the physical quantities are assumed to be independent of θ since the flow is axisymmetric about $z-$axis. The stagnation line is at $z = 0$ and the flow domain consists of the upper half plane filled with nanofluid. The disk is assumed to be stretching/shrinking radially in accordance with the velocity $u(r,0) = \lambda u_w$, where $u_w = cr$ and $\lambda > 0$ stands for disk stretching while $\lambda < 0$ for disk shrinking. Additionally, the disk is rotating in the anti-clockwise direction with velocity $v(r,0) = v_w = \Omega r$, where $\Omega(\geq 0)$ is the rotation rate. The nanoparticles volume fraction for the ambient fluid is C_∞. The Buongiorno's nanofluid model is treated to study the thermophoresis and Brownian motion. The assumptions of variable thermal conductivity and heat source/sink are taken. At the disk face with thermophoresis, the nanoparticles normal flux is considered to be zero. Within the framework of these axioms, the governing flow problem is given by

$$\frac{\partial}{\partial z}(w) + \frac{1}{r}\frac{\partial}{\partial r}(ru) = 0, \tag{5.1}$$

$$u\frac{\partial u}{\partial r} + w\frac{\partial u}{\partial z} - \frac{v^2}{r} = \nu\frac{\partial^2 u}{\partial z^2} + u_e\frac{du_e}{dr} - \lambda_1\left[u^2\frac{\partial^2 u}{\partial r^2} + w^2\frac{\partial^2 u}{\partial z^2} + 2uw\frac{\partial^2 u}{\partial r\partial z}\right.$$

$$\left. -\frac{2uv}{r}\frac{\partial v}{\partial r} - \frac{2vw}{r}\frac{\partial v}{\partial z} + \frac{uv^2}{r^2} + \frac{v^2}{r}\frac{\partial u}{\partial r}\right], \tag{5.2}$$

$$u\frac{\partial v}{\partial r} + w\frac{\partial v}{\partial z} + \frac{uv}{r} = \nu\frac{\partial^2 v}{\partial z^2} - \lambda_1\left[u^2\frac{\partial^2 v}{\partial r^2} + w^2\frac{\partial^2 v}{\partial z^2} + 2uw\frac{\partial^2 v}{\partial r\partial z}\right.$$

$$\left. +\frac{2uv}{r}\frac{\partial u}{\partial r} + \frac{2vw}{r}\frac{\partial u}{\partial z} - \frac{2u^2v}{r^2} - \frac{v^3}{r^2} + \frac{v^2}{r}\frac{\partial v}{\partial r}\right], \tag{5.3}$$

$$u\frac{\partial T}{\partial r} + w\frac{\partial T}{\partial z} = \frac{1}{\rho c_p}\frac{\partial}{\partial z}\left(k(T)\frac{\partial T}{\partial z}\right) + D_B\tau^*\left[\frac{D_T}{D_B T_\infty}\left(\frac{\partial T}{\partial z}\right)^2 + \frac{\partial T}{\partial z}\frac{\partial C}{\partial z}\right] + Q(T - T_\infty), \tag{5.4}$$

$$u\frac{\partial C}{\partial r} + w\frac{\partial C}{\partial z} = \frac{D_T}{T_\infty}\left(D_B\frac{T_\infty}{D_T}\frac{\partial^2 C}{\partial z^2} + \frac{\partial^2 T}{\partial z^2}\right), \tag{5.5}$$

with following conditions

$$u = \lambda u_w, \ v = v_w, \ w = w_0, \ T = T_w, \ \frac{\partial C}{\partial z} D_B + \frac{\partial T}{\partial z} \frac{D_T}{T_\infty} = 0 \text{ at } z = 0,$$

$$u = u_e = c_1 r, \ v = v_e \to 0, \ w = w_e = -2c_1 z, \ T = T_\infty, \ C = C_\infty \text{ as } z \to \infty. \qquad (5.6)$$

Taking into account the following similarity variables (cf. Chapter **2**)

$$u = crF, \ v = \Omega rG, \ w = \sqrt{c v} H, \ \eta = \sqrt{\frac{c}{v}} z,$$

$$\theta(\eta) = \frac{T - T_\infty}{T_w - T_\infty}, \ \phi(\eta) = \frac{C - C_\infty}{C_\infty}. \qquad (5.7)$$

By applying the similarity variables, Eqs. (5.1) to (5.6) reduce to the subsequent non-dimensional forms

$$H' + 2F = 0, \qquad (5.8)$$

$$F^2 - G^2 + HF' = F'' - \beta_1 \left(H^2 F'' + 2FF'H - 2HGG' \right), \qquad (5.9)$$

$$2FG + HG' = G'' - \beta_1 \left(H^2 G'' + 2FG'H + 2HGF' \right) + A^2, \qquad (5.10)$$

$$(1 + \varepsilon) \theta'' + \varepsilon \theta'^2 + \Pr \theta' \left(Nb\phi' - H \right) + \Pr Nt \ \theta'^2 + \Pr \delta_2 \theta = 0, \qquad (5.11)$$

$$\phi'' + \frac{Nt}{Nb} \theta'' - ScH\phi' = 0, \qquad (5.12)$$

$$F(0) = \lambda, \ G(0) = \omega, \ H(0) = S_w, \ \theta(0) = 1, \ \phi'(0) + \theta'(0)\frac{Nt}{Nb} = 0,$$

$$G(\infty) = 0, \ F(\infty) = A, \ \theta(\infty) = 0, \ \phi(\infty) = 0, \qquad (5.13)$$

where primes indicate the ordinary derivative with respect to η. The non-dimensional controlling parameters are the Deborah number $\beta_1 \left(= \lambda_1 \Omega \right)$, the velocity ratio parameter $\left(A = \frac{c_1}{c} \right)$, the heat source/sink $\delta_2 \left(= \frac{Q}{c\rho c_p} \right)$, the Prandtl number $\Pr \left(= \frac{v}{\alpha} \right)$, the Schmidt number $Sc \left(= \frac{\nu}{D_B} \right)$, the rotation parameter $\omega \left(= \frac{\Omega}{c} \right)$, the thermophoretic parameter $Nt \left(= \frac{\tau^* D_B (T_w - T_\infty)}{vT_\infty} \right)$, the Brownian motion parameter $Nb \left(= \frac{\tau^* D_B C_\infty}{v} \right)$, the suction/injection parameter $S_w \left(= \frac{w_0}{\sqrt{cv}} \right)$. The local

Nusselt number Nu_r is defined as

$$Nu_r = \frac{Rq_w}{k\left(T_w - T_\infty\right)}, \tag{5.14}$$

where

$$q_w = -k\left(\frac{\partial T}{\partial z}\right)|_{z=0}, \tag{5.15}$$

and dimensionless expression is

$$Re^{-1/2} Nu_r = -\theta'(0), \tag{5.16}$$

5.2   Solution Approach

This numerical integration of the nonlinear flow problem in Eqs. $(5.8 - 5.13)$ is accomplished through built-in scheme called bvp4c in Matlab with tolerance level of 10^{-3} and the consequences are exhibited through tables and graphs. In current bvp4c collacation method, Lobatto IIIA formula is employed. To obtain the numerical solution of Eqs. $(5.8 - 5.13)$, an appropriate set of guesses satisfying the boundary conditions are required. Once the initial guesses are provided then further iterations are performed by modifying these guesses with finite-difference scheme. To implement this method it is necessary to reduce the higher order ODEs into first order ODEs by familiarizing new variables. For conversion, we assume the following steps

$$H = \xi_1,\ F = \xi_2,\ F' = \xi_3,\ G = \xi_4,\ G' = \xi_5,\ \theta = \xi_6,\ \theta' = \xi_7,\ \phi = \xi_8,\ \phi' = \xi_9, \tag{5.17}$$

$$\xi_1' = \xi\xi_1, \xi\xi_1 = -2\xi_2, \tag{5.18}$$

$$\xi_2' = \xi_3,\ \xi_3' = \xi\xi_2, \tag{5.19}$$

$$\xi\xi_2 = \frac{\xi_2^2 - \xi_4^2 + \xi_1\xi_3 + \beta_1\left[(2\xi_1\xi_2\xi_3 - 2\xi_1\xi_4\xi_5) - \lambda^2\right]}{1 - \beta_1\xi_1^2}, \tag{5.20}$$

$$\xi_4' = \xi_5,\ \xi_5' = \xi\xi_3, \tag{5.21}$$

$$X_5' = \frac{2\xi_2\xi_4 + \xi_1\xi_5 + \beta_1\left[2\xi_1\xi_2\xi_3 + 2\xi_1\xi_2\xi_5\right]}{1 - \beta_1\xi_1^2}, \tag{5.22}$$

72

$$\xi_6' = \xi_7, \ \xi_7' = \xi\xi_4, \tag{5.23}$$

$$\xi\xi_4 = \frac{-\varepsilon\xi_7^2 - \Pr\left(Nb\xi_7\xi_9 + Nt\xi_7^2 - \xi_1\xi_7 + \delta\xi_6\right)}{1 + \varepsilon\xi_6}, \tag{5.24}$$

$$\xi_8' = \xi_9, \ \xi_9' = \xi\xi_5, \tag{5.25}$$

$$\xi\xi_5 = Sc\xi_1\xi_9 - \frac{Nt}{Nb}\xi\xi_4, \tag{5.26}$$

with conditions

$$\xi_1(0) = S_w, \ \xi_2(0) = \lambda, \ \xi_4(0) = \omega, \ \xi_6(0) = 1, \ \xi_9(0) + \frac{Nt}{Nb}\xi_7(0) = 0,$$

$$\xi_2(\infty) = A, \ \xi_4(\infty) = 0, \ \xi_6(\infty) = 0, \ \xi_8(\infty) = 0. \tag{5.28}$$

5.3   Results and Discussion

The flow around stagnation region in Maxwell nanofluid influenced by permeable rotating disk has been studied numerically in the presence of heat source/sink and variable thermal conductivity. The present study involves the dimensionless parameters namely; ω, λ, Nt, A, Nb, S_w, ε, Pr, δ, and Sc. This section illustrates the numerical and pictorial outputs for Nusselt number, concentration, temperature and velocity fields against the physical involved parameters.

Fig. 5.1(a) is displayed to visualize the impact of velocity ratio parameter A on radial velocity $F(\eta)$ when the disk is stretching ($\lambda = 0.2$) and shrinking ($\lambda = -0.2$). It is observed that radial flow amplifies with an intensification in A for both stretching/shrinking phenomena. As the parameter A is the ratio of velocities ar(free stream) to cr(stretching). It can be perceived physically that when the values of $A < 1$, the velocity cr will be dominant than the velocity ar which as a result enhances the flow in the radial flow. These curves also reveal that the value of radial velocity field is higher in case of shrinking disk ($\lambda = -0.2$) as compared to disk stretching ($\lambda = 0.2$). The outcomes of radial velocity $F(\eta)$ against the velocity ratio parameter A for the case of injection ($S_w = -0.5$) and suction ($S_w = 0.5$) are portrayed in Fig. 5.1(b). Here again the radial velocity is an increasing function of velocity ratio parameter A in both wall suction and injection parameters. We observe that the influence of suction parameter is to enhance the

radial flow as compared to the case of injection.

At a specified value of A, the effects of the rotation parameter ω , stretching/shrinking parameter λ and suction/ injection parameter S_w on the radial flow $F(\eta)$ are shown in **Figs. 5.2(a,b)**. It is revealed from **Fig. 5.2(a)** that radial velocity upsurges as rotation parameter ω rises. This is mainly due to the reason that the rotation parameter is the ratio of swirl Ω to stretch c rates. By boosting ω, the rotating effects becomes stronger as compared to stretching effects and as a result the centrifugal force becomes stronger. The impact of this force is to push the fluid in the radial direction which causes to enhance the radial velocity. Further, shrinking the disk have higher value of radial velocity field for away from the disk surface as compared to stretching effects . In **Fig. 5.2(b)**, it is observed that the impact of injection parameter is to reduce the radial velocity field as compared to suction parameter.

The curves of azimuthal velocity $G(\eta)$ for different values of velocity ratio parameter A are included in **Fig. 5.3(a)**. The numerical data is displayed for the disk stretching ($\lambda = 0.2$) and shrinking ($\lambda = -0.2$) cases. It can be noticed that the azimuthal velocity diminishes when the value of velocity ratio parameter becomes enlarge for both disk stretching and shrinking situations. However, the azimuthal velocity field appears to be greater marginally when the disk is operated at shrinking velocity than the stretching velocity. In **Fig. 5.3(b)**, the azimuthal velocity is sketched as a decreasing function of A for two different cases of injection ($S_w = -0.5$) and suction ($S_w = 0.5$) parameters. Here it is observed that the azimuthal velocity is lower for injection parameter as compared to suction parameter.

The impact of rotation parameter ω on stagnation pint flow for two different cases, that is, when the disk is stretching and shrinking is displayed in **Fig. 5.4(a)**. Since the rotation parameter is directly proportional to swirl rate. Therefore, enhancing the rotation parameter boosts up the disk rotation forcefully which as a result produces a fast fluid motion in the azimuthal direction. It is also obvious from these curves that impact of shrinking causes to increase the azimuthal flow when we compared with disk stretching. The impact of rotation parameter and suction and injection on azimuthal flow is disclosed on **Fig. 5.4(b)**. It is concluded that the influence of suction parameter ($S_w = 0.5$) is to intensify the azimuthal velocity component in comparison with injection parameter ($S_w = -0.5$).

In current analysis, the nanofluids properties are introduced by the parameters Nt and Nb.

74

The variation of Nt on temperature profile $\theta(\eta)$ curves is shown in **Fig. 5.5(a)**. The effect of temperature gradient have to tendency to accelerate the nanoparticles from warm to cold region. As the value of Nt increases, the $\theta(\eta)$ develops larger signifying an enhancement in the thermal field. Further, it is apparent from this figure that temperature profile is higher in case of disk shrinking ($\lambda = -0.2$) with respect to disk stretching ($\lambda = 0.2$). **Fig. 5.5(b)** exhibits the impact of Pr on the $\theta(\eta)$ with constant and variable variable thermal conductivity conditions. Temperature field $\theta(\eta)$ is observed to be a reducing function of Prandtl number Pr. This means that the flow with greater value of Prandtl number diminishes the heat distribution in the fluid. Physically, growing values of Prandtl number indicates weaker thermal diffusivity which results in thinning the penetration depth of temperature. It can also be inferred that the assuming thermal conductivity as a function of temperature has higher value in heat transfer mechanism. The heat generation/absorption parameter δ plays a useful role in changing the fluid temperature. The value ($\delta > 0$) depicts the situation when there is a heat source and the case ($\delta < 0$) represents the condition of heat sink. It is apparent from **Fig. 5.5(c)** that increasing values of heat source rise the fluid temperature and thermal boundary layer thickness. On the other hand, growing values of heat sink parameter causes to reduce the fluid temperature in boundary layer flow of Maxwell fluid.

Fig. 5.6(a) exposes the nanoparticle concentration $\phi(\eta)$ for cumulative values of thermophoresis parameter Nt. Nanoparticles concentration $\phi(\eta)$ shows a progressing trend with variation in Nt. It is also indicated that by enlarging the Brownian motion parameter Nb from 0.5 to 0.7, a considerable reduction in concentration profile is observed. The features of Sc with various values on $\phi(\eta)$ is sketched in **Fig. 5.6(b)**. An inverse relation exists between the Schmidt number Sc and Brownian diffusion coefficient D_B. Therefore, concentration profile $\phi(\eta)$ and related boundary layer thickness decay with escalating values of Schmidt number Sc.

Figs. 5.7(a,b) are exposed to show the isotherms for disk shrinking ($\lambda = -0.2$) and stretching ($\lambda = 0.2$) cases, respectively. In **Figs. 5.8(a,b)** the isotherms are drawn for the thermal conductivity parameter $\varepsilon = 0.0$ and $\varepsilon = 1.0$.

Table 5.1 is organized to study the impact of physical parameters on the surface heat flux $-\theta'(0)$. It is seen that heat transfer rate $-\theta'(0)$ boosts up significantly with escalating values of rotation parameter ω, stretching/shrinking parameter λ, velocity ratio parameter A, and

suction parameter S_w. However, the roles of thermal conductivity parameter ε, thermophoresis parameter Nt, and heat source parameter δ are quite beneficial in reducing the heat transfer rate.

Table 5.1: The Nusselt number $-\theta'(0)$ values when $\beta_1 = 0.1$, $\mathrm{Pr} = 3.0$, $Nb = 0.5$, and $Sc = 1.5$.

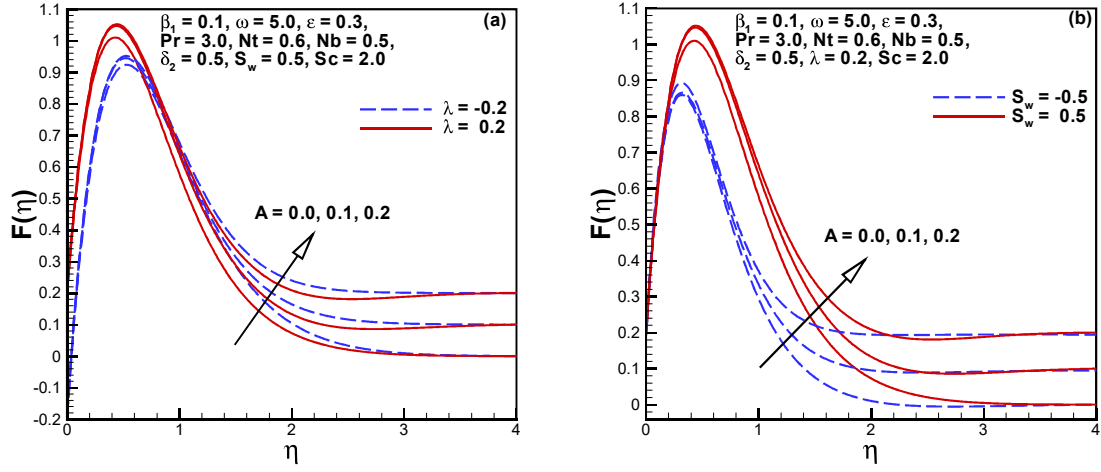| λ	A	ω	S_w	ε	Nt	δ	
1.0	0.1	5.0	0.4	0.2	0.6	0.5	$-\theta'(0)$
-1.5							0.4268873
-1.3							0.3166374
-1.0							0.1528901
1.0							0.7644015
1.3							0.8538346
1.5							0.9823639
	0.0						0.8433533
	0.1						0.8538346
	0.2						0.8667719
		1.0					0.3065634
		2.0					0.4520842
		3.0					0.5991248
			0.0				1.289064
			0.2				1.062991
			0.4				0.8538346
				0.3			0.8165573
				0.6			0.7273971
				0.9			0.6607102
					0.1		0.937258
					0.4		0.8898072
					0.7		0.8343712
						0.0	1.244686
						0.2	1.098932
						0.5	0.8538346

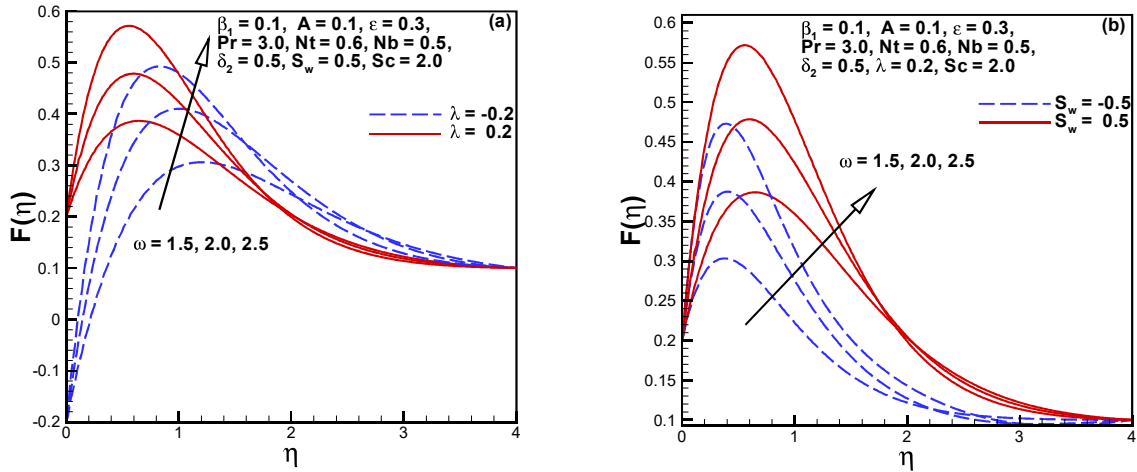**Fig. 5.1:** F for A, λ and S_w.
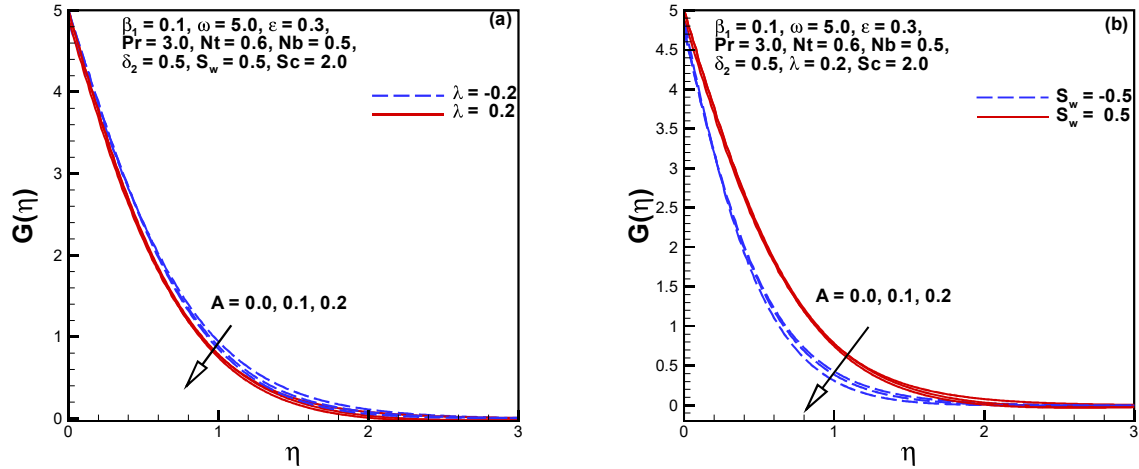

Fig. 5.2: F for ω, λ and S_w.
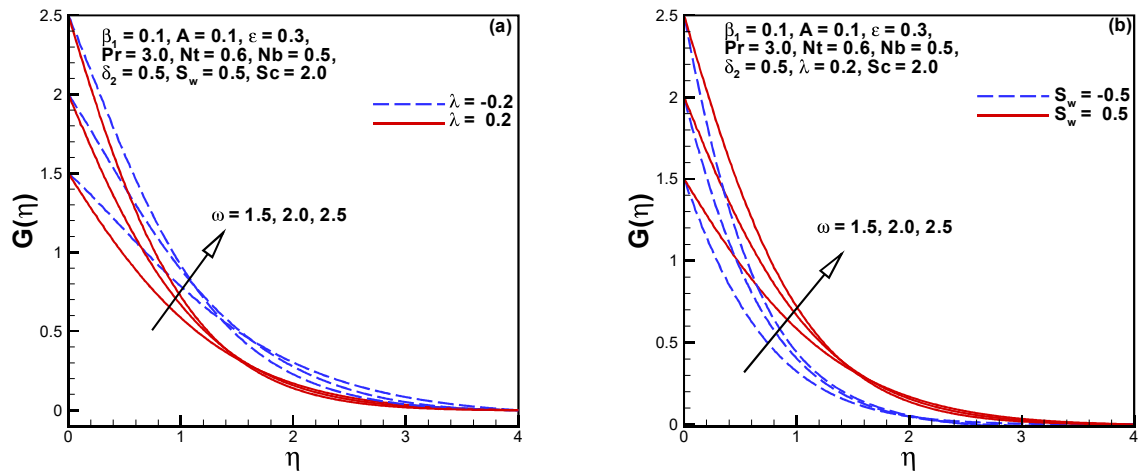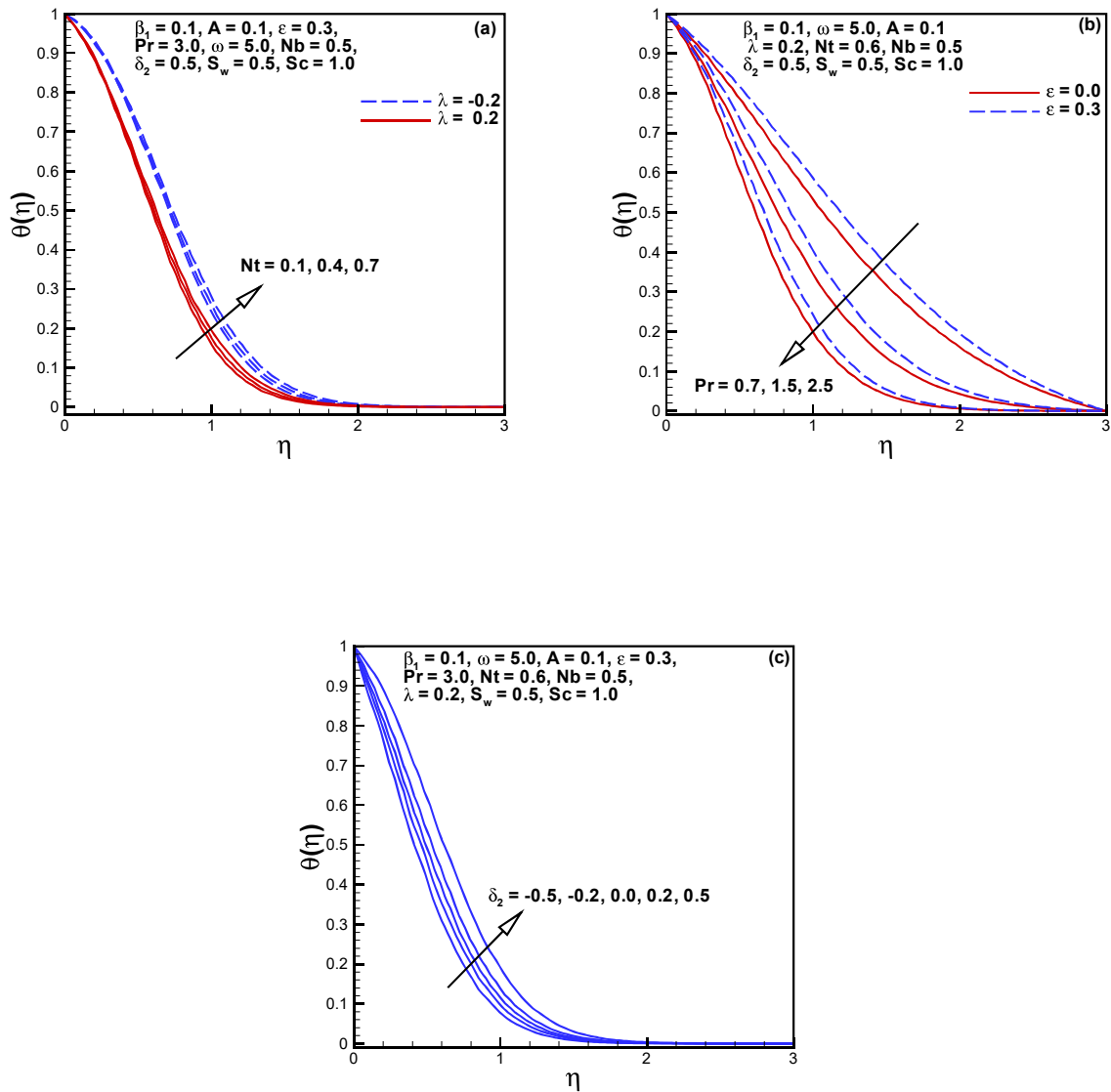
Fig. 5.3: G for A, λ and S_w.

Fig. 5.4: G for ω, λ and S_w.

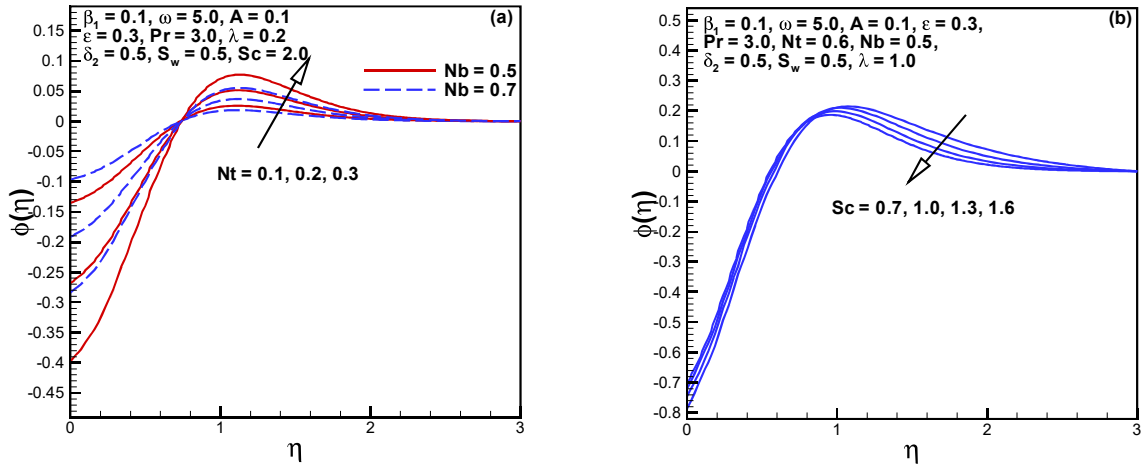**Fig. 5.5:** θ for Nt, λ, Pr, ε and δ_2 .
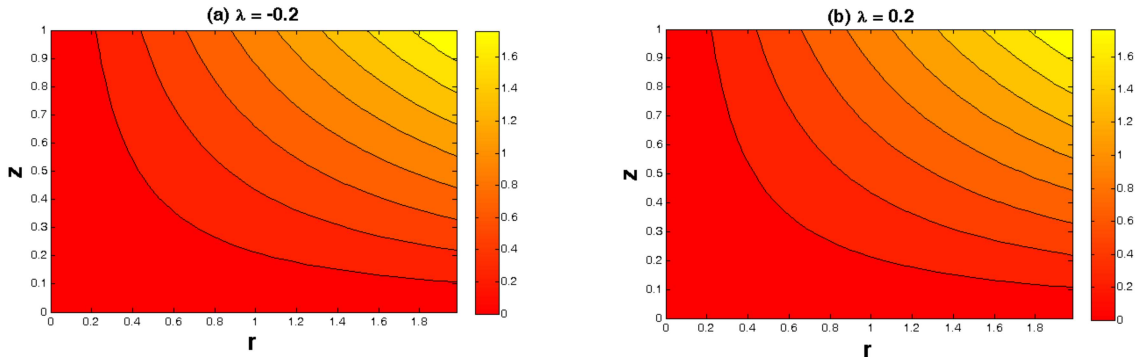
Fig. 5.6: ϕ for Nt, Nb and Sc .
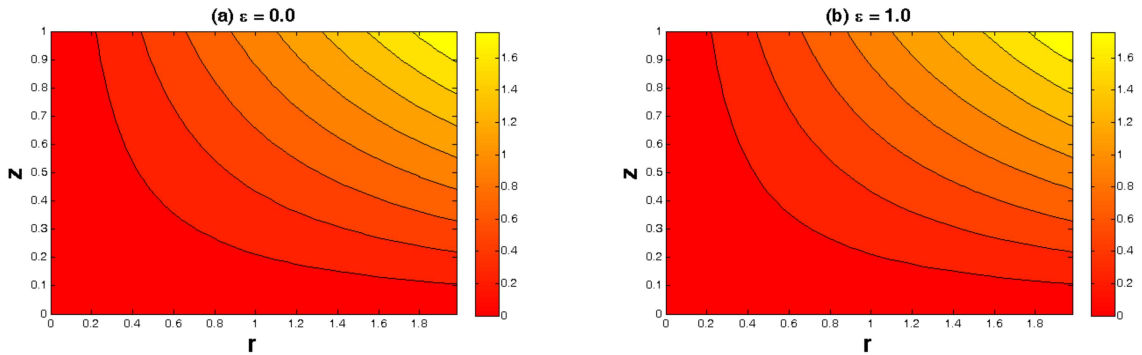

Fig. 5.7: Isotherms for λ.

Fig. 5.8: Isotherms for ε.

Chapter 6

Transient Thin Film Flow of Nonlinear Radiative Maxwell Nanofluid over a Rotating Disk

In this chapter, a mathematical model for transient nature thin film flow of Maxwell nanofluid over a rotating disk is studied in the presence of a uniform magnetic field and non-linear thermal radiation. The Brownian motion and thermophoresis features due to nanofluid are captured by adopting the Buongiorno model. The prime emphasize is to explore the temperature field and nanoparticles volume fraction in nanofluid thin film flow. The numerical outcomes regarding film thickness, Nusselt number, Sherwood number, flow, thermal and solutal profiles are revealed for varying estimation of involved physical parameters. It is shown that the film thickness minimizes with augmenting magnetic number. Further, the impacts of thermophoresis and thermal radiation parameters are worthwhile in enhancing the fluid temperature. The solute concentration is found to decrease with Brownian motion and Schmidt number.
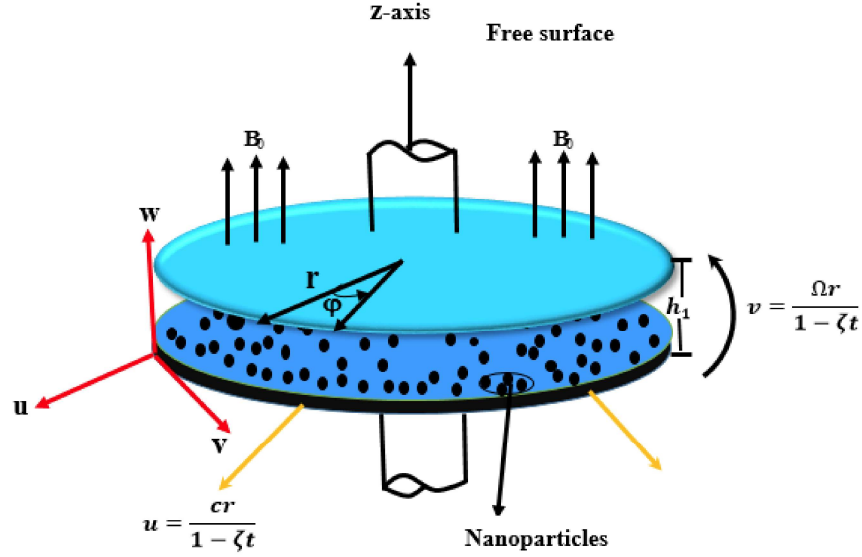
6.1 Flow Configuration

Fig. 6.1: Schematic of the physical system.

6.2 Mathematical Description

The Maxwell nanofluid with thin layer rotating caused by time dependent revolution of disk with angular velocity Ω is focused. The system (r, φ, z) of cylindrical coordinates is adopted for the mathematical description of the problem as shown in **Fig. 6.1**.

The liquid film with uniform thickness h_1 is lying horizontally on the rotating disk surface. The stretching velocity of disk is taken to be $u = \frac{cr}{1-\zeta t}$, where c is the stretching rate and ζ a constant. The disk rotating velocity is assumed to be $v = \frac{\Omega r}{1-\zeta t}$, . The surface temperature of the disk T_s is defined by

$$T_s = T_0 - T_{ref} \frac{\Omega r^2}{\nu (1 - \zeta t)^{3/2}}, \tag{6.1}$$

where the temperature at the origin is denoted by T_0 and constant reference temperature is assumed as T_{ref}. Along vertical direction, a magnetic beam $B(t) = B_0/\sqrt{1 - \zeta t}$ is projected on liquid thin film motion. Moreover, the concentration at the disk surface C_s is given by

$$C_s = C_0 - C_{ref} \frac{\Omega r^2}{\nu (1 - \zeta t)^{3/2}}, \tag{6.2}$$

where the concentrations at location $(0,0,0)$ is C_0 and at reference is C_{ref}. The heat transfer analysis is performed in the presence of nonlinear thermal radiations. The Brownian motion and thermophoresis features are incorporated due to nanoparticles using Buongiorno model. The above hypotheses yield the subsequent equations

$$\frac{1}{r}\frac{\partial}{\partial r}(ru) + \frac{\partial}{\partial z}(w) + 0, \tag{6.3}$$

$$\frac{\partial u}{\partial t} - \frac{v^2}{r} + w\frac{\partial u}{\partial z} + u\frac{\partial u}{\partial r} + \lambda_1\left(\frac{\partial^2 u}{\partial t^2} + u^2\frac{\partial^2 u}{\partial r^2} + 2u\frac{\partial^2 u}{\partial r\partial t} - 2\frac{v}{r}\frac{\partial v}{\partial t} + 2w\frac{\partial^2 u}{\partial z\partial t} - \frac{2uv}{r}\frac{\partial v}{\partial r} + \frac{uv^2}{r^2}\right.$$

$$\left. +2uw\frac{\partial^2 u}{\partial r\partial z} - \frac{2vw}{r}\frac{\partial v}{\partial z} + w^2\frac{\partial^2 u}{\partial z^2} + \frac{v^2}{r}\frac{\partial u}{\partial r}\right) = \nu\left(\frac{\partial^2 u}{\partial z^2}\right) - \frac{\sigma B_0^2}{\rho(1-\zeta t)}\left(u + \lambda_1\left(\frac{\partial u}{\partial t} + w\frac{\partial u}{\partial z}\right)\right),$$
$$\tag{6.4}$$

$$\frac{\partial v}{\partial t} + \frac{uv}{r} + w\frac{\partial v}{\partial z} + u\frac{\partial v}{\partial r} + \lambda_1\left(\frac{\partial^2 v}{\partial t^2} + 2u\frac{\partial^2 v}{\partial r\partial t} + 2\frac{v}{r}\frac{\partial u}{\partial t} + 2w\frac{\partial^2 v}{\partial z\partial t} + u^2\frac{\partial^2 v}{\partial r^2} - \frac{2u^2 v}{r^2} + \frac{2uv}{r}\frac{\partial u}{\partial r}\right.$$

$$\left. +2uw\frac{\partial^2 v}{\partial r\partial z} - \frac{v^3}{r^2} + \frac{2vw}{r}\frac{\partial u}{\partial z} + \frac{v^2}{r}\frac{\partial v}{\partial r} + w^2\frac{\partial^2 v}{\partial z^2}\right) = \nu\left(\frac{\partial^2 v}{\partial z^2}\right) - \frac{\sigma B_0^2}{\rho(1-\zeta t)}\left(v + \lambda_1\left(\frac{\partial v}{\partial t} + w\frac{\partial v}{\partial z}\right)\right),$$
$$\tag{6.5}$$

$$\frac{\partial T}{\partial t} + w\frac{\partial T}{\partial z} + u\frac{\partial T}{\partial r} = \alpha\left(\frac{\partial^2 T}{\partial z^2}\right) + \tau^*\left(D_B\frac{\partial T}{\partial z}\frac{\partial C}{\partial z} + \frac{D_T}{T_0}\left(\frac{\partial T}{\partial z}\right)^2\right) + \frac{16\sigma^*}{3\rho c_p k^*}\frac{\partial}{\partial z}\left(T^3\frac{\partial T}{\partial z}\right), \tag{6.6}$$

$$\frac{\partial C}{\partial t} + w\frac{\partial C}{\partial z} + u\frac{\partial C}{\partial r} = \frac{D_T}{T_0}\left(D_B\frac{T_0}{D_T}\frac{\partial^2 C}{\partial z^2} + \frac{\partial^2 T}{\partial z^2}\right), \tag{6.7}$$

where λ_1 is the relaxation time parameter, T the fluid temperature, C the fluid concentration, τ^* the heat capacities ratio, D_B the Brownian diffusion coefficient, and D_T the thermophoresis diffusion coefficient. Expressing the boundary conditions

$$(u, v, w, T, C) = \left(\frac{cr}{1-\zeta t}, \frac{r\Omega}{1-\zeta t}, 0, T_s, C_s\right) \text{ at } z = 0,$$

$$w = \frac{\partial h_1}{\partial t} + u\frac{\partial h_1}{\partial r}, \frac{\partial u}{\partial z} = \frac{\partial v}{\partial z} = 0, \frac{\partial T}{\partial z} = \frac{\partial C}{\partial z} = 0 \text{ at } z = h_1. \tag{6.8}$$

Defining the similarity quantities

$$u = f'(\eta)\frac{r\Omega}{1-\zeta t}, \quad v = g(\eta)\frac{r\Omega}{1-\zeta t}, \quad w = -2f(\eta)\left(\frac{\nu\Omega}{1-\zeta t}\right)^{1/2}, \quad \eta = \left(\frac{\Omega}{\nu(1-\zeta t)}\right)^{1/2}z,$$

$$h_1(t) = \left(\frac{\nu}{\Omega}\right)^{1/2} (1 - \zeta t)^{1/2} \beta, T = T_0 - T_{ref} \frac{\Omega r^2}{\nu (1 - \zeta t)^{3/2}} \theta(\eta), C = C_0 - C_{ref} \frac{\Omega r^2}{\nu (1 - \zeta t)^{3/2}} \phi(\eta).$$

(6.9)

Substituting Eqs. (6.9) into Eqs. (6.3 − 6.8), we obtain

$$f''' - S\left(f' + \frac{\eta}{2}f''\right) - \left(f'^2 - g^2 - 2ff''\right) - \beta_1\left(S^2\left(2f' + \frac{7}{4}\eta f'' + \frac{1}{4}\eta^2 f'''\right)\right. +$$

$$S\left(2f'^2 - 2g^2 - 6ff''\right) + \eta S\left(f'f'' - gg' - 2ff'''\right) - 4ff'f'' + 4f^2 f''' - 4fgg'\right)$$

$$-M\left(f' + \beta_1\left(Sf' + \frac{1}{2}\eta Sf'' - 2ff''\right)\right) = 0,$$

(6.10)

$$g'' - S\left(g + \frac{\eta}{2}g'\right) - 2\left(f'g - fg'\right) - \beta_1\left(S^2\left(2g + \frac{7}{4}\eta g' + \frac{1}{4}\eta^2 g''\right)\right. +$$

$$S\left(4f'g - 6fg'\right) + \eta S\left(f'g' + f''g - 2fg''\right) - 4ff'g' - 4ff''g + 4f^2 g''\right)$$

$$-M\left(g + \beta_1\left(Sg + \frac{1}{2}S\eta g' - 2fg'\right)\right) = 0,$$

(6.11)

$$\left(1 + \frac{4}{3}Rd\right)\theta'' + \frac{4}{3}Rd\left[(\theta_w - 1)^3\left(3\theta^2\theta'^2 + \theta^3\theta''\right) + 3(\theta_w - 1)^2\left(2\theta\theta'^2 + \theta^2\theta''\right)\right.$$

$$+3(\theta_w - 1)\left(\theta'^2 + \theta\theta''\right)\right] + 2\Pr\left(f\theta' - f'\theta\right) - \frac{1}{2}\Pr S\left(\eta\theta' + 3\theta\right) + \Pr\left(Nt \, \theta'^2 + Nb\theta'\phi'\right) = 0,$$

(6.12)

$$\phi'' - \frac{1}{2}Sc\left(3\phi + \eta\phi'\right)S - 2Sc\left(f'\phi - f\phi'\right) + \theta''\frac{Nt}{Nb} = 0,$$

(6.13)

with conditions

$$f'(0) = \omega, \; g(0) = 1, \; f(0) = 0, \; \theta(0) = 1, \; \phi(0) = 1,$$

$$f(\beta) = \frac{S\beta}{4}, \; f''(\beta) = 0, \; g'(\beta) = 0, \; \theta'(\beta) = 0, \; \phi'(\beta) = 0.$$

(6.14)

where the dimensionless parameter $S = \frac{a}{\Omega}$ is the measure of unsteadiness, $M = \frac{\sigma B_0^2}{\rho \Omega}$ the magnetic parameter, $\beta_1 = \frac{\lambda_1 \Omega}{1 - \zeta t}$ the Deborah number, $N_b = \frac{\tau^* D_B (C_0 - C_s)}{v}$ the Brownian motion parameter, $\Pr = \frac{v}{\alpha}$ the Prandtl number, $\theta_w = \frac{Ts}{T_0}$ the temperature ratio parameter, $Rd = \frac{4\sigma^* T_0^3}{kk^*}$ the radiation parameter, $N_t = \frac{\tau^* D_T (T_0 - T_s)}{T_0 v}$ the thermophoresis parameter, $Sc = \frac{\nu}{D_B}$ the Schmidt number and $\omega = \frac{c}{\Omega}$ the rotation parameter. Further, β denotes the value of the similarity variable η at the

free surface. Thus Eq. (6.9) gives

$$\beta = \left(\frac{\Omega}{\nu\left(1 - \zeta t\right)}\right)^{1/2} h_1. \tag{6.15}$$

The Nusselt numbers Nu_r and Sherwood number Sh_r are defined as

$$Nu_r = -\left(1 + \frac{16\sigma^* T^3}{3kk^*}\right) \frac{R\left(\frac{\partial T}{\partial z}\right)|_{z=0}}{(T_w - T_\infty)}, \ Sh_r = -\frac{R\left(\frac{\partial C}{\partial z}\right)|_{z=0}}{(C_w - C_\infty)}, \tag{6.16}$$

and dimensionless expressions of these quantities are

$$Re^{-1/2} \ Nu_r = -\left(1 + \frac{4}{3}Rd\left\{1 + (\theta_w - 1)\theta(0)\right\}^3\right)\theta'(0), \ Re^{-1/2} \ Sh_r = -\phi'(0), \tag{6.17}$$

where $Re = \frac{R^2\Omega}{v(1-\zeta t)}$ is the Reynolds number.

6.3 Results and Discussion

The dimensionless nonlinear momentum, temperature and concentration Eqs. $(6.10 - 6.13)$ with conditions in Eq. (6.14) are considered for the numerical computations. The numerical scheme bvp4c with tolerance level of 10^{-3} is followed to characterize the flow, temperature and concentration profiles in the form of graphs. The graphical significance of the active parameters on velocity components (radial $f'(\eta)$, azimuthal $g(\eta)$ and axial $f(\eta)$), temperature $\theta(\eta)$ and nanoparticles volume fraction $\phi(\eta)$, Nusselt $\frac{Nu_r}{Re^{0.5}}$ and Sherwood $\frac{Sh_r}{Re^{0.5}}$ numbers for some selected values is demonstrated through **Figs. (2-6)**.

In **Figs. 6.2(a,b)**, we showed the radial, and azimuthal velocities for diverse estimations of β_1. For small β_1, the shorter will be the recovery duration and material acts like a purely viscous fluid. However, a material having higher Deborah number will have larger relaxation time and solid like response is shown by the material. The radial and azimuthal velocities decrease gradually against increasing values of η. It is obvious as the Deborah number enlarges, that is, the fluid relaxation time parameter increases, profiles related with $f'(\eta)$ and $g(\eta)$ diminish.

The thermophoresis parameter Nt affect with varying values on $\theta(\eta)$ is shown in **Fig. 6.3(a)**. In nanofluid the ratio between nanoparticle diffusion and thermophoretic force to the momentum

diffusion is referred to thermophoresis number Nt. By enlarging the thermophoresis parameter, the temperature distribution increases in thin film nanofluid flow. The characteristics of parameter corresponding to radiation Rd are sketched in **Fig. 6.3(b)** for $\theta(\eta)$. It is evident from the sketches that an enhancement occurs in fluid temperature under an escalating values of Rd. This trend is legitimate for linear as well as for nonlinear thermal radiations. In fact, more heat is provided to the liquid by flourishing the thermal radiation effects which leads to promote the profile of $\theta(\eta)$ in thin film flow. The role of thermal radiation is quite significant in boosting up heat transfer rate.

Figs. 6.4(a,b) represent the isotherms patterns for the values $Rd = 0.0$ and $Rd = 1.0$, respectively, by taking $T_0 = 0.01$. It is observed that by moving in the radial and azimuthal directions, simultaneously the temperature starts increasing. It is clear that the value of the temperature is maximum at $r = z = 1$. The same behavior is depicted for $Rd = 1.0$ in **Fig. 6.4(b)**. Closely observed that at $r = z = 1$, the hotter region is greater for $Rd = 1.0$ than that of $Rd = 0.0$.

Fig. 6.5(a) depicts that an intensifying values of Sc reduces the concentration field and associated boundary layer thickness. Schmidt number Sc can be defined as the ratio of momentum diffusivity to the Brownian diffusion coefficient D_B. When the values of Sc become larger, the coefficient of Brownian diffusion diminishes which results in a reduction in nanoparticles volume fraction $\phi(\eta)$. The plots of nanoparticles volume fraction $\phi(\eta)$ with Brownian motion parameter Nb are revealed in **Fig. 6.5(b)**. These curves show a decreasing trend when the value of Nb increases.

The expression of heat transport $Nu_r Re^{-1/2}$ is sketched in **Fig. 6.6(a)** with different effective parameters like the radiation and temperature ratio parameters. The impact of radiation and thermophoresis parameters is to increase the Nusselt number. **Fig. 6.6(b)** is displayed to speculate the influence of M and S on film thickness β. It is noticed that β decreases with increasing value of M and S. **Table 6.1** demonstrates the numerical data regarding the film thickness parameter β with a variation in S, M and β_1. It is observed that the film thickness decreases with S, M and β_1.

Table 6.1: Variations of film thickness β for different values of S, M, and β_1 when $\omega = 1.0$.

S	M	β_1	β
1.2	1.0	0.1	1.832088
1.4			1.552972
1.6			1.335090
1.0	1.0		2.225809
	2.0		1.907348
	3.0		1.696364
	1.0	0.0	2.473066
		0.1	2.225809
		0.2	2.042126
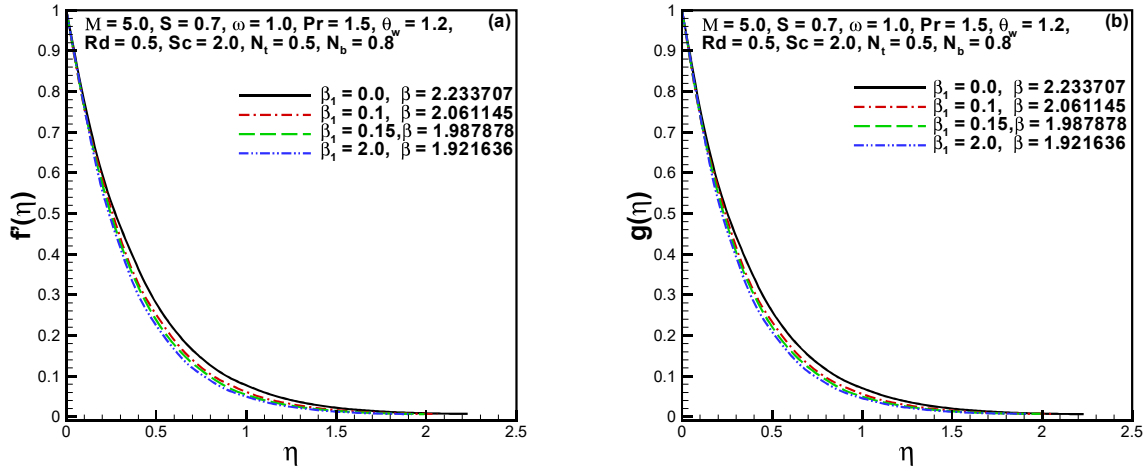
Fig. 6.2: f' and g for β_1.
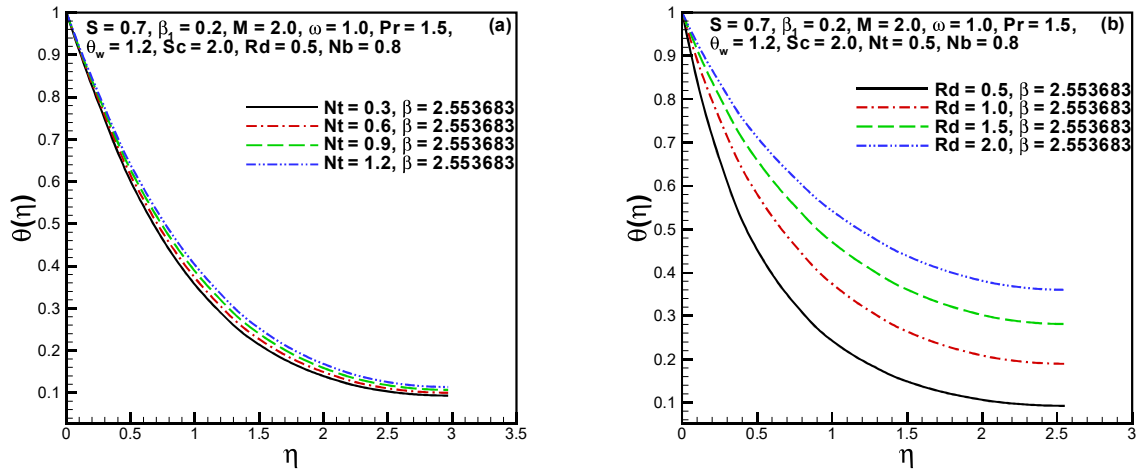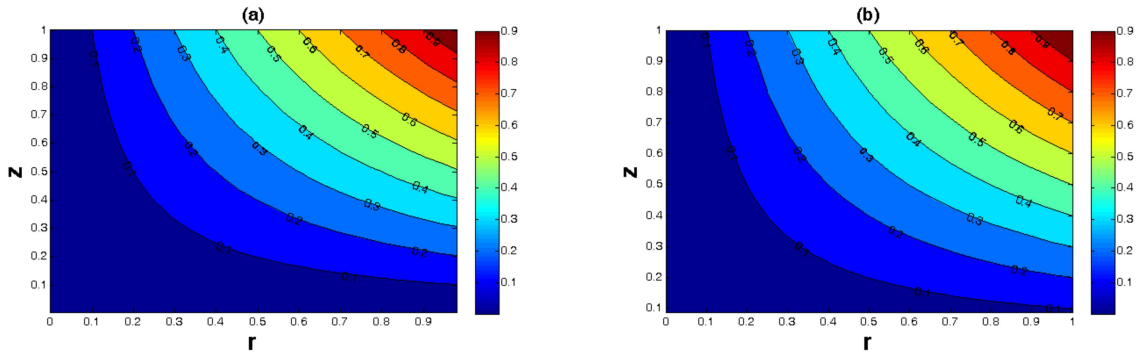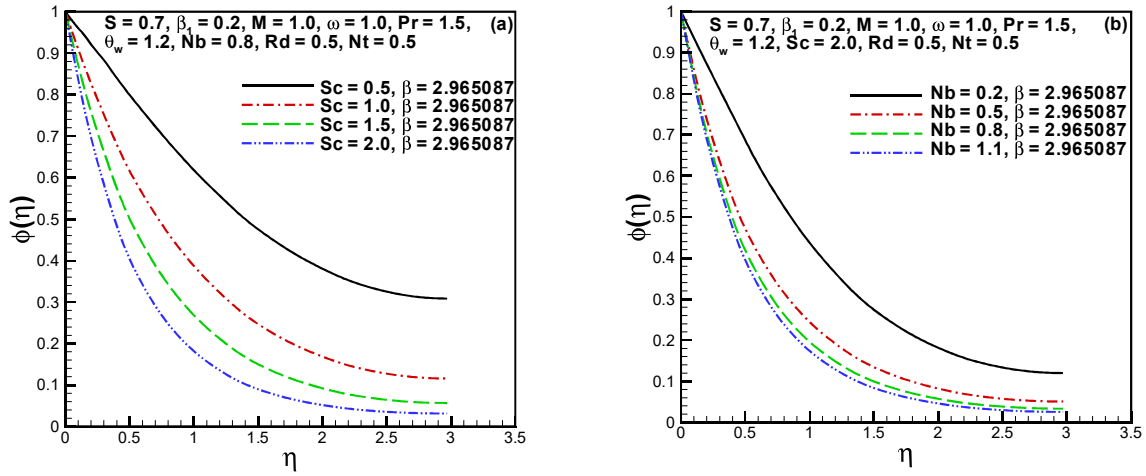

Fig. 6.3: θ for Nt and Rd.

Fig. 6.4: Isotherms for (a) $Rd = 0.0$ and (b) $Rd = 1.0$, when $S = 0.7, M = 1.0,$ $\beta_1 = 0.1,$ $\omega = 1.0,$ $\Pr = 1.5,$ $\theta_w = 1.2,$ $Sc = 3.0,$ $Nt = 0.5,$ $Nb = 1.0$ and $\beta = 3.223446.$
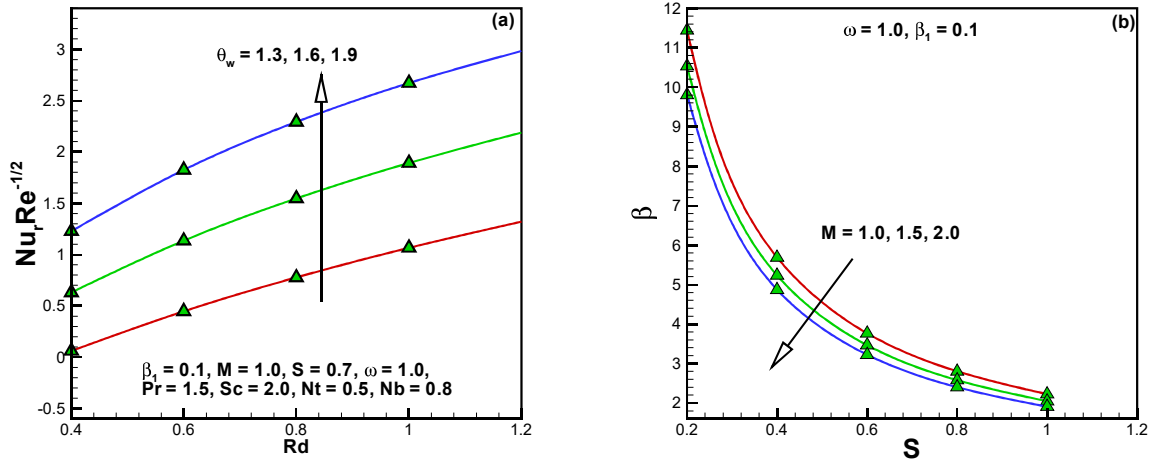

Fig. 6.5: ϕ for Sc and $Nb.$

Fig. 6.6: (a) Nu_r for θ_w and Rd and (b) β for M and S.

Chapter 7

Impact of Activation Energy in Thin Film Flow of Maxwell Nanofluid

The current chapter aims to study the unsteady finite thin film flow of upper convected Maxwell (UCM) fluid due to horizontal rotating disk in the presence of nanoparticles. The development of thin conducting liquid film is investigated under the impacts of non-linear thermal radiations, variable magnetic field, and Joule heating. A significant perspective of this attempt is to incorporate the features of exothermic chemical reaction with activation energy for Buongiorno's model of nanofluid owing to their improved heat transfer. The non-dimensional analysis is performed to acquire the ordinary differential equations. A finite difference base numerical scheme namely bv4c is implemented for the numerical simulation of the nonlinear problem. The physical consequence of the active parameters, that influenced the model, are argued through graphs. The obtained results intimate that nanofluid film thickness decays with the growing values of magnetic field, unsteadiness parameter and Deborah number. It is noted that the nanoparticles volume fraction increases with incremented values of activation energy parameter. Moreover, the nanofluid temperature shows a remarkable enhancement with the thermophoresis parameter.

7.1 Problem Formulation

Consider the magnetohydrodynamic (MHD) time dependent electrically conducting thin film flow of upper convected Maxwell nanofluid over a stretchable rotating disk. The motion of fluid is due to stretching as well as rotating phenomena as display in flow setup (**Fig. 6.1**).

A uniform liquid film of thickness $h_1(r,t)$ is formed horizontally on the surface of rotating disk. The disk stretching and rotating velocities, temperature and concentration vary with space and time.

The vertical flow is impacted with the magnetic beam $B(t) = B_0/\sqrt{1-\zeta t}$. The process of heat transfer is carried out in the presence of nonlinear thermal radiations and Joule heating. The Buongiorno model is used to study the features of nanoparticles described by Brownian motion and thermophoresis quantities. The above assumptions together with species chemical reaction and Arrhenius activation energy lead the following system of governing equations

$$\frac{\partial}{\partial z}(w) + \frac{1}{r}\frac{\partial}{\partial r}(ru) = 0, \tag{7.1}$$

$$\frac{\partial u}{\partial t} + u\frac{\partial u}{\partial r} + w\frac{\partial u}{\partial z} - \frac{v^2}{r} + \lambda_1\left(\frac{\partial^2 u}{\partial t^2} + u^2\frac{\partial^2 u}{\partial r^2} + 2u\frac{\partial^2 u}{\partial r\partial t} - 2\frac{v}{r}\frac{\partial v}{\partial t} + 2w\frac{\partial^2 u}{\partial z\partial t} - \frac{2uv}{r}\frac{\partial v}{\partial r} + \frac{uv^2}{r^2}\right.$$

$$\left. +2uw\frac{\partial^2 u}{\partial r\partial z} - \frac{2vw}{r}\frac{\partial v}{\partial z} + w^2\frac{\partial^2 u}{\partial z^2} + \frac{v^2}{r}\frac{\partial u}{\partial r}\right) = \nu\left(\frac{\partial^2 u}{\partial z^2}\right) - \frac{\sigma B(t)^2}{\rho}\left(u + \lambda_1\left(\frac{\partial u}{\partial t} + w\frac{\partial u}{\partial z}\right)\right), \tag{7.2}$$

$$\frac{\partial v}{\partial t} + u\frac{\partial v}{\partial r} + w\frac{\partial v}{\partial z} + \frac{uv}{r} + \lambda_1\left(\frac{\partial^2 v}{\partial t^2} + 2u\frac{\partial^2 v}{\partial r\partial t} + 2\frac{v}{r}\frac{\partial u}{\partial t} + 2w\frac{\partial^2 v}{\partial z\partial t} + u^2\frac{\partial^2 v}{\partial r^2} - \frac{2u^2 v}{r^2} + \frac{2uv}{r}\frac{\partial u}{\partial r}\right.$$

$$\left. +2uw\frac{\partial^2 v}{\partial r\partial z} - \frac{v^3}{r^2} + \frac{2vw}{r}\frac{\partial u}{\partial z} + \frac{v^2}{r}\frac{\partial v}{\partial r} + w^2\frac{\partial^2 v}{\partial z^2}\right) = \nu\left(\frac{\partial^2 v}{\partial z^2}\right) - \frac{\sigma B(t)^2}{\rho}\left(v + \lambda_1\left(\frac{\partial v}{\partial t} + w\frac{\partial v}{\partial z}\right)\right), \tag{7.3}$$

$$\frac{\partial T}{\partial t} + u\frac{\partial T}{\partial r} + w\frac{\partial T}{\partial z} = \alpha\frac{\partial^2 T}{\partial z^2} + \tau^*\left[D_B\frac{\partial T}{\partial z}\frac{\partial C}{\partial z} + \frac{D_T}{T_0}\left(\frac{\partial T}{\partial z}\right)^2\right]$$

$$+\frac{\sigma B(t)^2}{\rho}\left(u^2 + v^2\right) + \frac{16\sigma^*}{3\rho c_p k^*}\frac{\partial}{\partial z}\left(T^3\frac{\partial T}{\partial z}\right). \tag{7.4}$$

$$\frac{\partial C}{\partial t} + u\frac{\partial C}{\partial r} + w\frac{\partial C}{\partial z} = D_B\frac{\partial^2 C}{\partial z^2} + \frac{D_T}{T_0}\frac{\partial^2 T}{\partial z^2} - k_r^2\left(C - C_0\right)\left(\frac{T}{T_0}\right)^n\exp\left(-\frac{E_a}{k_1 T}\right), \tag{7.5}$$

where E_a is the activation energy and k_r the reaction rate. Expressing the conditions

$$(u, v, w, T, C) = \left(\frac{cr}{1 - \zeta t}, \frac{r\Omega}{1 - \zeta t}, \ 0, \ T_s, \ C_s \right) \text{ at } z = 0,$$

$$w = \frac{\partial h_1}{\partial t} + u\frac{\partial h_1}{\partial r}, \ \frac{\partial u}{\partial z} = \frac{\partial v}{\partial z} = 0, \ \frac{\partial T}{\partial z} = \frac{\partial C}{\partial z} = 0 \text{ at } z = h_1. \tag{7.6}$$

Substituting the transformations (Eq. (6.9) Cf. Chapter **6**) into Eqs. $(7.1) - (7.5)$, and (7.6), we have

$$f''' - S\left(f' + \frac{\eta}{2}f'' \right) - \left(f'^2 - g^2 - 2ff'' \right) - \beta_1 \left(S^2 \left(2f' + \frac{7}{4}\eta f'' + \frac{1}{4}\eta^2 f''' \right) \right. +$$

$$S\left(2f'^2 - 2g^2 - 6ff'' \right) + \eta S\left(f'f'' - gg' - 2ff''' \right) - 4ff'f'' + 4f^2 f''' - 4fgg' \right)$$

$$-M\left(f' + \beta_1 \left(Sf' + \frac{1}{2}\eta Sf'' - 2ff'' \right) \right) = 0, \tag{7.7}$$

$$g'' - S\left(g + \frac{\eta}{2}g' \right) - 2\left(f'g - fg' \right) - \beta_1 \left(S^2 \left(2g + \frac{7}{4}\eta g' + \frac{1}{4}\eta^2 g'' \right) \right. +$$

$$S\left(4f'g - 6fg' \right) + \eta S\left(f'g' + f''g - 2fg'' \right) - 4ff'g' - 4ff''g + 4f^2 g'' \right)$$

$$-M\left(g + \beta_1 \left(Sg + \frac{1}{2}S\eta g' - 2fg' \right) \right) = 0, \tag{7.8}$$

$$\left(1 + \frac{4}{3}Rd \right)\theta'' + \frac{4}{3}Rd \left[(\theta_w - 1)^3 \left(3\theta^2 \theta'^2 + \theta^3 \theta'' \right) + 3\left(\theta_w - 1 \right)^2 \left(2\theta\theta'^2 + \theta^2 \theta'' \right) \right.$$

$$\left. +3\left(\theta_w - 1 \right)\left(\theta'^2 + \theta\theta'' \right) \right] + 2\Pr\left(f\theta' - f'\theta \right) - \frac{1}{2}\Pr S\left(\eta\theta' + 3\theta \right)$$

$$+\Pr\left(Nt \ \theta'^2 + Nb\theta'\phi' \right) + \Pr MEc\left(f'^2 + g^2 \right) = 0, \tag{7.9}$$

$$\phi'' - \frac{1}{2}Sc\left(3\phi + \eta\phi' \right)S + 2Sc\left(f\phi' - f'\phi \right) + \frac{Nt}{Nb}\theta'' - Sc\gamma\left(1 + \delta_3\theta \right)^n \phi \exp\left(-\frac{E}{1 + \delta\theta} \right) = 0, \tag{7.10}$$

with conditions

$$f'(0) = \omega, \ G(0) = 1, \ f(0) = 0, \ \theta(0) = 1, \ \phi(0) = 1,$$

$$f(\beta) = \frac{S\beta}{4}, \ g'(\beta) = 0, \ f''(\beta) = 0, \ \theta'(\beta) = 0, \ \phi'(\beta) = 0. \tag{7.11}$$

In the above equations, the dimensionless parameters S, M, β_1, $\Pr$, θ_w, Ec, Rd, Nt, Nb, Sc, ω, γ, δ_3 and E are the measure of unsteadiness, magnetic parameter, Deborah number, Prandtl

94

number, temperature ratio parameter, Eckert number, radiation parameter, thermophoresis parameter, Brownian motion parameter, Schmidt number, rotation parameter, reaction rate, temperature difference parameter and activation energy parameter. In dimensionless forms, we can write these parameters as

$$S = \frac{a}{\Omega}, \ M = \frac{\sigma B_0^2}{\rho \Omega}, \ \beta_1 = \frac{\lambda_1 \Omega}{1 - \zeta t}, \ \text{Pr} = \frac{v}{\alpha}, \ \theta_w = \frac{Ts}{T_0},$$

$$Ec = \frac{v^2}{c_p (T_s - T_0)}, \ Rd = \frac{4\sigma^* T_0^3}{kk^*}, Nt = \frac{\tau^* D_T (T_0 - T_s)}{T_0 v}, \ Nb = \frac{\tau^* D_B (C_0 - C_s)}{v},$$

$$Sc = \frac{\nu}{D_B}, \ \omega = \frac{c}{\Omega}, \ \gamma = \frac{k_r^2 (1 - \zeta t)}{\Omega}, \ \delta_3 = \frac{(T_s - T_0)}{T_0}, E = \frac{E_a}{k_1 T_0}. \tag{7.12}$$

Further, β denotes the value of the similarity variable η at the free surface and can be written (Eq. (6.9) Cf. Chapter **6**)

$$\beta = \sqrt{\frac{\nu}{\Omega (1 - \zeta t)}} h_1. \tag{7.13}$$

The Nusselt number Nu_r and Sherwood number Sh_r are defined as

$$Nu_r = \frac{R q_w}{k (T_s - T_0)}, Sh_r = \frac{R \ j_w}{k (C_s - C_0)}, \tag{7.14}$$

where

$$q_w = -k \left[1 + \frac{16\sigma^* T^3}{3kk^*}\right] \left(\frac{\partial T}{\partial z}\right) |_{z=0}, \ j_w = -k \left(\frac{\partial C}{\partial z}\right) |_{z=0}, \tag{7.15}$$

and dimensionless expressions of these quantities are

$$Re^{-1/2} \ Nu_r = -\left(1 + \frac{4}{3} Rd \{1 + (\theta_w - 1) \theta(0)\}^3\right) \theta'(0), \tag{7.16}$$

$$Re^{-1/2} \ Sh_r = -\phi'(0), \tag{7.17}$$

where Re is the Reynolds number defined in Chapter **6**.

7.2   Solution Approach

The dimensionless nonlinear momentum, temperature and concentration Eqs $(7.8 - 7.11)$ with conditions (7.12) are considered for the numerical computations. However, the numerical scheme bvp4c is followed to characterize the flow, temperature and concentration profiles in the form of graphs. The bvp4c is one of the collacation method which uses Lobatto IIIA formula. In order to approximate solution of Eqs. $(7.8 - 7.11)$ together with conditions (7.12), it will need the initial guesses which satisfy the boundary conditions. To implement this numerical builtin method the higher order system of ODEs are converted into a system of first ODEs by introducing some new variables. The steps for the conversion are given below. Let

$$f = z_1, \ f' = z_2, \ f'' = z_3, \ g = z_4, \ g' = z_5, \ \theta = z_6, \ \theta' = z_7, \ \phi = z_8, \ \phi' = z_9 \tag{7.18}$$

$$z_1' = z_2, \ z_2' = z_3, \tag{7.19}$$

$$z_3' = \frac{S\left(z_2 + \frac{\eta}{2}z_3\right) + z_2^2 - z_4^2 - 2z_1z_3 + M\left(z_2 + \beta_1\left(Sz_2 + \frac{\eta}{2}Sz_3 - 2z_1z_3\right)\right)}{\left(1 - 4\beta_1 S^2 \frac{\eta^2}{4} + 2\beta_1 S\eta z_1 - 4\beta_1 z_1^2\right)}$$

$$+ \frac{\beta_1\left[S^2\left(2z_2 + \frac{7}{4}\eta z_3\right) + S\left(2z_2^2 - 2z_4^2 - 6z_1z_3\right) + S\eta\left(z_2z_3 - z_4z_5\right) - 4z_1z_2z_3 - 4z_1z_4z_5\right]}{\left(1 - 4\beta_1 S^2 \frac{\eta^2}{4} + 2\beta_1 S\eta z_1 - 4\beta_1 z_1^2\right)} \tag{7.20}$$

$$z_4' = z_5, \tag{7.21}$$

$$z_5' = \frac{S\left(z_4 + \frac{\eta}{2}z_5\right) - 2z_1z_5 + 2z_2z_4 + M\left(z_4 + \beta_1\left(Sz_4 + \frac{\eta}{2}Sz_5 - 2z_1z_5\right)\right)}{\left(1 - 4\beta_1 S^2 \frac{\eta^2}{4} + 2\beta_1 S\eta z_1 - 4\beta_1 z_1^2\right)}$$

$$+ \frac{\beta_1\left[S^2\left(2z_4 + \frac{7}{4}\eta z_5\right) + S\left(4z_2z_4 - 6z_1z_5\right) + S\eta\left(z_2z_5 + z_3z_4\right) - 4z_1z_2z_5 - 4z_1z_3z_4\right]}{\left(1 - 4\beta_1 S^2 \frac{\eta^2}{4} + 2\beta_1 S\eta z_1 - 4\beta_1 z_1^2\right)} \tag{7.22}$$

$$z_6' = z_7, \tag{7.23}$$

$$z_7' = \frac{-\frac{4}{3}Rd\left[3\left(\theta_w - 1\right)^3 z_6^2 z_7^2 + 6\left(\theta_w - 1\right)^2 z_6 z_7^2 + 3\left(\theta_w - 1\right) z_7^2\right] - 2\Pr\left(z_1z_7 - z_2z_6\right)}{1 + \frac{4}{3}Rd\left(1 + \left(\theta_w - 1\right)^3 z_6^3 + 3\left(\theta_w - 1\right)^2 z_6^2 + 3\left(\theta_w - 1\right) z_6\right)}$$

$$+\frac{\frac{1}{2}\Pr S\left(\eta z_7 + 3z_6\right) - \Pr\left(Nbz_7z_9 + Ntz_7^2\right) - \Pr MEc\left(F'^2 + z_4^2\right)}{1 + \frac{4}{3}Rd\left(1 + (\theta_w - 1)^3 z_6^3 + 3\left(\theta_w - 1\right)^2 z_6^2 + 3\left(\theta_w - 1\right)z_6\right)},\tag{7.24}$$

$$z_8' = z_9,\tag{7.25}$$

$$z_9' = \frac{1}{2}Sc\left(3z_8 + \eta z_9\right)S + 2Sc\left(z_2z_8 - z_1z_9\right) - \frac{Nt}{Nb}z_7' + Sc\gamma\left(1 + \delta_3\theta\right)^n \phi e^{-\frac{E}{1+\delta_3\theta}},\tag{7.26}$$

with conditions

$$z_1(0) = 0, \;\; z_2(0) = \omega, \;\; z_4(0) = 1, \;\; z_6(0) = 1, \;\; z_8(0) = 1,$$

$$z_1(\beta) = \frac{S}{4}\beta, \;\; z_3(\beta) = 0, \;\; z_5(\beta) = 0, \;\; z_7(\beta) = 0, \;\; z_9(\beta) = 0.\tag{7.28}$$

Here in total ten boundary conditions are reduced into nine by finding the relationship between film thickness β and unsteadiness parameter S. This relationship can be obtained by solving first Eqs. (7.19) to (7.28) and the initial guess for the film thickness β is provided to the bvp4c numerical scheme. The value of guess for β is settled in such a manner so that the condition $Z_1(\beta) = \frac{S}{4}\beta$ holds. This procedure is based on trial and error basis. Then, Eqs. (7.19) to (7.28) are solved numerically with bvp4c method for known estimation of β and S.

7.3   Results and Discussion

The current work focuses on the transient heat and mass transfer properties in liquid thin film flow over a horizontal rotating disk with the impact of magnetic field, nonlinear thermal radiation, Joule heating, and Arrhenius chemical reaction with activation energy. Numerical computations have been accomplished with numerous estimation of emerging quantities in appropriate ranges like unsteadiness parameter S $(1.0 - 1.9)$, magnetic field parameter M $(1.0 - 2.5)$, rotation parameter ω $(1.0 - 1.6)$, Deborah number β_1 $(0.0 - 0.2)$, Prandtl number Pr $(1.0 - 2.5)$, temperature ratio parameter θ_w $(1.3 - 2.2)$, radiation parameter Rd $(1.0 - 2.2)$, Eckert number Ec $(0.0 - 1.5)$, thermophoresis parameter Nt $(0.5 - 2.0)$, Brownian motion parameter Nb $(0.4 - 1.2)$, reaction rate parameter γ $(0.0 - 3.0)$, temperature difference parameter δ $(0.0 - 3.0)$, activation energy parameter E $(0.0 - 1.5)$, and fitted rate constant n $(0.0 - 3.0)$. The obtained

numerical results are plotted through **Figs. 7.1(a-d)** to **7.12(a,b)**.

Figs. **7.1(a-c)** describe the consequences of unsteadiness parameter S on the velocity components represented by $f'(\eta)$, $g(\eta)$, and $f(\eta)$ in radial, axial and azimuthal directions, respectively. A significant increase is noted with the intensifying variation in the unsteadiness parameter S. These figures also exhibit that an increasing unsteadiness parameter S $(1.0 - 1.9)$ results in a reduction the film thickness β from 2.213683 to 1.094566. **Fig. 7.1(d)** illustrates the temperature field $\theta(\eta)$ with the growing values of unsteadiness parameter. It is observed from these curves that the fluid temperature increases with the unsteadiness parameter at the expense of reduction in the non-dimensional film thickness of nanofluid. The fluid velocity and frictional forces enhance due to an increase in the unsteady stretching rate of the disk. The area of the surface stretching inclines, and the heat produced as a result of frictional forces on the surface is shifted towards the flow as soon as the frictional forces increase, causing the reduction in heat-flux. The fundamental parameter of the physical problem specified by the rotation parameter ω affect the thermal and flow fields which is sketched in **Figs. 7.2(a-d)**. **Fig. 7.2(a)** depicts that the radial flow augmented with boosting the rotation parameter. Actually, when the rotation is enhanced, the centrifugal force develops forceful exerting pressure on the particles of fluid to travel in the radial direction. By moving away from the disk surface, a decreasing trend is seen in radial velocity component due to the reason that the impact of centrifugal force is influenced at disk nearby area. Also in view of this argument, the azimuthal velocity component also increases with increasing rotation as observed in **Fig. 7.2(c)**. A diminishing movement is shown by the axial velocity with ω. As the ω increases, the effect of centrifugal force becomes stronger. The impact of this force is to push the fluid particles in radial direction which are balanced by the particles move in the negative axial direction towards the wall due to wall stretching. **Fig. 7.2(d)** portrays that without Joule heating and dissipation, the fluid temperature drops down with growing rotation rate which leads to heat loss.

The parameter M properties on the velocities and thermal fields are demonstrated in **Figs. 7.3(a-d)**. We observe a noteworthy reduction in flow curves in $r-$, $\varphi-$ and $z-$directions as shown in **Figs. 7.3(a-c)**. The fluid temperature is seen in an increasing manner which is displayed in **Fig. 7.3(d)**. It is also prominent that these graphs that the film thickness β decreases with the magnetic field parameter M. The motion of electrically conducting fluid

faces an opposing force in response to magnetic field. Due to an increment in M, inertial force is dominated by the Lorentz force. This force is generated as an outcome of the transverse magnetic field and overcomes convection. Ultimately, minimizing the heat transfer rate. The effect of Deborah number β_1, which is associated with the fluid relaxation time characteristics, on vertical, radial, circumferential and thermal fields is depicted in **Figs. 7.4(a-d)**. By fixing the values of other parameters, fluid motion is revealed as a diminishing function of β_1 while an enhancement occurs in the temperature field. The value $\beta_1 = 0$ corresponds to the viscous fluid model while the curves for $\beta_1 \neq 0$ are shown for the Maxwell fluid model. The Deborah number is the ratio of fluid relaxation time to observation time. The lesser values of Deborah number correspond to the smaller recovery interval and the material behave like a purely viscous fluid. On the other hand, material depicts a solid like response for the larger value of Deborah number. Thus, an enhancement in Deborah number leads to increase the Deborah number and therefore the fluid velocity decreases. Consequently, the field $\theta(\eta)$ upsurges with the β_1 as depicted in **Fig. 7.4(d)**. It is also perceived that the liquid thickness β reduces with higher rating of β_1. Further, the nano liquid film thickness decreases from 2.4565061 to 2.033285 as the Deborah number increases from 0.0 to 2.0.

The temperature field $\theta(\eta)$ variation with Eckert number Ec is shown in **Fig. 7.5(a)**. It is remarked that the $\theta(\eta)$ upsurges with the enhancement of Ec. When Ec is augmented from 0.0 to 1.5 then due to molecules internal friction the fluid mechanical energy is transformed to thermal energy. Therefore the fluid temperature increases. The Prandtl number Pr impact on temperature field is described in **Fig**. **7.5(b)**. A significant decline in fluid temperature occurs with higher value of Prandtl number. Physically, Prandtl number has an inverse relation with thermal diffusivity. Therefore, the fluid having higher Pr slowly diffuses as compared to fluid having lower values of Pr. This argument results in a reduction in the fluid temperature within the thin film flow.

Fig. 7.6(a) shows the characteristics of radiation parameter Rd on temperature field $\theta(\eta)$. It is obvious from the curves that with the rising values of Rd, a significant development happens in fluid temperature. This observation is seen for linear as well as for nonlinear thermal radiations. Physically, more heat is provided to the liquid by flourishing the thermal radiation effects which as a result upsurges $\theta(\eta)$. The role of temperature ratio parameter θ_w on $\theta(\eta)$ is visualized in

Fig. 7.6(b). The value $\theta_w = 1$ corresponds to linear thermal radiation phenomenon. The temperature field is directly proportional to the temperature ratio parameter θ_w. It is due to the reason that improving temperature ratio parameter, the wall temperature value is superior than the ambient temperature.

The impact of nanofluid parameters Nt and Nb on $\theta(\eta)$ is elucidated in **Figs. 7.7(a,b)**. As shown by these plots, the temperature field magnifies and the film thickness β decreases with rising values of Nt and Nb. Physically, the Brownian motion signify the disorderly motion of the fluid particles and the increase in Brownian motion indicates the improvement in particles disorder motion which formed much heat. The temperature profile rise with increasing thermophoretic effects. The force that diffuses nanoparticles into the ambient fluid due to temperature gradient is known as thermophoresis force. The role of thermophoretic force is such that the nanoparticles near the hot boundary are being pushed towards the cold fluid at the ambient.

Figs. 7.8(a,b) represent the isotherms with variations in Eckert number $Ec = 0.5$ and $Ec = 1.5$, respectively, when $T_0 = 0.1$. By moving in the radial and azimuthal directions, the temperature values increase in both cases. The same behavior is depicted in **Figs. 7.8(c,d)** for the $Ec = 0.5$ and $Ec = 1.5$, respectively, when $T_0 = 0.0$. However, the difference between the Figs. **7.8(a,b)** and **Figs. 7.8(c,d)** is that hotter region is little bit greater in the case when $T_0 = 0.1$. Further, on the surface of the disk when $z = 0$, the temperature value 0.3 is achieved around the radial distance $r = 0.8$ in the case $T_0 = 0.1$ while in case of $T_0 = 0.0$ it is achieved at $r = 1.0$. The behavior of thermophoresis parameter $Nt = 0.0$ and $Nt = 0.6$ on the isotherms is graphed in **Figs. 7.9(a,b)** when $T_0 = 0.0$. Here temperature increases in the increasing $r-$ and $z-$ directions. Also, we observe that moving along the disk surface, value of temperature 0.3 is achieved at the radial distance after $r = 0.8$ in case of $Nt = 0.0$ while it is meet before $r = 0.8$ in case of $Nt = 0.6$.

In **Figs. 7.10(a)**, it is revealed that the nanoparticles volume fraction $\phi(\eta)$ shows a decreasing behavior with the increasing value of Brownian motion parameter Nb. The thermophoresis parameter Nt action on nanoparticles concentration is explained in **Fig. 7.10(b)**. The cumulative action of thermophoresis parameter has been shown an increasing trend in nanoparticles fluid concentration. This is because of the thermophoresis larger impact act to transport the

nanoparticles near to the hot disk on the way to cold fluid at the ambient and hence larger penetration depth is delivered. **Figs. 7.11(a,b)** are sketched to show the influence of reaction rate γ and fitted rate n constant on solutal concentration $\phi(\eta)$. It can be detected that an enhancement in either reaction rate or fitted rate constant implies an increment in the factor $Sc\gamma\left(1+\delta_3\theta\right)^n\phi\exp\left(-\frac{E}{1+\delta_3\theta}\right)$. This ultimately favors the destructive chemical reaction and thus rises the concentration field $\phi(\eta)$. The non-dimensional activation energy parameter E as a function of concentration profile $\phi(\eta)$ has been plotted in **Fig. 7.12(a)**. The patterns of the curves indicate the thickening of the boundary layer for concentration with developing value of E. This occurs because the high activation energy and low temperature results in a smaller rate constant and thus decelerate the chemical reaction which boosts the nanoliquid concentration. The temperature difference parameter δ_3 impact on concentration field is shown in **Fig. 7.12(b)**. A decreasing trend in solute concentration is noted with the variation in temperature difference parameter. This indicates that when the wall and ambient temperature difference enlarges, the $\phi(\eta)$ increases.

The fluctuation of β against the parameters S, M, β_1 and ω is computed in **table 7.1**. It can be observed that the effect of S, M and β_1 is to reduce the nanofluid film thickness whereas it is raised with the increasing impact of ω. **Table 7.2** is organized to see the impact of parameters S, β_1, M, ω, θ_w, Rd, Ec and Nt on heat transfer rate $Re^{-1/2}Nu_r$ at the surface of disk. It is revealed from this table that $Re^{-1/2}Nu_r$ intensified with S, ω, θ_w, and Rd whereas it decreases with β_1, M, Ec and Nt. The rate of mass transfer $Re^{-1/2}Sh_r$ against the parameters Nt, Nb, Sc, E, γ and δ_3 is shown in **table 7.3**. The mass transfer rate for the parameters Nb, Sc, γ, and δ_3 have the increasing tendency while the conflicting trend is observed for parameters Nt and E.

Table 7.1: Variations of film thickness β against several of S, M and β_1 when $\omega = 1.0$.

S	β_1	M	ω	β
1.3	0.1	1.0	1.0	1.681955
1.6				1.335091
1.9				1.086706
1.3	0.0			1.879473
	0.1			1.681955
	0.2			1.532196
	0.1	1.0		1.681955
		1.5		1.551951
		2.0		1.448023
		1.0	1.0	1.681955
			1.3	1.961108
			1.6	2.197069

Table 7.2: The Nusselt number $Nu_r Re^{-1/2}$ values when $\mathrm{Pr} = 1.7$, $Sc = 2.0$, $n = 2.0$, $E = 1.0$, $\gamma = 1.0$ and $\delta_3 = 1.0$.

S	β_1	M	ω	θ_w	Rd	Ec	Nt	Nb	$Nu_r Re^{-1/2}$
1.3	0.1	1.0	1.0	1.5	1.0	1.0	0.5	0.5	3.423540
1.6									3.612822
1.9									3.740212
1.3	0.0								3.487298
	0.1								3.423540
	0.2								3.352658
	0.1	1.0							3.423540
		1.5							3.054844
		2.0							2.706676
		1.0	1.0						3.423540
			1.2						3.547793
			1.4						3.629120
			1.0	1.3					2.936015
				1.6					3.667414
				1.9					4.359568
				1.5	0.5				2.558688
					1.5				4.009196
					2.5				4.730688
					1.0	0.5			3.739274
						1.0			3.42354
						1.5			3.106948
						1.0	0.6		3.398035
							1.2		3.254594
							1.8		3.125744

Table 7.3: The Sherwood number $Sh_r Re^{-1/2}$ values when $S = 1.3$, $\beta_1 = 0.1$, $M = 1.0$, $\mathrm{Pr} = 1.7$, $\omega = 1.0$, $\theta_w = 1.5$, $Rd = 1.0$, $Ec = 1.0$ and $n = 2.0$.

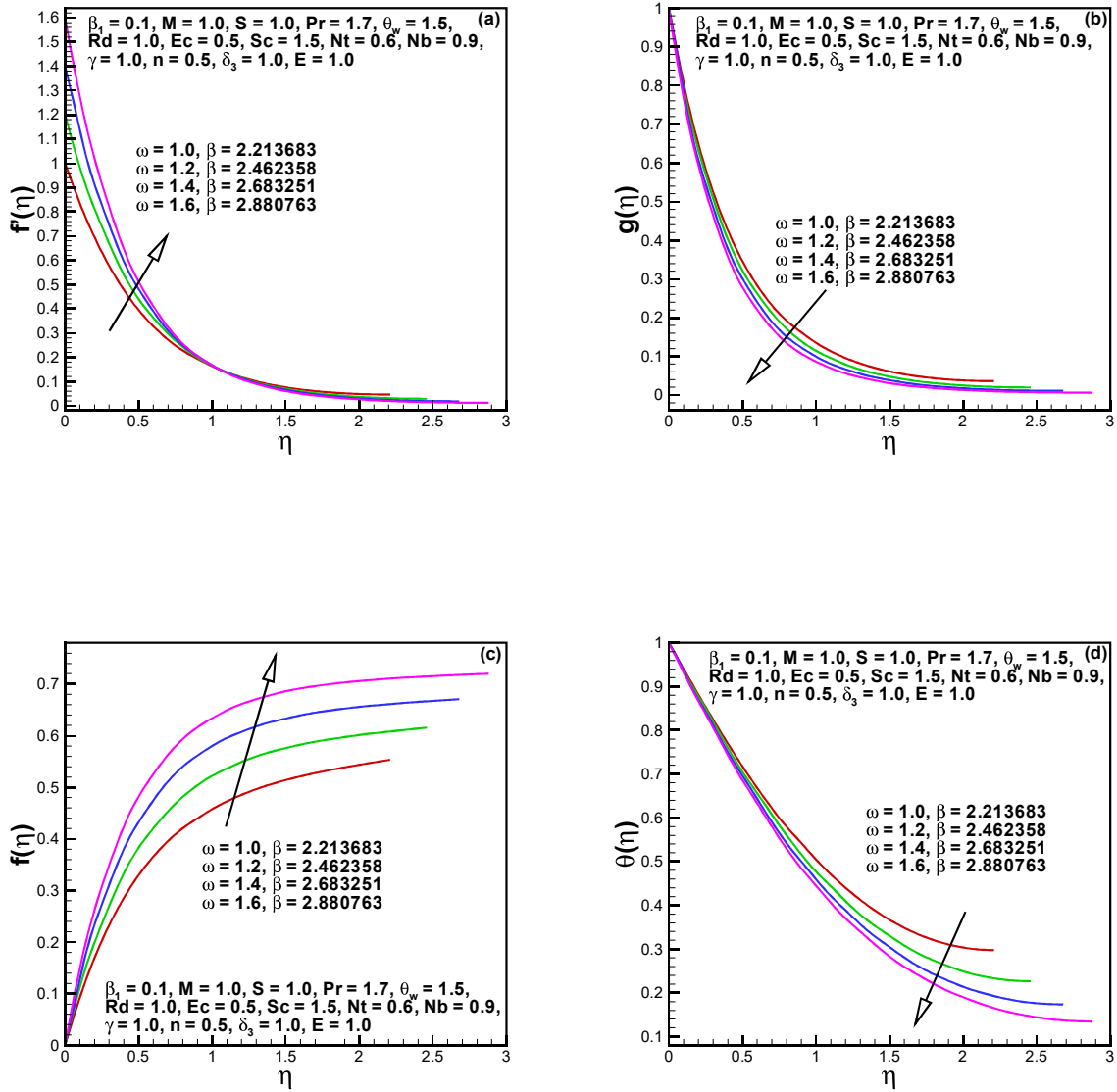| Nt	Nb	Sc	E	ω	δ_3	$Sh_r Re^{-1/2}$
0.6	0.5	2.0	1.0	1.0	1.0	3.408211
1.2						3.336393
1.8						3.280286
0.6	0.4					3.372096
	0.8					3.462955
	1.2					3.494176
	0.5	1.5				2.874149
		2.5				3.872146
		3.5				4.668066
		2.0	0.0			3.860343
			1.0			3.408211
			2.0			3.106957
			1.0	0.0		2.617261
				1.0		3.408211
				2.0		4.048394
				1.0	0.0	2.776979
					1.0	3.408211
					2.0	4.382524
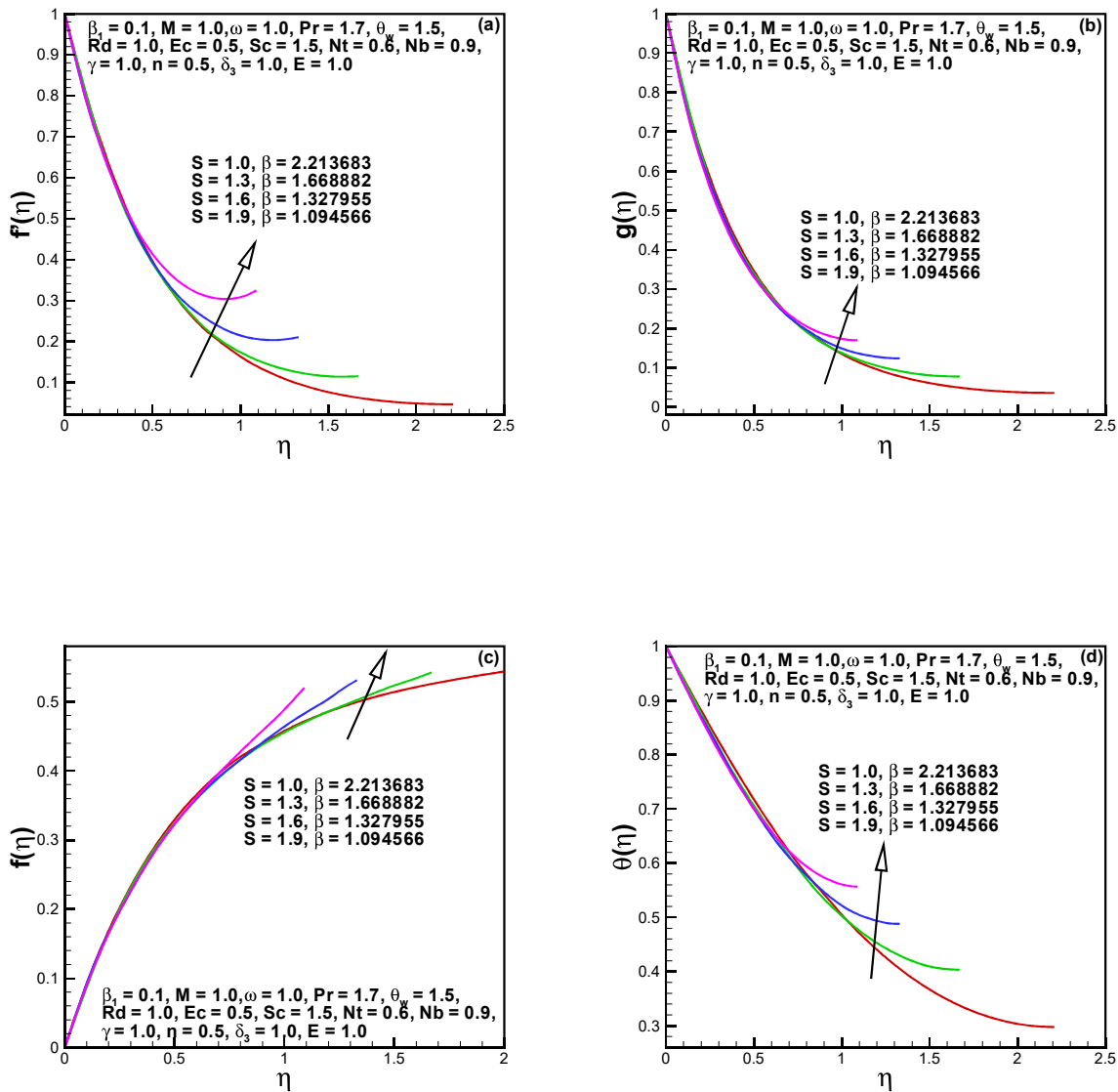
Fig. 7.1: f', g, f and θ for S.

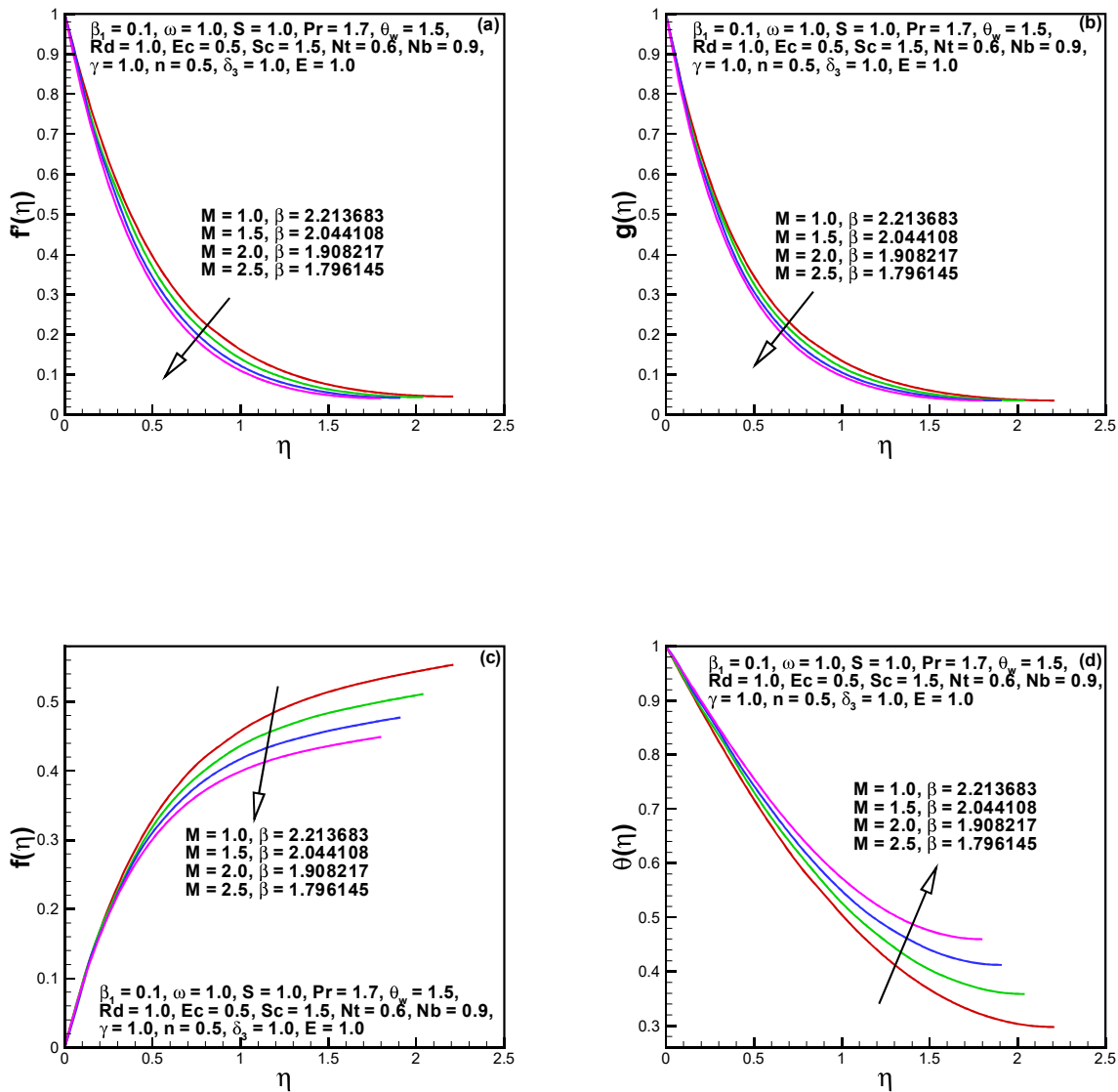**Fig. 7.2:** f', g, f and θ for ω.

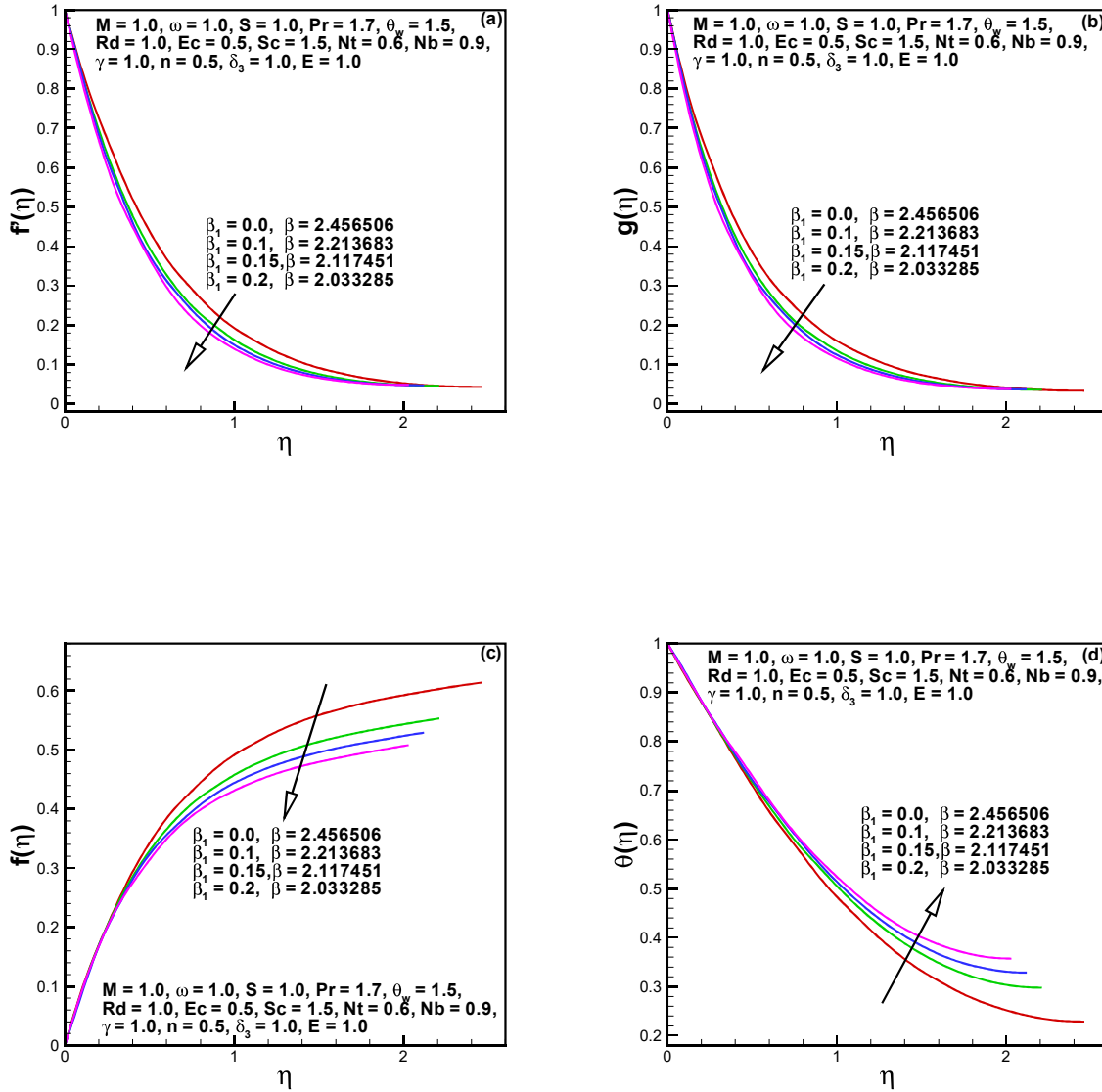**Fig. 7.3:** f', g, f and θ for M.
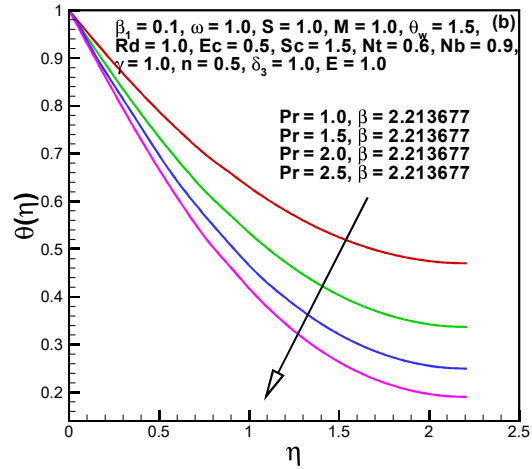
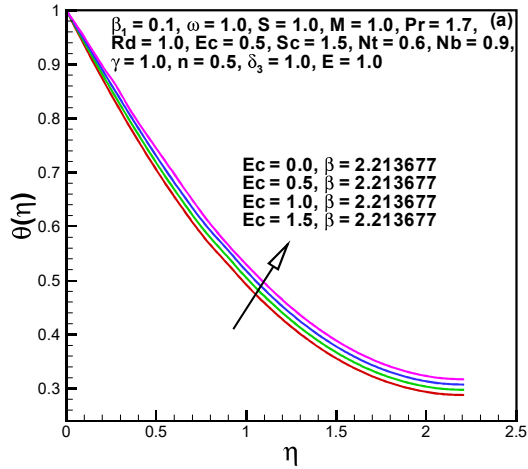**Fig. 7.4:** f', g, f and θ for β_1.

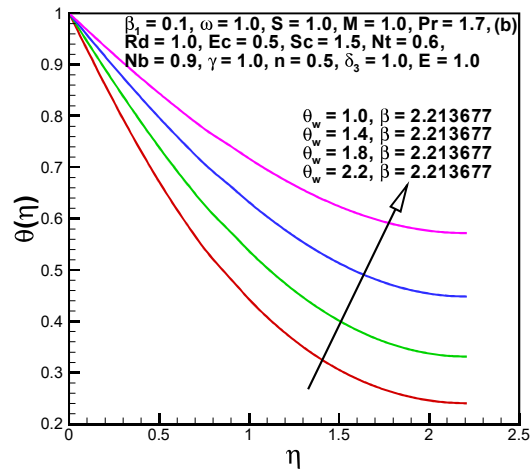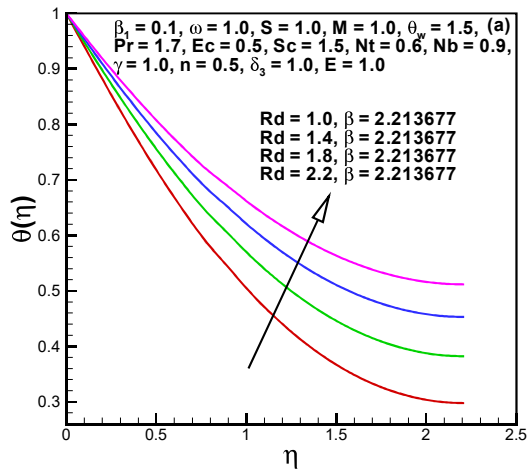**Fig. 7.5:** θ for Ec and Pr.

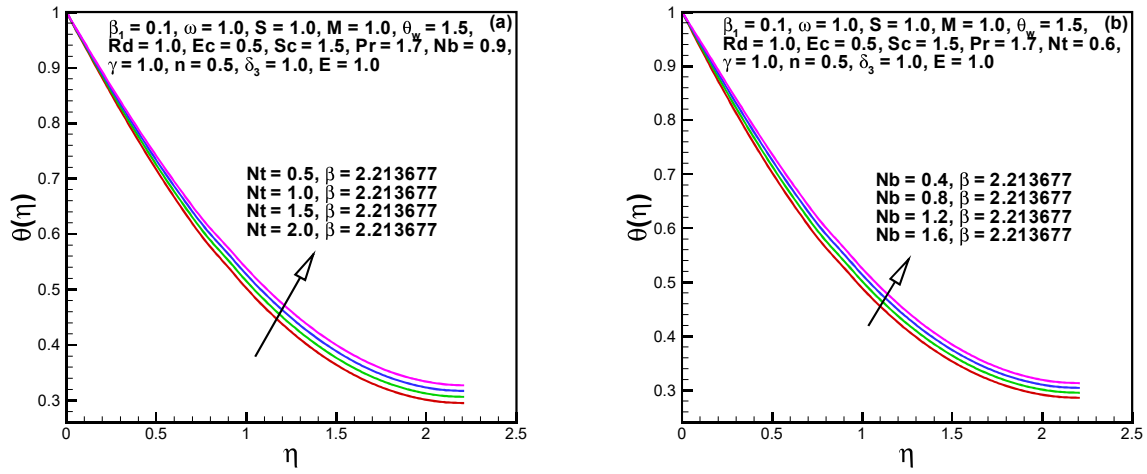**Fig. 7.6:** θ for Rd and θ_w.

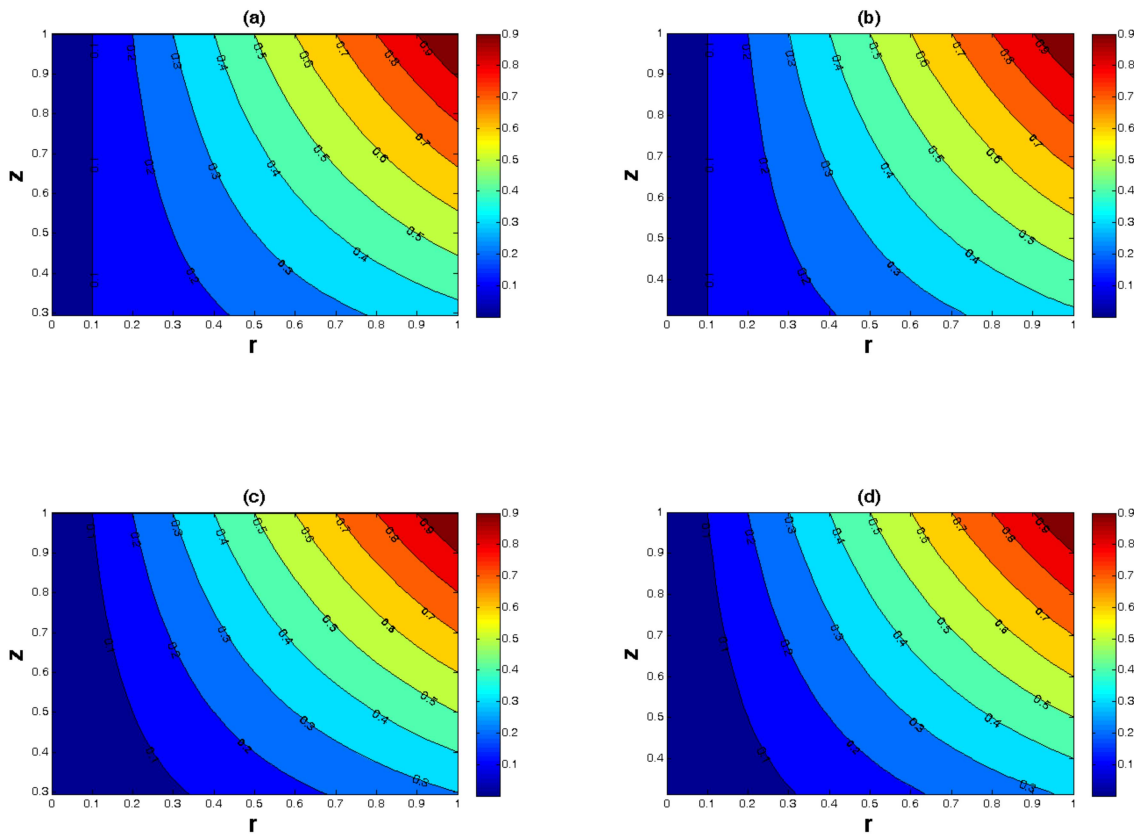**Fig. 7.7:** θ for Nt and Nb.

Fig. 7.8: Isotherms for Ec when (a,b) $T_0 = 0.1$ and (c,d) $T_0 = 0.0$.
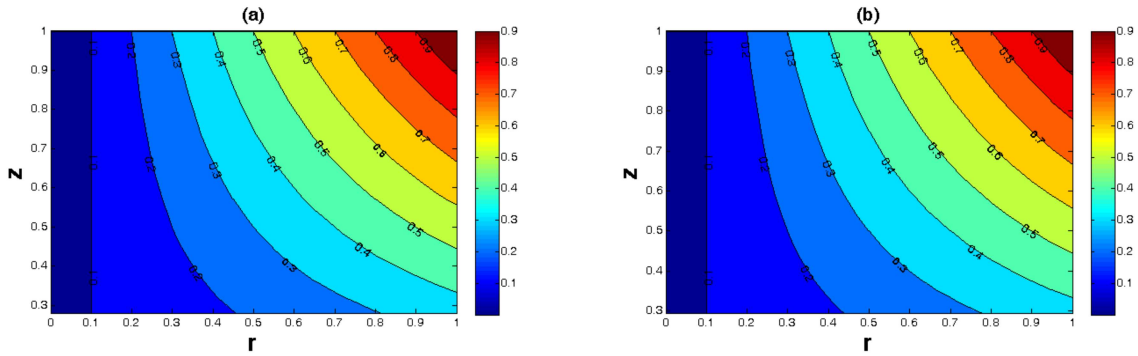
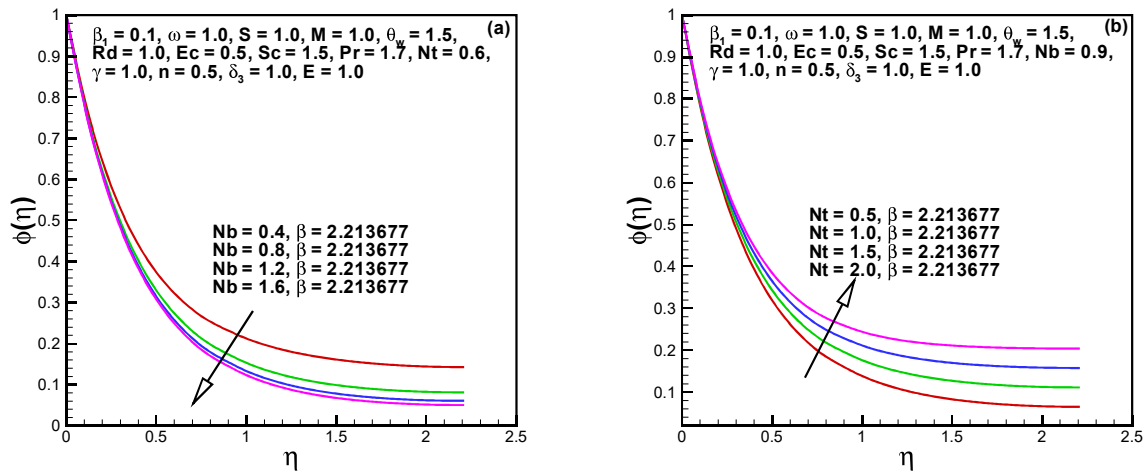**Fig. 7.9:** Isotherms for Nt when $T_0 = 0.1$.
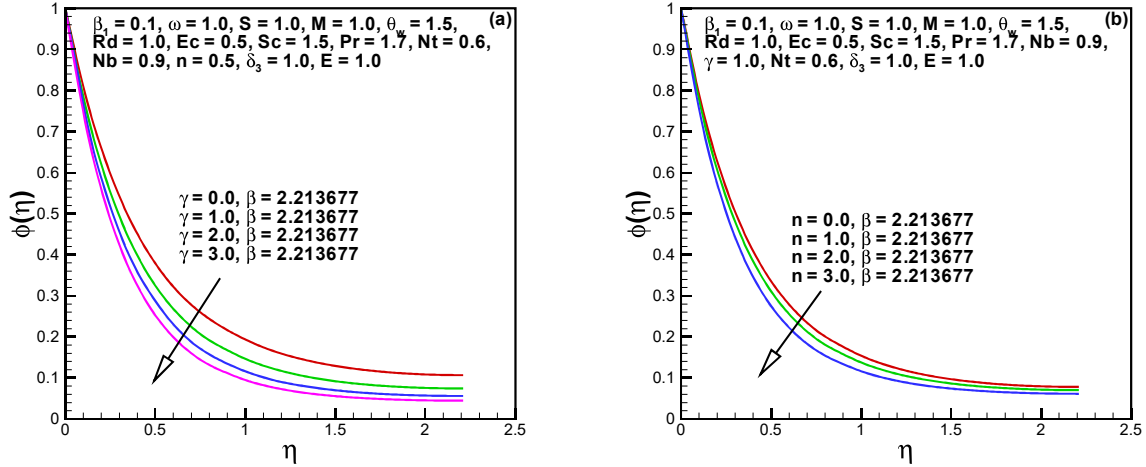

Fig. 7.10: ϕ for Nb and Nt.

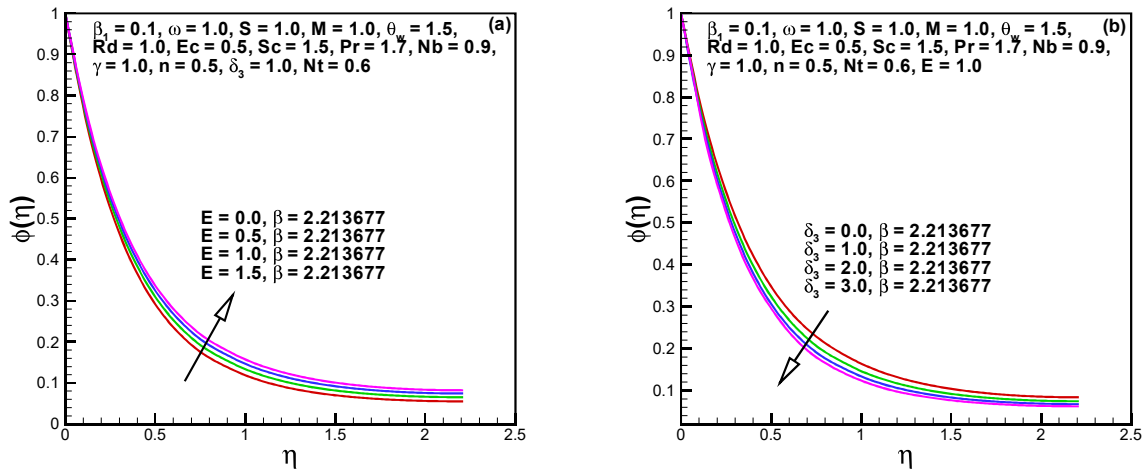**Fig. 7.11:** ϕ for γ and n.

Fig. 7.12: ϕ for E and δ_3.

112

Chapter 8

Flow of Maxwell Nanofluid Between Two Coaxially Rotating Disks with Variable Thermal Conductivity

The main concern of this chapter is to study the Maxwell nanofluid flow between two coaxially parallel stretchable rotating disks subject to axial magnetic field. The heat transfer process is studied with the characteristics of temperature dependent thermal conductivity. The upper and lower disks, rotating with different velocities, are discussed for the case of same as well as opposite directions of rotation. The von Kármán transformations procedure is implemented to obtain the set of nonlinear ODEs involving the momentum, energy and concentration equations. A builtin numerical scheme bvp4c is executed to accomplish the solution of governing nonlinear problem. The graphical and tabular features of the concentration, temperature, velocity and pressure fields are demonstrated against the influential parameters including the thermophoresis parameter, magnetic number, stretching parameters, Deborah number, Reynolds number, Prandtl number and Brownian motion parameter. The significant outcomes reveal that stretching action causes to reverse the flow behavior. It is further noted that the effect of Deborah number is to reduce the velocity and pressure fields. Further, the impact of thermophoresis and thermal conductivity parameters is to increase the temperature profile. Moreover, the fluid concentration is reduced with the stronger action of Schmidt number.
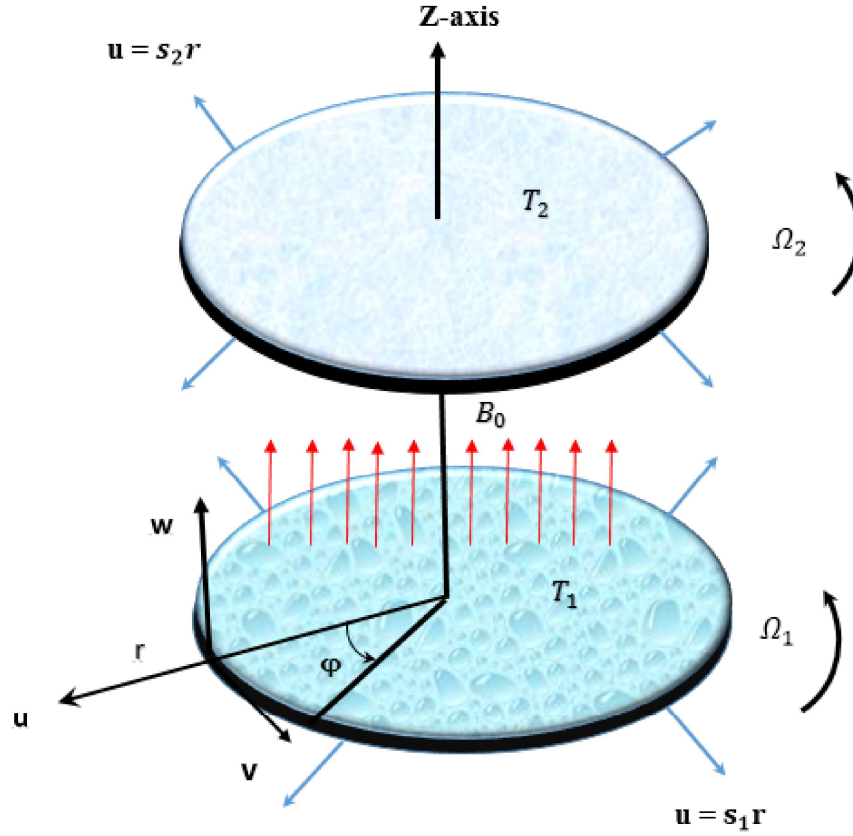
8.1 Flow Configuration

Fig. 8.1: Flow geometry and coordinates system.

8.2 Mathematical Presentation

Consider the steady motion of Maxwell nanofluid between the gap of two stretchable coaxially rotating disks. The lower disk is kept at $z = 0$ while upper disk is positioned at constant distance apart $z = d$. The strength B_0 of magnetic flux is projected in vertical upward direction. The rotating velocity and stretching rate of lower disks are (Ω_1, s_1) while the upper disk is rotating and stretching with (Ω_2, s_2). Let (T_1, T_2) denote the prescribed constant temperature at lower and upper disks, where $T_1 > T_2$. The concentration at the lower and upper disks are represented with (C_1, C_2). The development of mathematical model is assisted with cylindrical coordinated system (r, φ, z) as seen in **Fig. 8.1**.

In components form, the continuity, momentum, energy and concentration equations take

the following forms (Eqs. (1.4), (1.7), (1.15), (1.17) Cf. Chapter **1**)

$$\frac{\partial}{\partial z}(w) + \frac{1}{r}\frac{\partial}{\partial r}(ru) = 0, \tag{8.1}$$

$$u\frac{\partial u}{\partial r} + w\frac{\partial u}{\partial z} - \frac{v^2}{r} = -\frac{1}{\rho}\frac{\partial p}{\partial r} + \nu\left(-\frac{2u}{r^2} + 2\frac{\partial^2 u}{\partial r^2} + \frac{\partial^2 u}{\partial z^2} + \frac{\partial^2 w}{\partial r\partial z} + \frac{2}{r}\frac{\partial u}{\partial r}\right)$$

$$-\lambda_1\left(u^2\frac{\partial^2 u}{\partial r^2} + w^2\frac{\partial^2 u}{\partial z^2} + 2uw\frac{\partial^2 u}{\partial r\partial z} - \frac{2uv}{r}\frac{\partial v}{\partial r} - \frac{2uw}{r}\frac{\partial v}{\partial z} + \frac{uv^2}{r^2} + \frac{v^2}{r}\frac{\partial u}{\partial r}\right)$$

$$-\frac{\sigma B_0^2}{\rho}\left(u + w\lambda_1\frac{\partial u}{\partial z}\right), \tag{8.2}$$

$$u\frac{\partial v}{\partial r} + w\frac{\partial v}{\partial z} + \frac{uv}{r} = \nu\left(\frac{\partial^2 v}{\partial r^2} - \frac{v}{r^2} + \frac{1}{r}\frac{\partial v}{\partial r} + \frac{\partial^2 v}{\partial z^2}\right)$$

$$-\lambda_1\left(u^2\frac{\partial^2 v}{\partial r^2} + w^2\frac{\partial^2 v}{\partial z^2} + 2uw\frac{\partial^2 v}{\partial r\partial z} + \frac{2uv}{r}\frac{\partial u}{\partial r} + \frac{2vw}{r}\frac{\partial u}{\partial z} - \frac{2u^2v}{r^2} - \frac{v^3}{r^2} + \frac{v^2}{r}\frac{\partial v}{\partial r}\right)$$

$$-\frac{\sigma B_0^2}{\rho}\left(v + w\lambda_1\frac{\partial v}{\partial z}\right), \tag{8.3}$$

$$w\frac{\partial w}{\partial z} + u\frac{\partial w}{\partial r} = \nu\left(2\frac{\partial^2 w}{\partial z^2} + \frac{\partial^2 u}{\partial r\partial z} + \frac{\partial^2 w}{\partial r^2} + \frac{1}{r}\frac{\partial u}{\partial z} + \frac{1}{r}\frac{\partial w}{\partial r}\right) - \frac{1}{\rho}\frac{\partial p}{\partial z}$$

$$-\lambda_1\left(u^2\frac{\partial^2 w}{\partial r^2} + 2uw\frac{\partial^2 w}{\partial r\partial z} + w^2\frac{\partial^2 w}{\partial z^2} + \frac{v^2}{r}\frac{\partial w}{\partial r}\right), \tag{8.4}$$

$$(\rho c_p)_f\left(u\frac{\partial T}{\partial r} + w\frac{\partial T}{\partial z}\right) = \frac{k(T)}{r}\frac{\partial T}{\partial r} + \frac{\partial}{\partial r}\left(k(T)\frac{\partial T}{\partial r}\right) + \frac{\partial}{\partial z}\left(k(T)\frac{\partial T}{\partial z}\right) +$$

$$(\rho c_p)_p\left[D_B\left(\frac{\partial T}{\partial z}\frac{\partial C}{\partial z} + \frac{\partial T}{\partial r}\frac{\partial C}{\partial r}\right) + \frac{D_T}{T_2}\left\{\left(\frac{\partial T}{\partial z}\right)^2 + \left(\frac{\partial T}{\partial r}\right)^2\right\}\right], \tag{8.5}$$

$$w\frac{\partial C}{\partial z} + u\frac{\partial C}{\partial r} = D_B\left(\frac{\partial^2 C}{\partial z^2} + \frac{\partial^2 C}{\partial r^2} + \frac{1}{r}\frac{\partial C}{\partial r}\right) + \frac{D_B}{T_2}\left(\frac{\partial^2 T}{\partial z^2} + \frac{\partial^2 T}{\partial r^2} + \frac{1}{r}\frac{\partial T}{\partial r}\right), \tag{8.6}$$

The modeled conditions are

$$(T,\ C,\ u,\ v,\ w) = (T_1,\ C_1,\ s_1 r,\ \Omega_1 r,\ 0)\ \text{at}\ z = 0,$$

$$(T,\ C,\ u,\ v,\ w) = (T_2,\ C_2,\ s_2 r,\ \Omega_2 r,\ 0)\ \text{at}\ z = d. \tag{8.7}$$

The similarity variables are defined as

$$u = \Omega_1 r f'(\eta), \ v = \Omega_1 r g(\eta), \ w = -2h\Omega_1 f(\eta), \ \eta = \frac{z}{d},$$

$$p = \rho \Omega_1 \nu \left(P(\eta) + \frac{1}{2}\frac{r^2}{d^2}\Lambda \right), \ \theta(\eta) = \frac{T - T_2}{T_1 - T_2}, \ \phi(\eta) = \frac{C - C_2}{C_1 - C_2}. \tag{8.8}$$

Adopting the above transformations, we can write the dimensionless form of Eqs. (8.1) to (8.7) as

$$f''' - Re\left(f'^2 - g^2 - 2ff'' \right) + Re\beta_1 \left(4ff'f'' - 4f^2 f''' - 4fgg' \right)$$

$$-MRe\left(f' - 2\beta_1 ff'' \right) + \Lambda = 0, \tag{8.9}$$

$$g'' + 2Re\left(fg' - f'g \right) + Re\beta_1 \left(4ff'g' - 4f^2 g'' + 4ff''g \right) - MRe\left(g - 2\beta_1 fg' \right) = 0, \tag{8.10}$$

$$P' = -2f'' - Re\left(4ff' - 8\beta_1 f^2 f'' \right), \tag{8.11}$$

$$(1 + \varepsilon\theta)\theta'' + 2Re\Pr f\theta' + \varepsilon\theta'^2 + \Pr Nb\theta'\phi' + \Pr Nt\theta'^2 = 0, \tag{8.12}$$

$$\phi'' + 2ReSc f\phi' + \frac{Nt}{Nb}\theta'' = 0, \tag{8.13}$$

with conditions

$$\left(f', \ f, \ g, \ \theta, \ \phi, \ P \right) = (S_1, \ 0, \ 1, \ 1, \ 1, \ 0) \text{ at } \eta = 0,$$

$$\left(f', \ f, \ g, \ \theta, \ \phi \right) = (S_2, \ 0, \ \omega_1, \ 1, \ 1) \text{ at } \eta = 1, \tag{8.14}$$

where Λ is the unknown pressure gradient parameter that has to be determined by the boundary conditions. The dimensionless parameters $\beta_1 = \lambda_1\Omega_1$ is the Deborah number, $S_1 = \frac{s_1}{\Omega_1}$ the stretching parameter of the lower disk, $S_2 = \frac{s_2}{\Omega_2}$ the stretching parameter of the upper disk, $M = \frac{\sigma B_0^2}{\rho\Omega_1}$ the magnetic parameter, $\Pr = \frac{\nu}{\alpha}$ the Prandtl number, $\omega_1 = \frac{\Omega_2}{\Omega1}$ the rotation number, $Nb = \frac{(\rho c_p)_p D_B (C_1 - C_2)}{(\rho c_p)_f \nu}$ the Brownian motion parameter, $Nt = \frac{(\rho c_p)_p D_B (T_1 - T_2)}{(\rho c_p)_f \nu T_2}$ the thermophoresis parameter , $Sc = \frac{\nu}{D_B}$ the Schmidt number and $Re = \frac{\Omega_1 d^2}{\nu}$ the Reynolds number.

8.2.1 Nusselt Number

The heat transfer rate at the lower and upper disks can be defined as

$$Nu_1 = -\frac{h}{k(T_1 - T_2)}\left(\frac{\partial T}{\partial z} \right)\Big|_{z=0}, \ Nu_2 = -\frac{h}{k(T_1 - T_2)}\left(\frac{\partial T}{\partial z} \right)\Big|_{z=d}. \tag{8.15}$$

In dimensionless form, Nusselt numbers can be written as

$$Nu_1 = -\theta'(0), \ Nu_2 = -\theta'(1). \tag{8.16}$$

8.2.2 Sherwood Number

The mass transfer rate at the lower and upper disks can be defined as

$$Sh_1 = -\frac{h}{k(C_1 - C_2)} \left(\frac{\partial C}{\partial z}\right) |_{z=0}, \ Sh_2 = -\frac{h}{k(C_1 - C_2)} \left(\frac{\partial C}{\partial z}\right) |_{z=d} . \tag{8.17}$$

In dimensionless form, Sherwood numbers can be written as

$$Sh_1 = -\phi'(0), \ Sh_2 = -\phi'(1). \tag{8.18}$$

8.3 Solution Procedures

8.3.1 Collacation Method

The simulation of system of Eqs. $(8.9 - 8.13)$ with conditions (8.14) is accomplished with the technique based on finite difference namely bvp4c in Matlab. The scheme bvp4c is a collacation method for solving system of first order which implements the three-stage Lobatto IIIa formula. An initial guess that fulfills the boundary conditions is required to approximate the solution of the governing problem. The initial guess is modified for further iterations by builtin method namely finite difference. To carry out this numerical scheme, the first order ODEs system is obtained by reducing the higher order ODEs. To convert this, introducing the following new variables:

$$f = \chi_1, \ f' = \chi_2, \ f'' = \chi_3, \ g = \chi_4, \ g' = \chi_5, \ P = \chi_6, \ \theta = \chi_7, \ \theta' = \chi_8, \ \phi = \chi_9, \ \phi' = \chi_{10}, \tag{8.19}$$

$$\chi_1' = \chi_2, \ \chi_2' = \chi_3, \tag{8.20}$$

$$\chi_3' = \frac{Re\left\{\left(\chi_2^2 - \chi_4 - 2\chi_1\chi_3\right) - \beta_1\left(4\chi_1\chi_2\chi_3 - 4\chi_1\chi_4\chi_5\right) + M\left(\chi_2 - 2\beta_1\chi_1\chi_3\right)\right\} - \Lambda}{\left(1 - 4Re\beta_1\chi_1^2\right)}, \tag{8.21}$$

$$\chi_4' = \chi_5, \tag{8.22}$$

$$\chi_5' = \frac{Re\left\{2\left(\chi_2\chi_4 - \chi_1\chi_5\right) - \beta_1\left(4\chi_1\chi_2\chi_5 + 4\chi_1\chi_3\chi_4\right) + M\left(\chi_4 - 2\beta_1\chi_1\chi_5\right)\right\}}{\left(1 - 4Re\beta_1\chi_1^2\right)}, \tag{8.23}$$

$$\chi_6' = Re\left(-4\chi_1\chi_2 + 8\beta_1\chi_1^2\chi_3\right) - 2\chi_3, \tag{8.24}$$

$$\chi_7' = \chi_8, \tag{8.25}$$

$$\chi_8' = \frac{-2Re\,\mathrm{Pr}\,\chi_1\chi_8 - \varepsilon\chi_8^2 - \mathrm{Pr}\,Nb\chi_8\chi_{10} - \mathrm{Pr}\,Nt\chi_8^2}{\left(1 + \varepsilon\chi_7\right)}, \tag{8.26}$$

$$\chi_9' = \chi_{10}, \tag{8.27}$$

$$\chi_{10}' = -2ReSc\chi_1\chi_{10} - \frac{Nt}{Nb}\chi_8', \tag{8.28}$$

with conditions

$$\chi_1(0) = 0, \ \chi_2(0) = S_1, \ \chi_4(0) = 1, \ \chi_6(0) = 1, \ \chi_7(0) = 1, \chi_9(0) = 1,$$

$$\chi_1(1) = 0, \ \chi_2(1) = S_2, \ \chi_4(1) = \omega_1, \ \chi_7(1) = 0, \ \chi_9(1) = 0, \tag{8.29}$$

8.3.2 Runge-Kutta-Fehlberg (RKF45) Method

The system of Eqs. $(8.9 - 8.13)$ with conditions (8.14) is also solved with the numerical scheme (RKF45) with intention to validate the outcomes obtained by the bvp4c.

8.3.3 Results Validation

The validation of numerical code is reported for the case by neglecting the stretching effects in both disks. **Table 8.1** is displayed for the comparison of our numerical results with those of Lance and Rogers [34] and Turkyilmazoglu [35] for multiple variation of $\Omega = -0.5, \ 0.0, \ 0.5$ at Reynolds number $Re = 0, 10$. **Table 8.2** also describes the numerical values of radial $f''(0)$ and axial skin frictions with various values of rotation number $\Omega = -0.5, \ 0.0, \ 0.5$ at Reynolds number $Re = 0, 10$. It is seen that our results match in an excellent way with aforementioned references. **Table 8.3** is computed to validate the present bvp4c scheme with Runge-Kutta-Fehlberg method (RKF45) in Maple. From this table it is clear that the present results have

excellent match with the results obtained with RKF45.

8.4   Results and Discussion

In this section, the numerical results are plotted and tabulated in order to visualize the effects of different parameters like the stretching parameters (S_1, S_2), rotation parameter ω_1, magnetic number M, Reynolds number Re, Deborah number β_1, thermal conductivity parameter ε, Schmidt number Sc, thermophoresis Nt, and Brownian motion Nb parameters on the velocity (radial $f'(\eta)$, axial $g(\eta)$ and azimuthal $f(\eta)$), temperature $\theta(\eta)$, concentration $\phi(\eta)$ and pressure $P(\eta)$ profiles. The entire computational analysis is performed by fixing the values of parameters as $S_1 = S_2 = 0.5$, $Nt = 0.2$, $Re = 5.0$, $\beta_1 = 0.1$, $M = 0.2$, $Pr = 1.0$, $\varepsilon = 0.2$, $Sc = 2.0$ and $Nb = 0.2$.

In **Figs. 8.2(a-d)** and **8.3(a-d)**, the impact of rotation parameter ω_1 and stretching parameters (S_1, S_2) on thermal and flow fields with the fixed value of $Re = 5.0$ is shown. It is mentioned here that the value $\omega_1 < 0$ portrays the case when directions of rotation of both disks are opposite to each other, $\omega_1 = 0$ implies the upper disk stationary situation and $\omega_1 > 0$ represents the case of where both disks are rotating in the same directions. It is notable here that $|\omega_1| < 1$, as reported in this study, depicts the condition where lower disk is rotating with higher speed than the upper disk.

Figs. 8.2(a-d) represent the development of stretching parameter S_2 on flow and thermal distribution curves in the situation when $(S_1 = 0)$. When stretching rate of upper disk is zero $(S_2 = 0)$, the sign of $f(\eta)$ denoting axial velocity component is positive for both same and opposite rotation directions. Thus, the fluid motion happens from slower rate towards faster rate rotating disk. Consequently, at the vicinity of lower disk the radial velocity $f'(\eta)$ is perceived positive and negative near the upper disk. It is detected that the radial velocity changes its sign at the midway that is $\eta \simeq 0.5$, exhibiting the inflexional property about that point. As a consequence, the fluid drawn radially inwards over a slow rotating disk is radially thrown outwards over the fast rotating disk. The tangential velocity varies linearly as revealed in **Fig. 8.2(b)**.

When the upper disk is activated with the stretching rate $(S_2 = 0.5, 1.0)$, the vertical flow

direction alters from lower to upper disk as shown in **Fig. 8.2(a)**. This is happening on account of the stronger centrifugal forces caused by flourishing stretching rates. Thus the inward fluid drawn over the faster rotating disk is finally thrown away over the slower speed rotating disk. It is also noticed that the stronger rate of S_2 causes the shifting of inflection point towards the fast rotating disk in the radial velocity as revealed by **Fig. 8.2(c)**. It is observed that direction of radial flow changes at $\eta \simeq 0.7$ due to stretching and rotation phenomena showing that the radial flow magnitude speed up at the lower disk and at the upper disk radial velocity increase. Also, a maximum increase in the azimuthal velocity is observed with boosting up the upper disk stretching rate S_2 as depicted through **Fig. 8.2(b)**. In **Fig. 8.2(d)**, a decrease in temperature is observed as a result of decrease in stretching rate S_2. The impact of same and opposite disks rotation on radial and axial velocity components and temperature field is very slight while azimuthal velocity $g(\eta)$ has more prominent effect.

Figs. 8.3(a-d) reveal the thermal and momentum fields in the situation where the lower disk is functional at stretching rate $S_1 = 0.5$. Here the azimuthal velocity and heat transfer enhance with augmenting the upper disk stretching rate. Further, rising upper disk stretching rate , an axial push in the fluid motion is observed from the lower disk and fluid is thrown radially outwards from the faster rotating to slower rotating disk which can be visualized from the curves through **Figs. 8.3(a)** and **(c)**. It is revealed from **Fig. 8.3(c)** that the radial flow changes its direction at $\eta \simeq 0.7$ due to stretching and rotation phenomena. Here the magnitude of the radial velocity enhances at the lower disk and near the upper disk radial velocity increase.

The flow and temperature profiles with varying values of magnetic parameter M and $\omega_1 = -0.5$ and 0.5 are sketched in **Figs. 8.4(a-d)**. It is evident that the axial velocity at lower disk vicinity is a declining function of M while near the upper disk the magnitude of axial velocity decreases. A decrease in radial flow field is viewed near the lower and upper disks regions with higher magnetic field strength. The azimuthal velocity component is decreased throughout the flow region with increasing magnetic field. Physically, a drag like force is formed that resists the fluid movement on applying magnetic field which delivers a hindrance in velocity components and augmentation in fluid temperature as viewed in **Fig. 8.4(d)**.

Figs. 8.5(a-d) give the variation of velocity and temperature fields with the improvement in Reynolds number Re for the same rotation cases and both the disks stretch radially with

the same rates ($S_1 = S_2 = 0.5$). The axial flow rises with increasing Reynolds number Re. The radial velocity component intensifies near the lower disk and after the value $\eta \simeq 0.6$, an opposite behavior is watched. In **Fig. 8.5(b),** the azimuthal velocity component increases but the temperature profile diminishes as the effects of Reynolds number grow as can be depicted in **Fig. 8.5(d)**.

The results of flow and temperature fields with the variation in Deborah number β_1 when both disks rotate in the same direction ($\omega_1 = 0.5$) and in the absence of upper disk stretching are demonstrated in **Figs. 8.6(a-d)**. The radial and azimuthal components of velocity decay with Deborah number β_1 as depicted in **Figs. 8.6(a,b)**. The flow behavior in axial direction falls at the lower disk whereas the magnitude of axial velocity declines at the upper disk surface. As expected, the fluids that possess the low value of Deborah number, the viscous properties are predominant in comparison with elastic features. On the other hand, higher Deborah number fluids have to characteristics of elastic solid material. The fluid temperature rises as the Deborah number increases as shown in **Fig. 8.6(d)**.

Figs. 8.7(a,b) show the influence of thermal conductivity parameter ε and Prandtl number Pr on temperature field $\theta(\eta)$. Temperature profile escalates with increasing the values of ε. As fluid thermal conductivity has direct relation with ε and as a result larger mount of heat occur which is transferred to the fluid by the disk surface due to which the fluid temperature rises. A fall in the temperature profile is observed through **Fig. 8.7(b)** with accelerating Pr in the absence of upper disk stretching $S_2 = 0$. Physically, thermal diffusivity is reduced with higher value of Prandtl number.

The nanofluid active parameters namely, Nt and Nb play a significant role on mass and heat transport features. The prominence of Nt on $\theta(\eta)$ is depicted in **Fig. 8.8(a)**. There is a significant increase in temperature with higher values of Nt. Actually, escalating value of Nt implies the strengthening the thermophoresis forces which have the tendency to transport the nanoparticles from hotter towards the cooler at the cost of increasing the fluid temperature. **Fig. 8.8(b)** represents the temperature profile against the impact of Nb. The consequence of Nb is to upsurges the $\theta(\eta)$. As the value of Nb is incremented, the random motion of the fluid particles develops which causes to increase the temperature distribution.

Figs. 8.9(a,b) emphasis on the efficiency of thermophoresis Nt and Schmidt number Sc

on the concentration profile $\phi(\eta)$. The effect of Nt is to decrease the concentration profile. The outcomes of Sc on curves of concentration are shown in **Fig. 8.9(b)**. The action of Sc is to reduce the profile of concentration. Since Schmidt number and Brownian diffusion coefficient are inversely related which causes the reduction in concentration distribution.

In **Figs. 8.10(a,b)**, the impact of Reynolds number Re and Deborah number β_1 on pressure field $P(\eta)$ is portrayed. The pressure profile near the lower disk surface decreases while at the upper disk an opposite development is observed. The influence of Deborah number β_1 is to diminish the pressure profile.

In **Fig. 8.11(a)**, the pressure gradient parameter Λ is plotted against Deborah number β_1 with various $Re = 1.0, 2.0, 3.0, 4.0$, by considering the stretching rate of upper disk to be zero $(S_2 = 0.0)$ while the lower disk is operated at stretching as $S_1 = 0.5$. The sway of β_1 is to diminishes the pressure gradient parameter Λ whereas increasing Reynolds number increases the pressure gradient parameter Λ. For $Re = 1.0$, by increasing Deborah number a very slight decrease in Λ is observed. However, increasing Reynolds number makes this reduction more significant. In **Fig. 8.11(b)**, the pressure gradient Λ is sketched for S_2 and varying magnetic field parameter values. Increasing the upper disk stretching rate, upsurges the pressure gradient parameter Λ whereas the growing magnetic filed effects decreases Λ.

The heat transfer rates $-\theta'(0)$ and $-\theta'(1)$ at the lower and the upper disks, respectively, with various values of M, Re, Pr, S_2, ε and Nt are numerically computed through **table 8.4.** Here the $-\theta'(0)$ reduces at the lower disk with upgrading estimations of S_2, M ε and Nt while a reverse conduct is detected at the upper disk. The impact of Reynolds number Re is to boosts up the heat transfer rate at the lower and decrease at the upper disk. The heat transfer rates at the lower and the upper disks are increasing function of Prandtl number.

Table 8.1: A comparison of $F''(0)$, $-G'(0)$ and Λ against numerous ω_1 in non-stretching case $S_1 = S_2 = 0$ when $Re = 1$ and $M = 0 = \beta_1$.

	ω_1	-1.0	-0.8	-0.3	0.0	0.50
$F''(0)$	Ref. [34]	0.06666000	0.08394000	0.10395000	0.09997000	0.06663000
	Ref. [35]	0.06666313	0.08394206	0.10395088	0.09997221	0.06663419
	Observe	0.06666258	0.08394164	0.10395000	0.09997146	0.06663400
$-G'(0)$	Ref. [34]	2.00095000	1.80259000	1.30442000	1.00428000	0.50261000
	Ref. [35]	2.00095215	1.80258847	1.30442355	1.00427756	0.50261351
	Observe	2.00095200	1.80258800	1.30442300	1.00427700	0.50261350
Λ	Ref. [34]	0.19992000	0.17185000	0.20636000	0.29924000	0.57458000
	Ref. [35]	0.19991538	0.17184642	0.20635721	0.29923645	0.57457342
	Observe	0.19991651	0.17184728	0.20635898	0.29923784	0.57457377

Table 8.2: A comparison of $f''(0)$ and $-g'(0)$, against numerous Re and ω_1 when $S_1 = 0.5 = S_2$ and $M = 0 = \beta_1$.

		$f''(0)$		$-g'(0)$	
Re	ω_1	Ref. [35]	Observe	Ref. [35]	Observe
0	-0.5	-2.00000007	-2.0000000	1.50000000	1.50000000
10		-1.60562889	-1.6056320	3.40116128	3.40119500
0	0.0	-2.00000007	-2.0000000	1.00000000	1.0000000
10		-1.44561724	-1.4456070	2.56217438	2.5621880
0	0.5	-2.00000007	-2.0000000	0.50000000	0.5000000
10		-1.89459839	-1.8945800	1.50020105	1.5002260

Table 8.3. Comparison values between bvp4c and RK Fehlberg methods for Nusselt number Nu_1 and Sherwood number Sh_1 at the lower disk when $S_1 = S_2 = \omega_1 = 0.5,\ \beta_1 = 0.1,\ M = 1.0,\ Re = 5.0,\ \Pr = 2.0,\ Nt = Nb = 0.2$, and $Sc = 2.0$.

	Nu_1			Sh_1	
Pr	bvp4c	RK Fehlberg	Sc	bvp4c	RK Fehlberg
1.0	0.7607183	0.7607184	1.0	1.446996	1.446996
2.0	0.6888794	0.6888793	1.5	1.520110	1.520110
3.0	0.6190098	0.6190093	2.0	1.595939	1.595940
4.0	0.5521271	0.5521260	2.5	1.674528	1.674529

Table 8.4. Nusselt numbers Nu_1 at the lower disk and Nu_2 at the upper disk when $S_1 = \omega_1 = 0.5,\ \beta_1 = 0.1, Nb = 0.2$, and $Sc = 2.0$.

| S_2	M	Re	Pr	ε	Nt	Nu_1	Nu_2
0.0	1.0	5.0	2.0	0.5	0.2	0.859295	1.333642
0.4						0.719970	1.805687
0.8						0.604426	2.308052
0.0	0.0					0.885851	1.282024
	0.5					0.871460	1.311182
	1.0					0.859295	1.333642
	1.0	0.0				0.611654	1.717482
		3.0				0.756705	1.475842
		6.0				0.911463	1.268939
		5.0	1.0			0.846418	1.291801
			3.0			0.871950	1.375445
			5.0			0.896550	1.458619
			2.0	0.0		1.039902	1.058778
				0.3		0.915346	1.224307
				0.6		0.836450	1.387988
				0.5	0.2	0.859295	1.333642
					0.4	0.737464	1.571611
					0.6	0.628838	1.827171
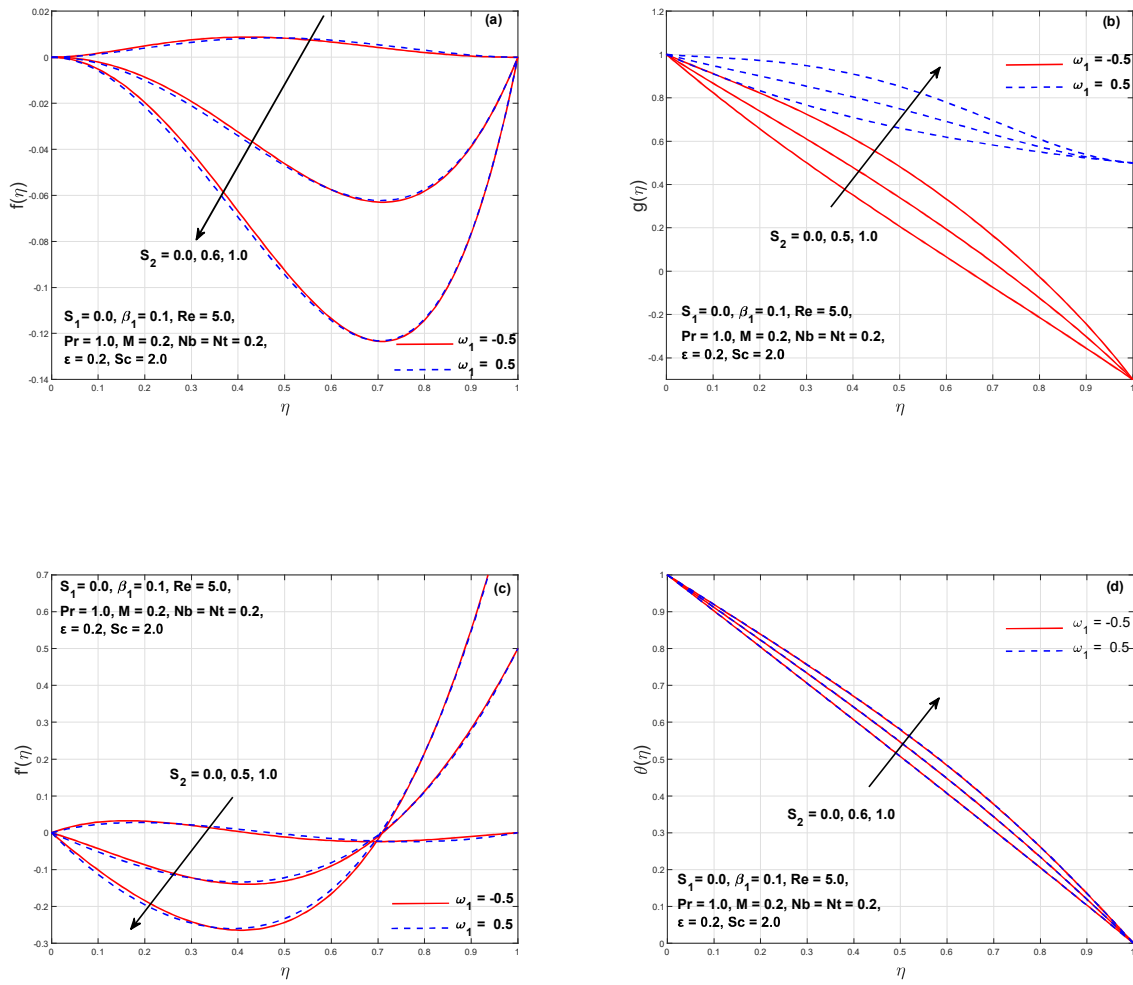
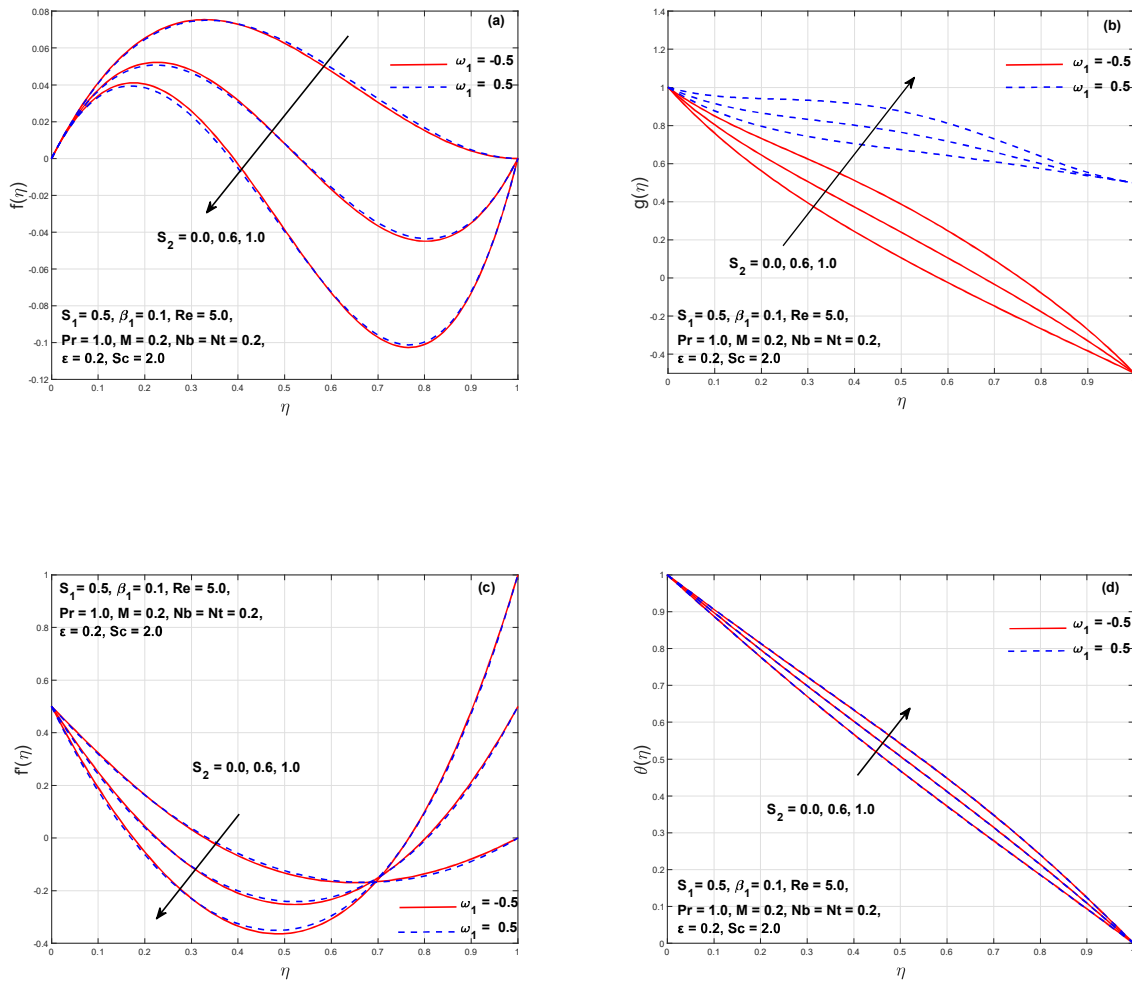**Fig. 8.2:** $f,\ g,\ \ f'$ and θ for S_2 with $S_1 = 0.0$.

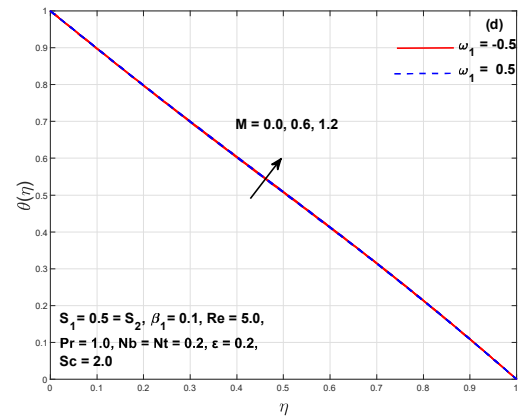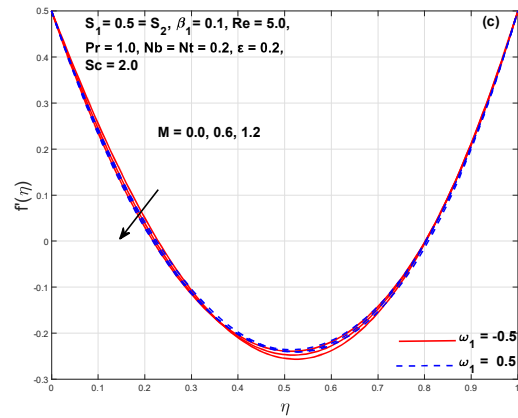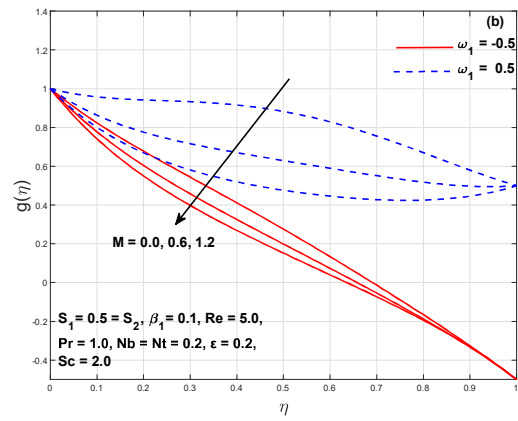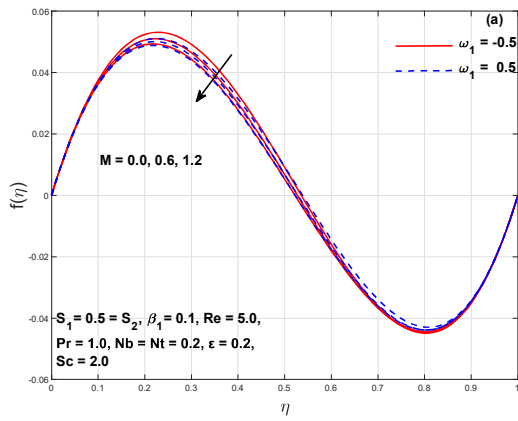**Fig. 8.3:** f, g, f' and θ for S_2 with $S_1 = 0.5$.
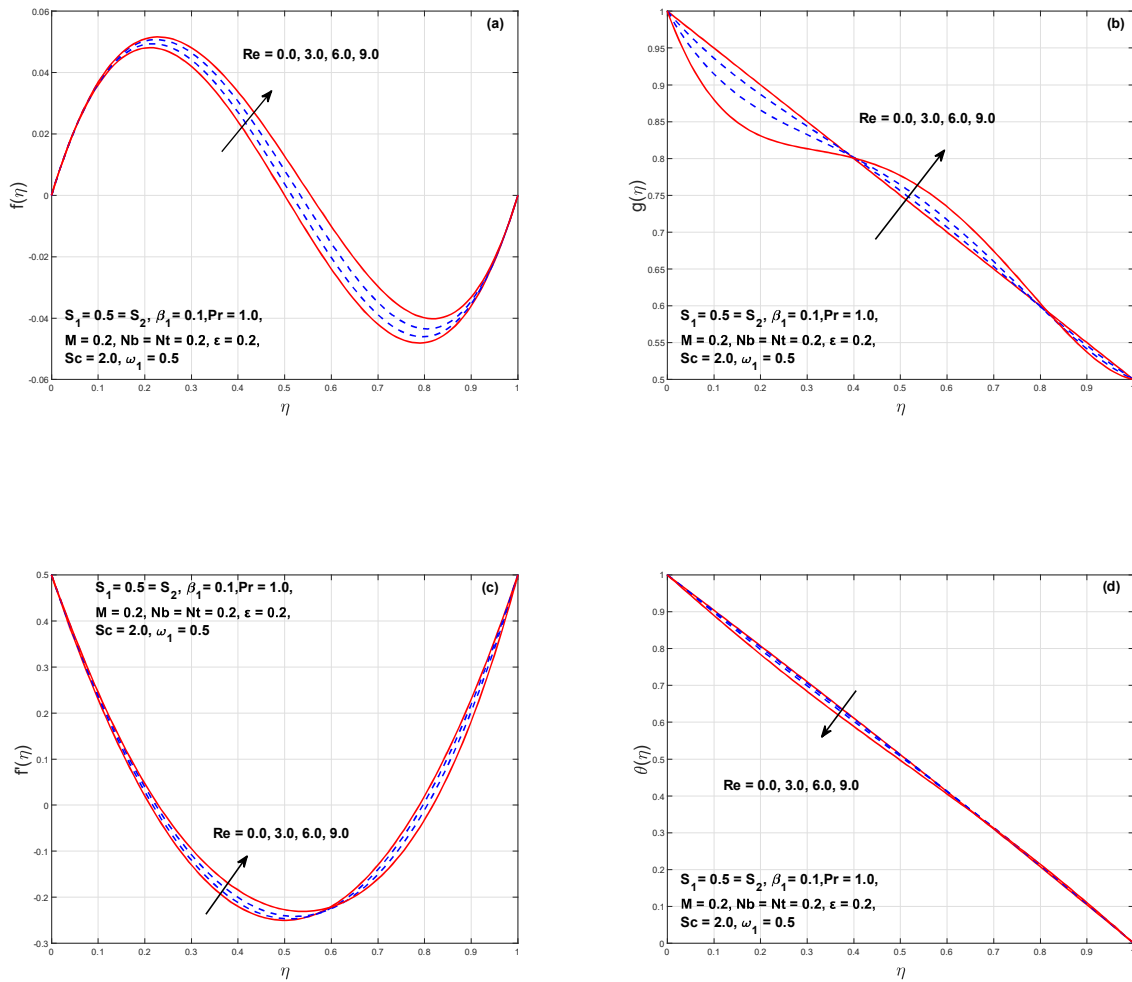
Fig. 8.4: f, g, f' and θ for M.
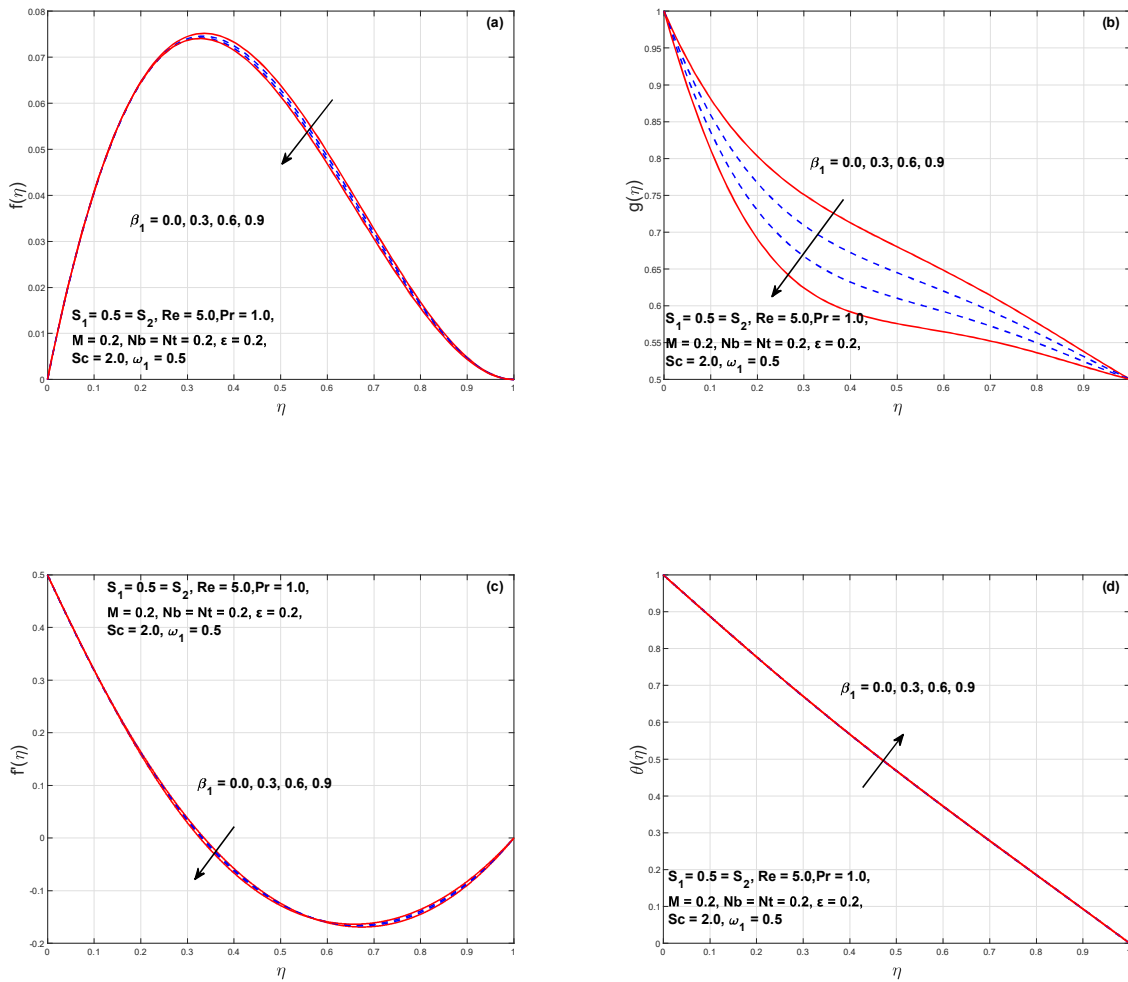
Fig. 8.5: f, g, f' and θ for Re.

Fig. 8.6: f, g, f' and θ for β_1.

(a)

$\theta(\eta)$

$\varepsilon = 0.0, 0.2, 0.4, 0.6$

$S_1 = 0.5 = S_2$, $\beta_1 = 0.1$, Pr = 1.0,
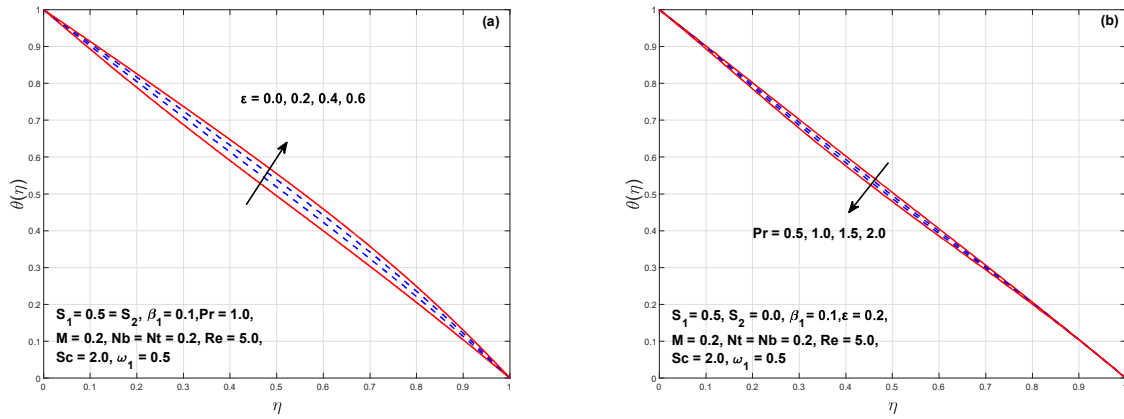M = 0.2, Nb = Nt = 0.2, Re = 5.0,
Sc = 2.0, $\omega_1 = 0.5$

η

(b)

$\theta(\eta)$

Pr = 0.5, 1.0, 1.5, 2.0

$S_1 = 0.5$, $S_2 = 0.0$, $\beta_1 = 0.1$, $\varepsilon = 0.2$,
M = 0.2, Nt = Nb = 0.2, Re = 5.0,
Sc = 2.0, $\omega_1 = 0.5$

η

Fig. 8.7: θ for ε and Pr.

(a)

$\theta(\eta)$

Nt = 0.2, 0.4, 0.6, 0.8

$S_1 = 0.5 = S_2$, $\beta_1 = 0.1$, Pr = 1.0,
M = 0.2, Nb = 0.2, Re = 5.0, $\varepsilon = 0.2$,
Sc = 2.0, $\omega_1 = 0.5$

η

(b)

$\theta(\eta)$

Nb = 0.1, 0.4, 0.7, 1.0

$S_1 = 0.5 = S_2$, $\beta_1 = 0.1$, Pr = 1.0,
M = 0.2, Nt = 0.2, Re = 5.0, $\varepsilon = 0.2$,
Sc = 2.0, $\omega_1 = 0.5$

η

Fig. 8.8: θ for Nt and Nb.

(a)

$\phi(\eta)$

Nt = 0.2, 0.4, 0.6, 0.8

$S_1 = 0.5 = S_2$, $\beta_1 = 0.1$, Pr = 1.0,
M = 0.2, Nb = 0.2, Re = 5.0, $\varepsilon = 0.2$,
Sc = 2.0, $\omega_1 = 0.5$

η

(b)

$\phi(\eta)$

Sc = 1.0, 2.0, 3.0, 4.0

$S_1 = 0.5 = S_2$, $\beta_1 = 0.1$, Pr = 1.0,
M = 0.2, Nb = Nb = 0.2, Re = 5.0,
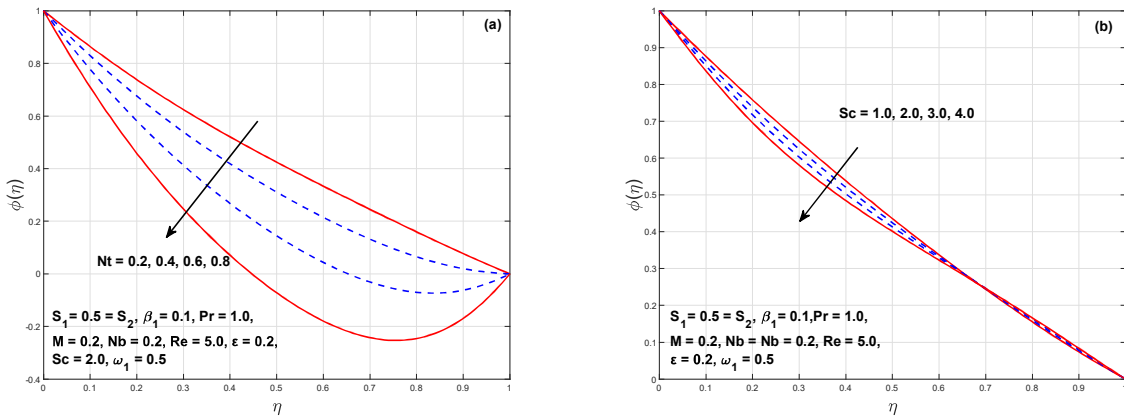$\varepsilon = 0.2$, $\omega_1 = 0.5$

η

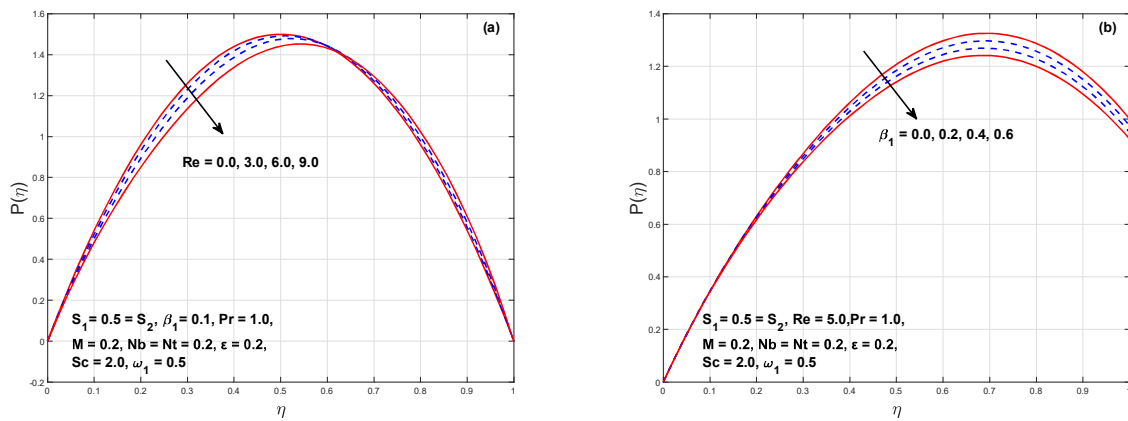**Fig. 8.9:** ϕ for Nt and Sc.

131
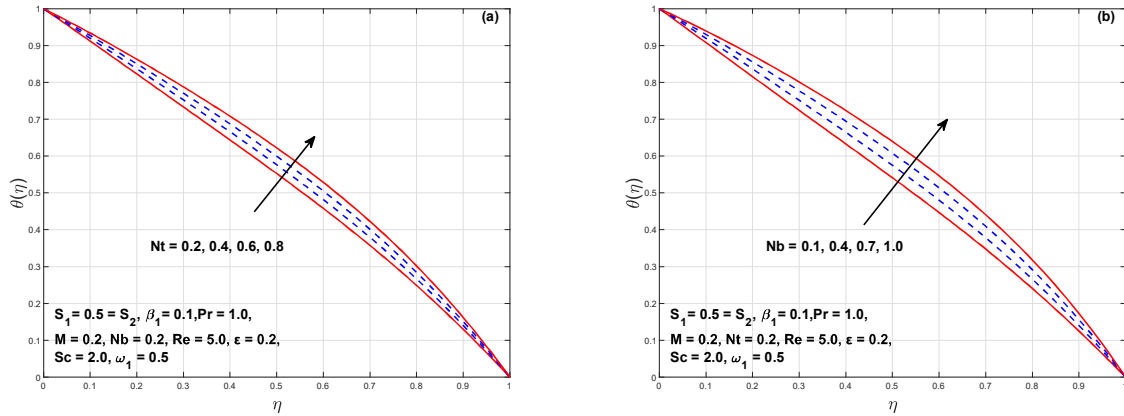
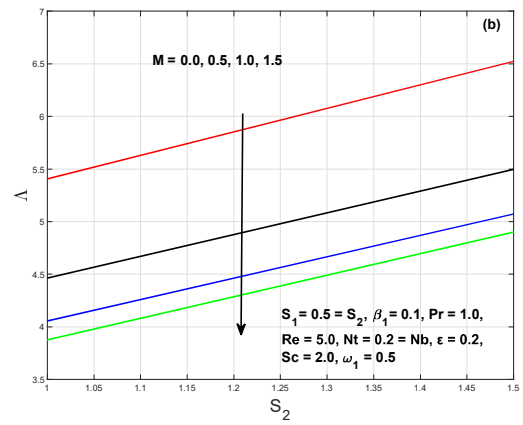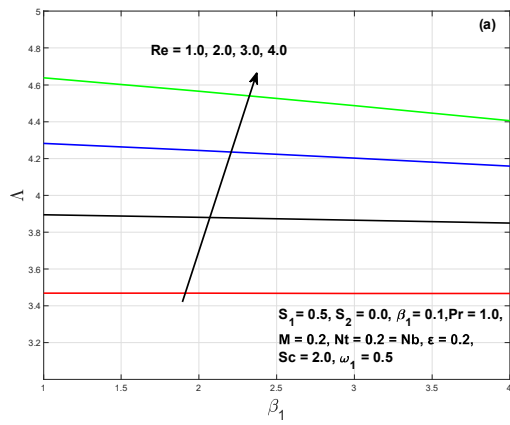**Fig. 8.10:** P for Re and β_1.

Fig. 8.11: Λ for Re and M.

Chapter 9

Homogeneous-Heterogeneous Reactions in Maxwell Fluid Flow Between Two Spiraling Disks

This chapter deals with the role of Cattaneo-Christov heat flux conduction model in rotating axisymmetic flow of Maxwell fluid between two coaxially spiraling disks. This model predicts the thermal relaxation characteristics. Two disparate situations, such as, when the direction of rotation of both disks is same and opposite are addressed. The system of nonlinear ODEs narrating the physical setup is obtained with the transformations executed by von Kármán. A finite difference algorithm based scheme, namely bvp4c, is implemented for numerical solution. The graphical and tabular trends for the radial, azimuthal, and axial flows as well as concentration and temperature fields are displayed against various pertinent quantities. The significant outcomes reveal that the impact of Deborah number is to decelerate the liquid motion all components. Additionally, the temperature field decays with the thermal relaxation time. Moreover, a decrease in fluid concentration is observed with increasing homogenous-heterogeneous reactions parameters.

9.1　Model Development

Here we consider an incompressible Maxwell fluid flow confined between two coaxially disks that are stretching and rotating at different rates. The mathematical modelling of the physical problem is described by choosing the cylindrical coordinated system (r, φ, z). The rotating and stretching velocities of lower disk positioned at $z = 0$ are, respectively, Ω_1 and s_1 while for upper disk positioned at $z = d$ are Ω_2 and s_2 as depicted in **Fig. 8.1**. The strength B_0 of magnetic flux is projected in vertical upward direction. Further, T_1 and T_2 represent the temperatures of the lower and upper disks, respectively.

The heat transfer analysis is considered with the imposition of convective conditions at the surfaces. Moreover, the homogeneous-heterogeneous reactions are considered. The above stated assumptions leads into following problem (Eqs. (8.1-8.3) Cf. Chapter **8**, Eqs. (4.1,4.2) Cf. Chapter **4**), Eqs. (3.1) Cf. Chapter **3**))

$$\frac{\partial}{\partial z}(w) + \frac{1}{r}\frac{\partial}{\partial r}(ru) = 0, \tag{9.1}$$

$$w\frac{\partial u}{\partial z} - \frac{v^2}{r} + u\frac{\partial u}{\partial r} = -\frac{1}{\rho}\frac{\partial p}{\partial r} + \nu\left(2\frac{\partial^2 u}{\partial r^2} + \frac{\partial^2 u}{\partial z^2} + \frac{\partial^2 w}{\partial r \partial z} + \frac{2}{r}\frac{\partial u}{\partial r} - \frac{2u}{r^2}\right)$$

$$-\lambda_1\left(-\frac{2uw}{r}\frac{\partial v}{\partial z} + u^2\frac{\partial^2 u}{\partial r^2} + w^2\frac{\partial^2 u}{\partial z^2} + 2uw\frac{\partial^2 u}{\partial r \partial z} - \frac{2uv}{r}\frac{\partial v}{\partial r} + \frac{uv^2}{r^2} + \frac{v^2}{r}\frac{\partial u}{\partial r}\right)$$

$$-\frac{\sigma B_0^2}{\rho}\left(u + w\lambda_1\frac{\partial u}{\partial z}\right), \tag{9.2}$$

$$w\frac{\partial v}{\partial z} + u\frac{\partial v}{\partial r} + \frac{uv}{r} = \nu\left(\frac{\partial^2 v}{\partial r^2} - \frac{v}{r^2} + \frac{1}{r}\frac{\partial v}{\partial r} + \frac{\partial^2 v}{\partial z^2}\right)$$

$$-\lambda_1\left(u^2\frac{\partial^2 v}{\partial r^2} + w^2\frac{\partial^2 v}{\partial z^2} + 2uw\frac{\partial^2 v}{\partial r \partial z} + \frac{2uv}{r}\frac{\partial u}{\partial r} + \frac{2vw}{r}\frac{\partial u}{\partial z} - \frac{2u^2v}{r^2} - \frac{v^3}{r^2} + \frac{v^2}{r}\frac{\partial v}{\partial r}\right)$$

$$-\frac{\sigma B_0^2}{\rho}\left(v + w\lambda_1\frac{\partial v}{\partial z}\right), \tag{9.3}$$

$$w\frac{\partial w}{\partial z} + u\frac{\partial w}{\partial r} = -\frac{1}{\rho}\frac{\partial p}{\partial z} + \nu\left(\frac{\partial^2 u}{\partial r \partial z} + \frac{\partial^2 w}{\partial r^2} + \frac{1}{r}\frac{\partial u}{\partial z} + \frac{1}{r}\frac{\partial w}{\partial r} + 2\frac{\partial^2 w}{\partial z^2}\right)$$

$$-\lambda_1\left(u^2\frac{\partial^2 w}{\partial r^2} + 2uw\frac{\partial^2 w}{\partial r \partial z} + w^2\frac{\partial^2 w}{\partial z^2} + \frac{v^2}{r}\frac{\partial w}{\partial r}\right), \tag{9.4}$$

135

$$\rho c_p \left(w \frac{\partial T}{\partial z} + u \frac{\partial T}{\partial r} \right) = k \left(\frac{\partial^2 T}{\partial z^2} + + \frac{1}{r} \frac{\partial T}{\partial r} + \frac{\partial^2 T}{\partial r^2} \right)$$

$$- \delta_E \left[u^2 \frac{\partial^2 T}{\partial r^2} + w^2 \frac{\partial^2 T}{\partial z^2} + 2uw \frac{\partial^2 T}{\partial r \partial z} + \frac{\partial T}{\partial r} \left(w \frac{\partial u}{\partial z} + u \frac{\partial u}{\partial r} \right) + \frac{\partial T}{\partial z} \left(w \frac{\partial w}{\partial z} + u \frac{\partial w}{\partial r} \right) \right], \qquad (9.5)$$

$$w \frac{\partial a}{\partial z} + u \frac{\partial a}{\partial r} = d_A \left(\frac{\partial^2 a}{\partial z^2} + \frac{\partial^2 a}{\partial r^2} + \frac{1}{r} \frac{\partial a}{\partial r} \right) - k_c a b^2, \qquad (9.6)$$

$$w \frac{\partial b}{\partial z} + u \frac{\partial b}{\partial r} = d_B \left(\frac{\partial^2 b}{\partial z^2} + \frac{\partial^2 b}{\partial r^2} + \frac{1}{r} \frac{\partial b}{\partial r} \right) + k_c a b^2. \qquad (9.7)$$

with conditions

$$u = s_1 r, \ v = \Omega_1 r, \ w = 0, \ T = T_1, \ d_A \frac{\partial a}{\partial z} = k_s a, \ d_B \frac{\partial b}{\partial z} = -k_s a \ \text{at} \ z = 0,$$

$$u = s_2 r, \ v = \Omega_2 r, \ T = T_2, \ a \to a_0, \ b \to 0 \ \text{at} \ z = d, \qquad (9.8)$$

where the velocity components (u, v, w) are in (r, φ, z) directions, respectively, ν the kinematic viscosity, λ_1 the relaxation time parameter, p the liquid pressure, c_p the specific heat, ρ the liquid density, (d_A, d_B) the diffusion coefficients, $h_i (i = 1, 2)$ the heat transfer coefficients, where $\Omega_i \ (i = 1, 2)$ are the swirling rates, and $s_i \ (i = 1, 2)$ the stretching rates.

Defining the transformations

$$u = f'(\eta) \Omega_1 r, \ v = g(\eta) \Omega_1 r, \ w = -2f(\eta) h \Omega_1, \ p = \rho \Omega_1 \nu \left(P(\eta) + \frac{1}{2} \frac{r^2}{h^2} \Lambda \right),$$

$$\theta(\eta) = \frac{T - T_2}{T_1 - T_2}, \ \phi(\eta) = \frac{a}{a_0}, \ \psi(\eta) = \frac{b}{a_0}, \ \eta = \frac{z}{d}. \qquad (9.9)$$

In dimensionless structure, Eqs. $(9.1 - 9.7)$, and (9.8) are stated as

$$f''' - Re \left(f'^2 - g^2 - 2ff'' \right) + Re \beta_1 \left(4ff'f'' - 4f^2 f''' - 4fgg' \right)$$

$$- MRe \left(f' - 2\beta_1 ff'' \right) + \Lambda = 0, \qquad (9.10)$$

$$g'' + 2Re \left(fg' - f'g \right) + Re \beta_1 \left(4ff'g' - 4f^2 g'' + 4ff''g \right) - MRe \left(g - 2\beta_1 fg' \right) = 0, \qquad (8.11)$$

$$P' = -2f'' - Re \left(4ff' - 8\beta_1 f^2 f'' \right), \qquad (9.12)$$

136

$$\theta'' + 2Re\,Pr\,f\theta' - 4\,Pr\,Re\lambda_E\left(f^2\theta'' + ff'\theta'\right) = 0, \tag{9.13}$$

$$\frac{1}{Sc}\phi'' + Re\left(2f\phi' - k_1\phi\psi^2\right) = 0, \tag{9.14}$$

$$\frac{\delta_1}{Sc}\psi'' + Re\left(2f\psi' + k_1\phi\psi^2\right) = 0, \tag{9.15}$$

with conditions

$$f(0) = 0,\ f'(0) = S_1,\ g(0) = 1,\ P(0) = 1,\ \theta(0) = 1, \phi'(0) = k_2\phi(0),\ \delta_1\psi'(0) = -k_2\phi(0),$$

$$f(1) = 0,\ f'(1) = S_2,\ g(1) = \omega_1,\ \theta(1) = 0,\ \phi(1) = 1,\ \psi(1) = 0, \tag{9.16}$$

where Λ is pressure gradient parameter which is unknown. The dimensionless parameter $Re\left(= \frac{\Omega_1 d^2}{\nu}\right)$ is the Reynolds number, $\beta_1\left(= \lambda_1\Omega_1\right)$ the Deborah number, $M\left(= \frac{\sigma B_0^2}{\rho\Omega_1}\right)$ the magnetic parameter, $Pr\left(= \frac{v}{\alpha}\right)$ the Prandtl number, $S_i\left(= \frac{s_i}{\Omega_i}\right)(i = 1, 2)$ the scaled stretching parameters, $\omega_1\left(= \frac{\Omega_2}{\Omega_1}\right)$ the rotation number, $\lambda_E\left(= \delta_E\Omega_1\right)$ the thermal relaxation time, $k_1\left(= \frac{k_c a_0^2}{\Omega_1}\right)$ the homogeneous reaction parameter, $k_2\left(= \frac{k_s d}{D_A}\right)$ the heterogeneous reaction parameter, $Sc\left(= \frac{\nu}{D_A}\right)$ the Schmidt number and $\delta\left(= \frac{D_B}{D_A}\right)$ the diffusion coefficient ratio.

Here the coefficients (d_A, d_B) for diffusion are assumed having same magnitude. This postulate results in to investigate the chemical reaction analysis such that d_A and d_B are equal *i.e.* $\delta_1 = 1$. This assumption leads to the following relationship

$$\phi(\eta) + \psi(\eta) = 1. \tag{9.17}$$

Thus, Eqs. (9.14) and (9.15) turn into

$$\frac{1}{Sc}\phi'' + 2Ref\phi' - Rek_1\phi\left(1 - \phi\right)^2 = 0, \tag{9.18}$$

with conditions

$$\phi'(0) = k_2\phi(0),\ \phi(1) = 1. \tag{9.19}$$

9.2 Solution Approach

The coupled system of Eqs. $(9.10 - 9.13)$ and (9.18) representing the momentum, energy, pressure, temperature and concentration with conditions in Eqs. $(9.16, 9.19)$ is integrated numerically with the bvp4c solver in Matlab. The basic theme of bvp4c solver is the utilization of Lobatto IIIA formula. To estimate the solution the initial iterations that fulfill the boundary conditions are needed. Once the initial guesses are given, then iteration process is continued by modifying the initial guess with another method called finite difference method. This built-in method can be implemented by altering the partially coupled differential equations into set of first order differential equations. For this purpose, we define the following new variables. Let,

$$ f = x_1, \ f' = x_2, \ f'' = x_3, \ g = x_4, \ g' = x_5, \ P = x_6, \ \theta = x_7, \ \theta' = x_8, \ \phi = x_9, \ \phi' = x_{10}, \quad (9.20) $$

$$ x_1' = x_2, \ x_2' = x_3, $$

$$ x_3' = \frac{Re \left\{ \left(x_2^2 - x_4 - 2x_1 x_3\right) - \beta_1 \left(4 x_1 x_2 x_3 - 4 x_1 x_4 x_5\right) + M \left(x_2 - 2\beta_1 x_1 x_3\right) \right\} - \Lambda}{\left(1 - 4Re\beta_1 x_1^2\right)}, \quad (9.21) $$

$$ x_4' = x_5, $$

$$ x_5' = \frac{Re \left\{ 2 \left(x_2 x_4 - x_1 x_5\right) - \beta_1 \left(4 x_1 x_2 x_5 + 4 x_1 x_3 x_4\right) + M \left(x_4 - 2\beta_1 x_1 x_5\right) \right\}}{\left(1 - 4Re\beta_1 x_1^2\right)}, \quad (9.22) $$

$$ x_6' = Re \left(-4 x_1 x_2 + 8 \beta_1 x_1^2 x_3\right) - 2 x_3, \quad (9.23) $$

$$ x_7' = x_8, $$

$$ x_8' = \frac{-2 Re \, Pr \, x_1 x_8 + 4 Re \, Pr \, \lambda_E x_1 x_2 x_8}{\left(1 - 4Re \, Pr \, \lambda_E x_1^2\right)}, \quad (9.24) $$

$$ x_9' = x_{10}, $$

$$ x_{10}' = -2 Re Sc x_1 x_{10} + Re Sc k_1 x_9 \left(1 - x_9\right)^2 \quad (9.25) $$

with conditions

$$ x_1(0) = 0, \ x_2(0) = S_1, \ x_4(0) = 1, \ x_6(0) = 1, \ x_7(0) = 1, x_{10} = k_2 x_9(0), $$

$$ x_1(1) = 0, \ x_2(1) = S_2, \ x_4(1) = \omega_1, \ x_7(1) = 0, \ x_9(1) = 1. \quad (9.26) $$

9.3 Discussion of Results

This segment reveals the physical description of the various pertinent parameters, namely, rotation parameter Ω, Deborah number β_1, Reynolds number Re, stretching parameters (S_1, S_2), magnetic number M, thermal relaxation time λ_E, Prandtl number Pr, homogenous-hetrogeneous parameters (k_1, k_2) and Schmidt number Sc on the radial $f'(\eta)$, azimuthal $g(\eta)$, and axial $f(\eta)$ velocities, temperature $\theta(\eta)$ and concentration $\phi(\eta)$ profiles.

For fixed value of $Re = 5.0$, **Figs. 9.1(a-d)** & **9.2(a-d)** represent the upshot of the thermal and flow fields against S_2 for $\omega_1 = -0.5$ and 0.5. The case is assumed $\omega_1 < 0$ when the lower disk is rotating in the opposite direction to upper one. The situation $\omega_1 > 0$ indicates the same direction of rotation of both disks. The value $\omega_1 = 0$ implies that the rotation rate of upper disk is zero. In this study we assume that $|\omega_1| < 1$, which depicts the situation where rotating speed of upper disk is less than the lower disk.

The variation in fluid flow and temperature distribution with the various values of upper disk stretching rate S_2 while considering the lower disk stretching rate S_1 to be zero is shown in **Figs. 9.1(a-d)**. It is viewed that when $S_2 = 0$, the values of axial velocity are positive for the rotation directions. Therefore, the fluid movement caused by slower to faster rate rotating disks. Thus, in the vicinity of lower rotating disk, a positive sign for radial velocity component is gained and it shows a negative sign in the vicinity of upper rotating disk. Carefully observing that the change of sign happens at the value $\eta \simeq 0.5$, depicting the inflexional behavior about that value. Thus, at the faster rotating disk, the fluid is thrown outwards direction drawn radially inwards at the slower moving disk. The azimuthal velocity is seen in a linear trend as revealed in **Fig. 9.1(b)**. By operating the stretching rate $(S_2 = 0.4, 1.0)$, a change in the vertical flow direction from lower to upper disk is noted due to the development of centrifugal force caused by augmenting the stretching rates. Consequently, inward fluid drawn over faster rotating disk is ultimately pushed away at the slow rotating disk vicinity. Enhancing the stretching rate S_2 causes the shifting of inflection point towards the faster rotating disk. An increasing trend is observed in the azimuthal velocity component $g(\eta)$ with an increasing the upper disk stretching rate S_2. Furthermore, the impact of strengthening the upper disk stretching rate boosts up the fluid temperature as depicted in **Fig. 9.1(d)**. A slight influence on the radial and axial velocities

and temperature is observed by changing the direction of rotations. The effect of changing the direction of rotation is prominent on the azimuthal velocity $g(\eta)$.

Fig. 9.2(a) reveals the axial velocity $f(\eta)$ in the situation when the lower disk is kept at a stretching rate $S_1 = 0.5$. The axial velocity magnitude increases, thus more fluid is pushed by the upper disk. Furthermore, enhancing the upper stretching rate, more amount of fluid is moved axially from the upper disk and is thrown outward in the radial direction from the faster towards the slower rotating disks. A slight escalation in liquid temperature is observed with strengthening the stretching rate S_2.

Figs. 9.3(a-d) are sketched to visualize the influence of magnetic parameter M on flow and temperature field for opposite rotation direction ($\omega_1 = -0.5$) as well as for the same direction of rotations ($\Omega = 0.5$) and stretching both the disks ($S_1 = S_2 = 0.5$). The axial velocity near the lower disk surface decreases while at the upper disk surface, the magnitude of axial flow component diminishes. Near the lower and upper disks regions, the flow in the radial direction is found to decrease with improving magnetic field parameter M. The reason can be narrated that on applying magnetic field to fluid motion, a resistive force is created which hinder the motion of fluid in respective directions and because of that the fluid temperature boosts up as displayed in **Fig. 9.3(d)**.

Fig. 9.4(a-d) are plotted to inspect the influence of Re on the thermal and momentum fields for the case when ($\omega_1 = 0.5$) and keeping both of them at a fixed stretching rates ($S_1 = S_2 = 0.5$). An increase in vertical flow is perceived with enhancing Re. The radial velocity is observed in an increasing way with Re around the lower disk; however, an opposite movement is noticed after the point of inflection ($\eta \simeq 0.6$). It is anticipated through **Fig. 9.4(b)**, that motion in the azimuthal direction enlarges with the effect of Re. The temperature profile shows a decreasing performance with rising Re by reason of increase in viscosity as seen in **Fig. 9.4(d)**.

The effect of Deborah number β_1 on the velocity components in $r-$, $\varphi-$ and $z-$ directions as well as on temperature fields in the same direction ($\omega_1 = 0.5$) with $S_2 = 0.0$ is displayed in **Figs. 9.5(a-d)**. The flows in $r-$ and $\varphi-$ directions reduce as revealed by **Figs. 9.5(a,b)**. Over the lower disk, the velocity in axial direction falls while it decays in magnitude near the upper disk. The evidence can be presented with the physical justification that the liquids possessing small value of β_1, there is dominancy of viscous influence in respect of elastic effects. However,

fluids with higher value of β_1 tends to serve as an elastically solid material. On account of this justification, the fluid temperature rises marginally between the rotating disks which is delineated in **Fig. 9.5(d)**.

In **Fig. 9.6(a)**, there is a reduction noted in the fluid temperature $\theta(\eta)$ for increasing value of the Prandtl number Pr. Larger amount of Pr physically reduce the thermal diffusivity. The contours of temperature field with several estimation of λ_E are depicted in Fig. 9.6(b). Here the behavior of liquid temperature decelerates with stronger rate of λ_E. The growing value of λ_E is linked to the greater heat flux relaxation time and larger time is required by the fluid particles in exchanging heat to their nearby particles which creates a reduction in the fluid temperature.

The upshots of the parameters k_1 and k_2 representing homogeneous and heterogeneous reactions on the concentration distribution $\phi(\eta)$ are manefisted in **Figs. 9.7(a,b)**. In **Fig. 9.7(a)**, the concentration field depreciates with a continuous increase in the homogeneous reaction parameter k_1. This is due to the reason that the diffusion coefficients are overwhelmed by the response rates. In **Fig. 9.7(b)**, the upshot of k_2 is to reduce the species concentration. The upshots of Sc on concentration distribution can be depicted in **Fig. 9.7(c)**. Obviously, enhancing influence of Sc causes to intensify the fluid concentration. By considering $S_2 = 0.0$ and $S_1 = 0.5$, the pressure gradient parameter Λ versus Deborah number β_1 with numerous values of Re is sketched in **Fig. 9.8(a)**. The effect of β_1 is to lessen Λ while promoting Reynolds effects improve the value of Λ. An insignificant decline in Λ is seen with increasing β_1 for $Re = 1.0$. However, more significant effects in reduction of Λ are observed with greater values of Re. In **Fig. 9.8(b)** the pressure gradient Λ against S_2 is plotted with different values of M. By enhancing the value of S_2, an escalation in Λ is observed whereas the stronger magnetic field influence causes to decline Λ.
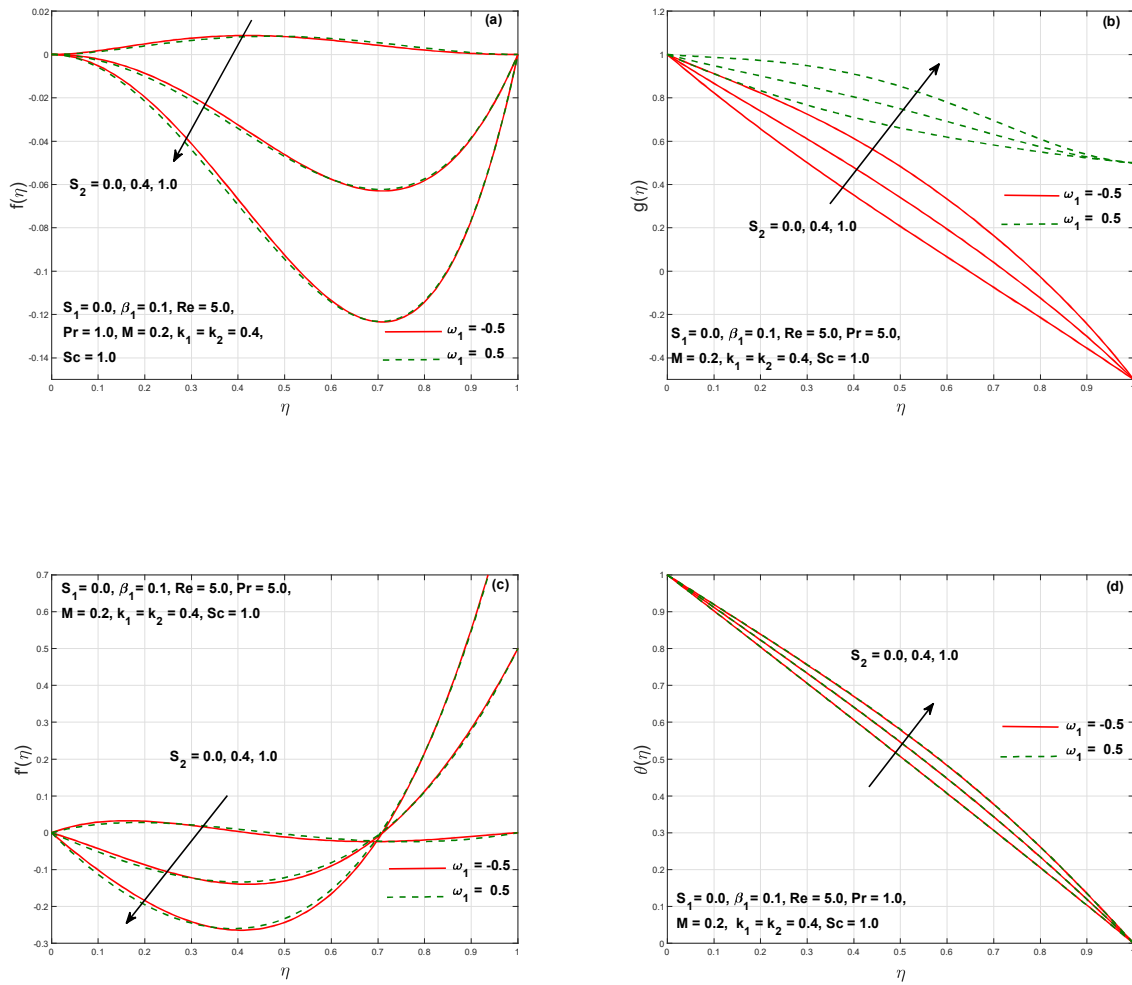
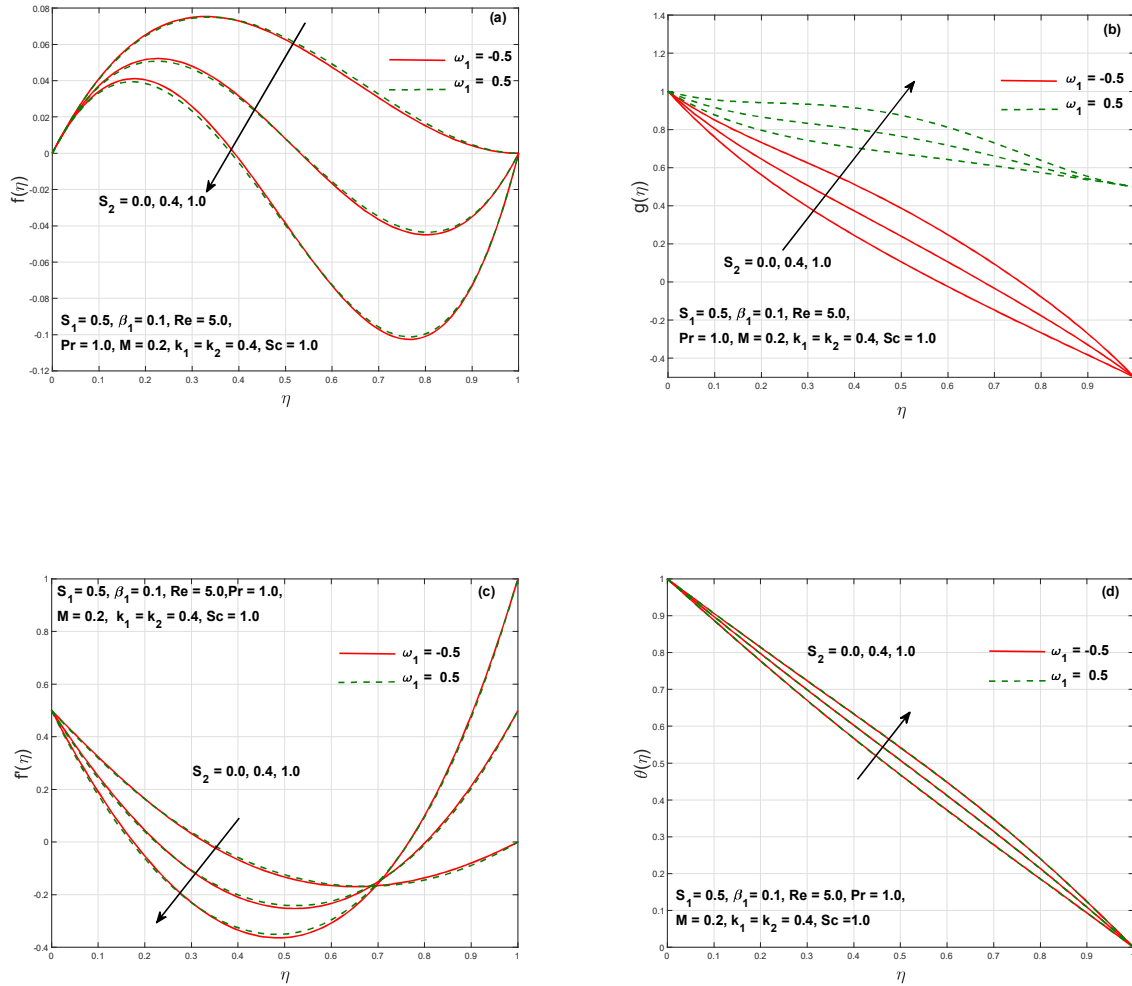**Fig. 9.1:** f, g, f' and θ for S_2 when $S_1 = 0.0$.

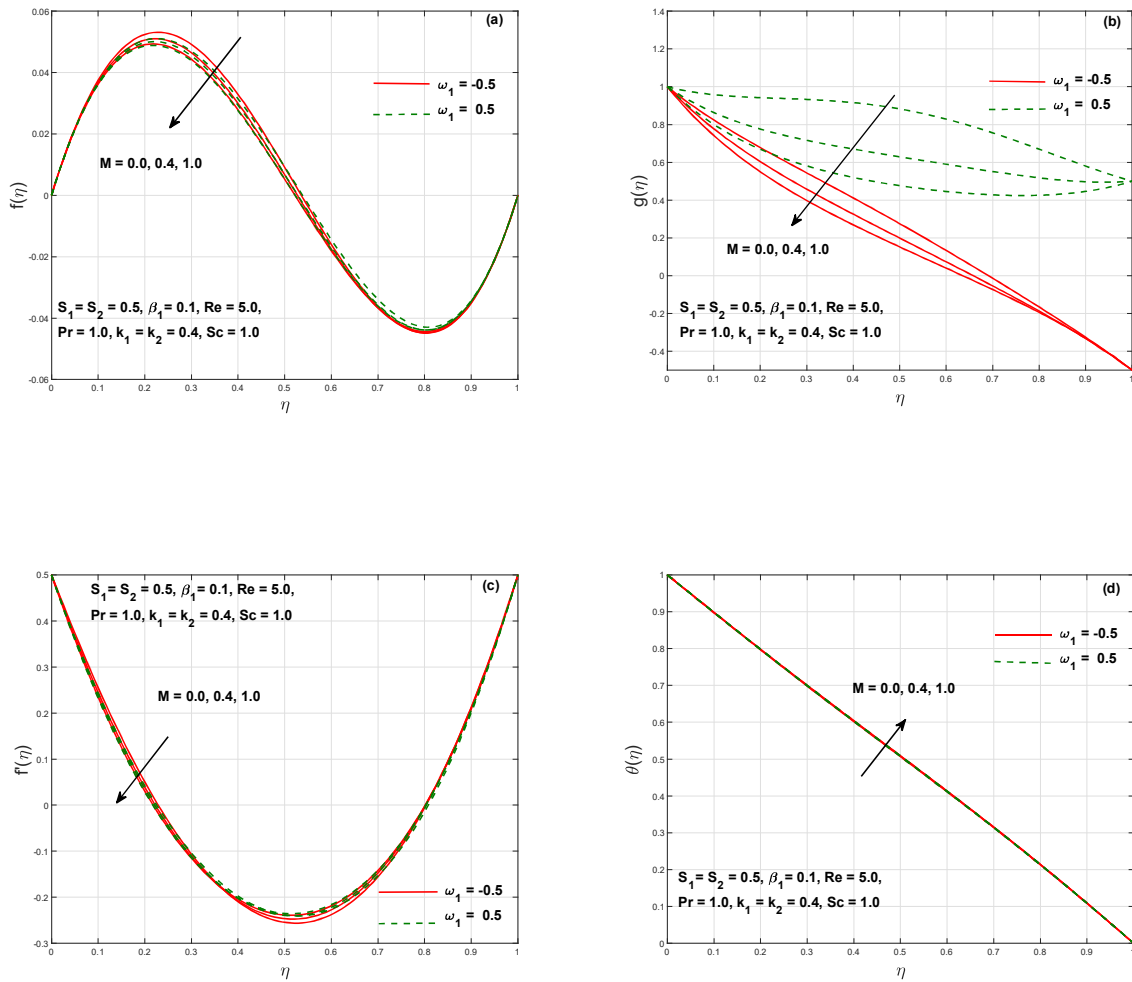**Fig. 9.2:** $f,\ g,\ f'$ and θ for S_2 when $S_1 = 0.5$.

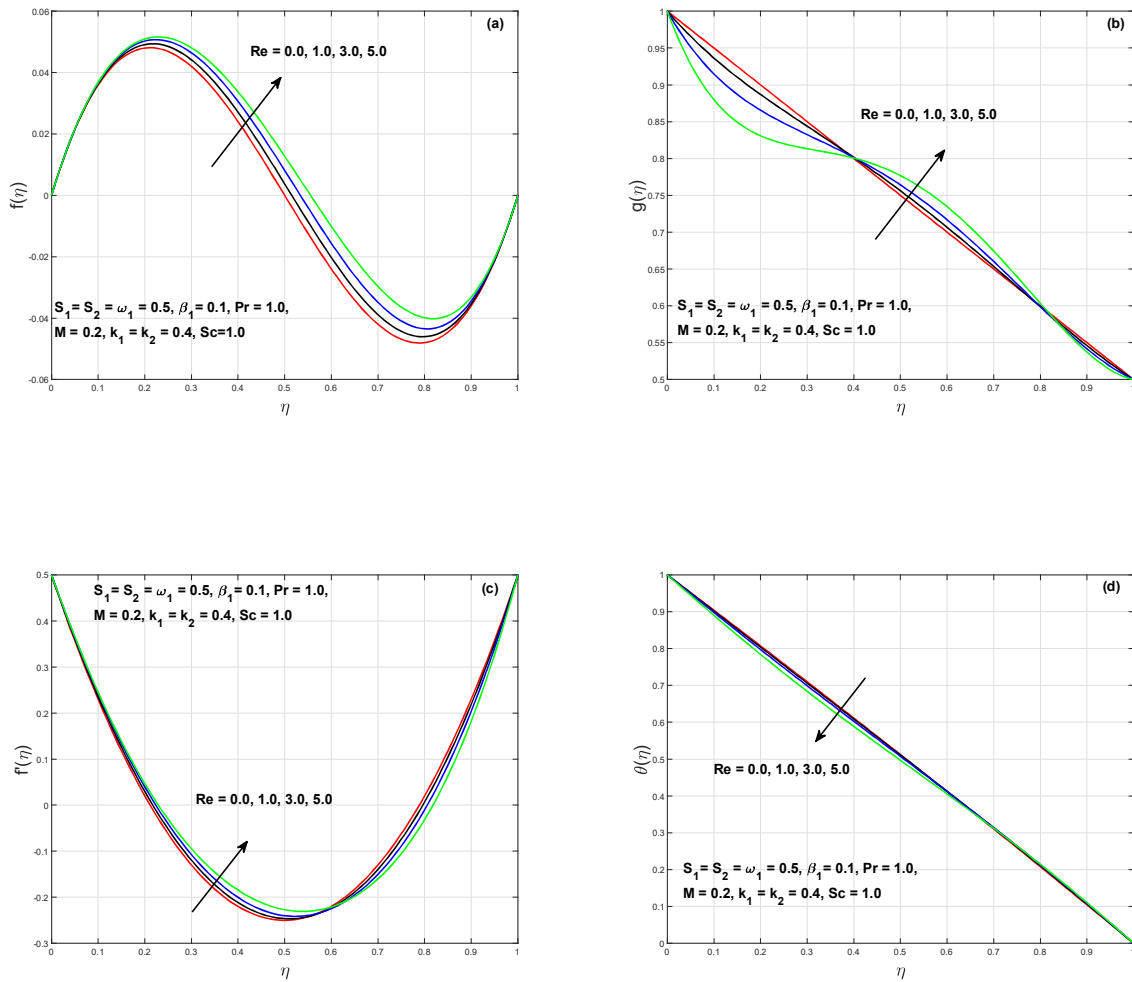**Fig. 9.3:** f, g, f' and θ for M.

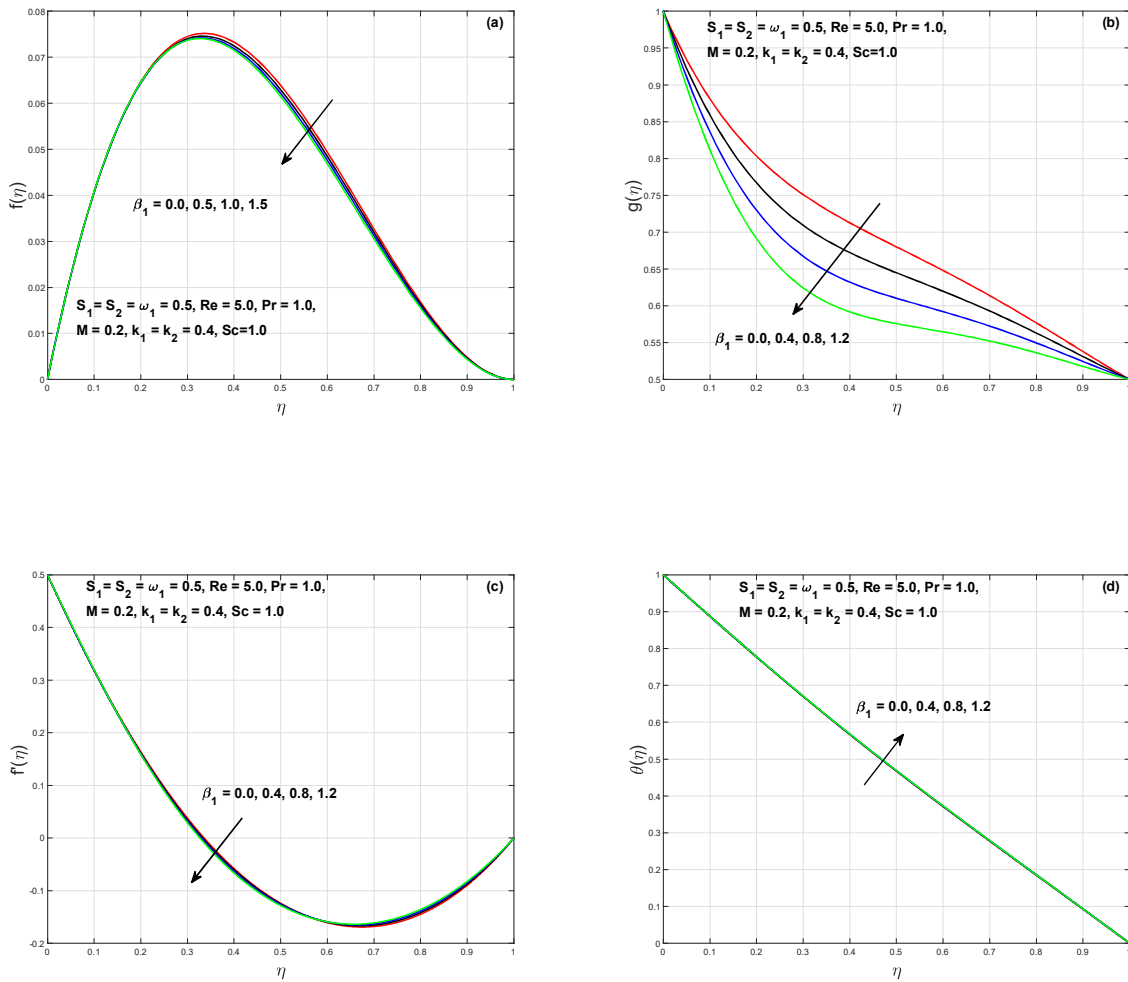**Fig. 9.4:** f, g, f' and θ for Re.
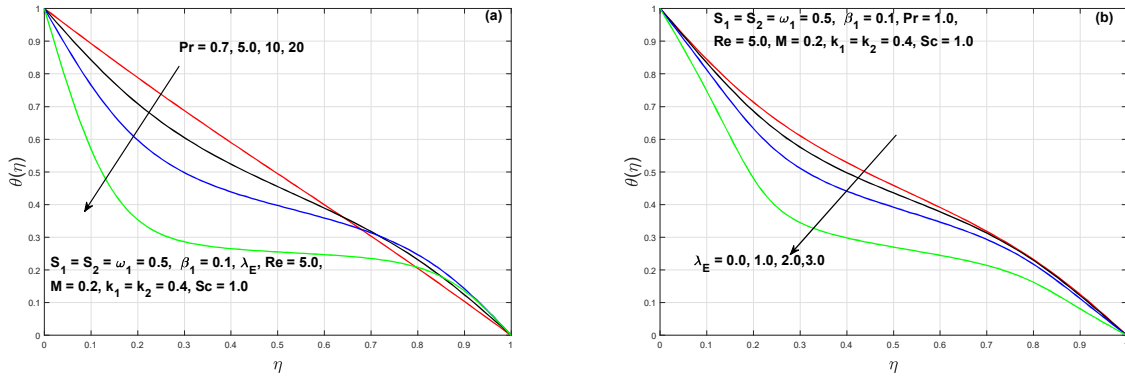
Fig. 9.5: f, g, f' and θ for β_1.
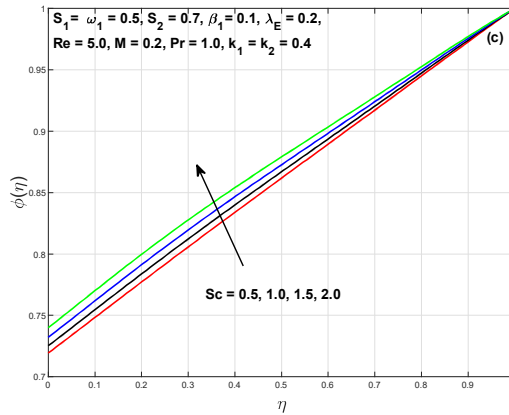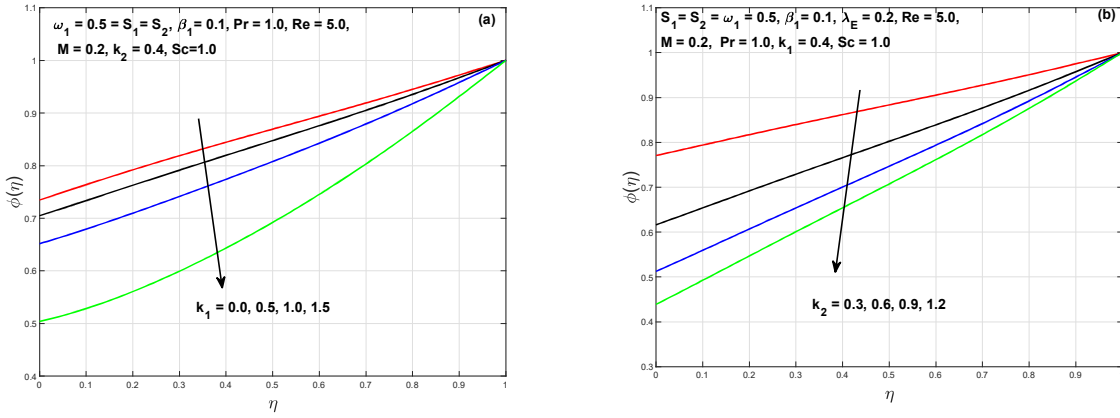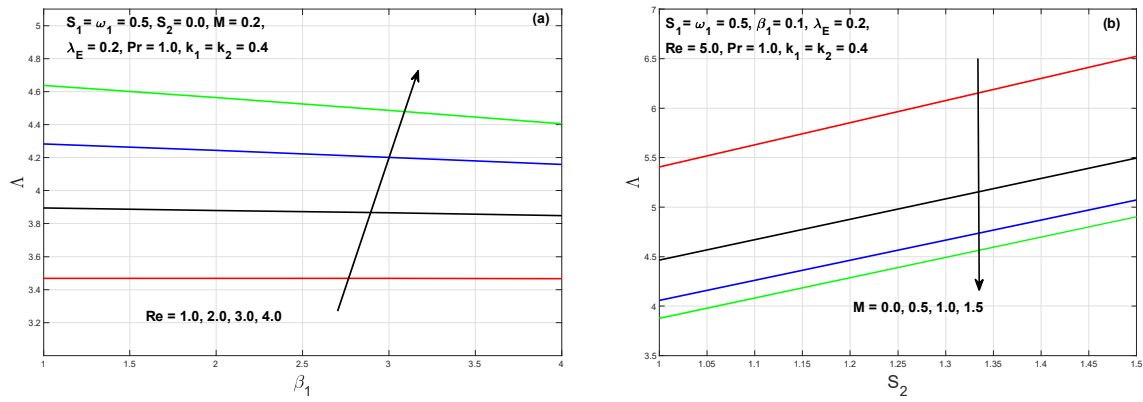
Fig. 9.6: θ for Pr and λ_E .

Fig. 9.7: ϕ for $k_1, \; k_2$ and Sc .

Fig. 9.8: Λ for S_2, M, β_1 and Re.

Chapter 10

Conclusion and Future Work

Over the past few years, there is a remarkable upsurge in the interest to scrutinize the fluid flow and heat transfer of non-Newtonian fluids over a rotating disk. In this thesis, we have formulated the swirling flows of non-Newtonian Maxwell fluid for several various rotating configurations like flow over a single stretchable rotating disk, unsteady thin film flow over a stretchable rotating disk and flow between the regions of two stretchable rotating disks. A special attention has been paid to develop mathematical modelling and numerical solution for Maxwell fluid flow in view of these configurations. Further, the mechanisms of heat and mass transport under numerous physical aspects were also considered. The governing continuity, momentum, temperature and concentrations partial differential equations (PDEs) were reduced into to a set of ordinary differential equations (ODEs) in the framework of suitable similarity transformations. The detail numerical solution procedures to solve the system of nonlinear ordinary differential equations are based on bvp midrich, Runge-Kutta-Felberg (RKF45) and bvp4c schemes in Maple and Matlab. The validity of the obtained results is also assessed by comparing against the results from published literature.

10.1 Concluding Remark

In this chapter, we summarize some of the results obtained in the preceding chapters as follow

- It was noted that with the stronger disk rotation, both the radial and circumferential flows

149

were experienced a dramatic increase due to centrifugal force and as a result the ambient fluid was pumped towards the disk.

- Both the radially outward and tangential flows were decelerated significantly with stronger effects of Deborah number causing to suppress the vertically downward fluid velocity.

- Thermal boundary layer thickness was thinned as the rotation parameter occurred with more intensification.

- The fluid temperature was enhanced with the strengthening of radiation, thermophoresis and Brownian motion parameters.

- The concentration field was boosted with higher effects of thermophoresis parameter while contrary trend was noticed in case of Brownian motion parameter.

- It was observed that the effect of unsteady parameter and Deborah number was to reduce the fluid film thickness whereas it was raised with the increasing impact of rotation parameter.

- By operating the upper disk stretching, the axial flow was observed to change its pattern from lower to upper disk.

- When both the disks were stretched in the same direction of rotation, the pressure profile near the lower disk surface was diminished while at the upper disk an opposite development was observed.

10.2   Future Work

In this work, we have focused on the numerical solution of Maxwell fluid flows over a radially stretching and rotating disk geometries. Although this thesis covers a wide range of aspects of mathematical modeling of Maxwell fluid for rotating disk; however, several area of interest remains unanswered. In the future, the following areas of study to a variety of non-Newtonian fluids may be of interest.

- It could be interesting to develop the mathematical modelling for Maxwell fluid flow over a rotating sphere.

- The Maxwell fluid model can be studied between the gap of a rotating cone and a rotating disk.

- The transient thin flow of Maxwell fluid flow over the rotating cylinder may also be focused in future work.

- Further work could also be done on discovering ways to extend this work to a number of non-Newtonian fluids. For instance, generalized second grade fluid model, Cross fluid model, rate type generalized Burgers fluid model.

- Regarding the solution of the considered problems it may be attractive to study these problems with robust numerical techniques like finite element method, finite volume method and lattice Boltzmann method etc.

Bibliography

[1] J.C. Maxwell, On the dynamical theory of gases, *Phil. Trans. Roy. Soc. London*, **A157** (1867) 49-88.

[2] C. Fetecau and C. Fetecau, A new exact solution for the flow of a Maxwell fluid past an infinite plate, Int. J. Non-Linear Mech., **38** (2003) 423-427.

[3] W. Tan, W. Pan, M. Xu, A note on unsteady flows of a viscoelastic fluid with the fractional Maxwell model between two parallel plates, *Int. J. Non-Linear Mech.*, **38** (2003) 645-650.

[4] M. Jamil and C. Fetecau, Helical flows of Maxwell fluid between coaxial cylinders with given shear stresses on the boundary, *Nonlin. Anal. Real World Appl.*, **5** (2010) 4302–4311.

[5] S. Han, L. Zheng, C. Li and X. Zhang, Coupled flow and heat transfer in viscoelastic fluid with Cattaneo–Christov heat flux model, *App. Math. Lett.*, **38** (2014) 87-93.

[6] M. Mustafa, Cattaneo–Christov heat flux model for rotating flow and heat transfer of upper-convected Maxwell fluid, *AIP Adv.*, **5** (2015) 047109.

[7] J. Sui, L. Zheng and X. Zhang, Boundary layer heat and mass transfer with Cattaneoe Christov double-diffusion in upper-convected Maxwell nanofluid past a stretching sheet with slip velocity, *Int. J. Therm. Sci.*, **104** (2016) 461-468.

[8] A.A. Afify and N.S. Elgazery, Effect of a chemical reaction on magnetohydrodynamic boundary layer flow of a Maxwell fluid over a stretching sheet with nanoparticles, *Particuology*, **29** (2016) 154-161.

[9] Y. Liu, and B. Guo, Coupling model for unsteady MHD flow of generalized Maxwell fluid with radiation thermal transform, *Appl. Math. Mech. -Eng. Edi.*, **37(2)** (2016) 137-150.

[10] L. Cao, X. Si, and L. Zheng, Convection of Maxwell fluid over stretching porous surface with heat source/sink in presence of nanoparticles: Lie group analysis, *Appl. Math. Mech. -Eng. Edi.*, **37(4)** (2016) 433-442

[11] K.L. Hsiao, Combined electrical MHD heat transfer thermal extrusion system using Maxwell fluid with radiative and viscous dissipation effects, *Appl. Therm. Eng.*, **112** (2017) 1281-1288.

[12] R. Jusoh, R. Nazar and I. Pop, Flow and heat transfer of magnetohydrodynamic three-dimensional Maxwell nanofluid over a permeable stretching/shrinking surface with convective boundary conditions, *Int. J. Mech. Sci.*, **124–125** (2017) 166-173.

[13] T.V. Kármán, Uber laminare und turbulente Reibung, *Z. Angew. Math. Mech.*, **1** (1921) 233–252.

[14] I.V. Shevchuk, Convective heat and mass transfer in rotating disk systems, *Springer Verlag, Berlin, Heidelberg*, (2009).

[15] M. Turkyilmazoglu, MHD fluid flow and heat transfer due to a stretching rotating disk, *Int. J. Therm. Sci.*, **51** (2012) 195-201.

[16] A. Ahmadpour, and K. Sadeghy, Swirling flow of Bingham fluids above a rotating disk: An exact solution, *J. Non-Newton. Fluid Mech.*, **197** (2013) 41–47.

[17] S. Xun, J. Zhao, L. Zheng, X. Chen and X. Zhang, Flow and heat transfer of Ostwald-de Waele fluid over a variable thickness rotating disk with index decreasing, *Int. J. Heat Mass Transf.*, **103** (2016) 1214-1224.

[18] I. Mustafa, T. Javed and A. Ghaffari, Heat transfer in MHD stagnation point flow of a ferrofluid over a stretchable rotating disk, *J. Mol. Liq.*, **219** (2016) 526-532.

[19] D.H. Doh and M. Muthtamilselvan, Thermophoretic particle deposition on magnetohydro-dynamic flow of micropolar fluid due to a rotating disk, *Int. J. Mech. Sci.*, **130** (2017) 350-359.

[20] T. Hayat, S. Qayyum, A. Alsaedi and B. Ahmad, Significant consequences of heat generation/absorption and homogeneous-heterogeneous reactions in second grade fluid due to rotating disk, *Res. Phys.*, **8** (2018) 223-230.

[21] T. Hayat, M.W.A. Khan, M.I. Khan and A. Alsaedi, Entropy optimization and Sisko material flow with nonlinear radiative heat flux and heat source/sink, *J. Braz. Soci. Mech. Sci. Eng.*, **40** (2018) 373.

[22] J.A. Khan, M. Mustafa, T. Hayat, and A. Alsaedi, A revised model to study the MHD nanofluid flow and heat transfer due to rotating disk: numerical solutions, *Neur. Comp. Appl.*, **30,** (2018) 957-964.

[23] T. Hayat, S. Ahmad, M.I. Khan and A. Alsaedi, Modeling and analyzing flow of third grade nanofluid due to rotating stretchable disk with chemical reaction and heat source, *Physica B: Conden. Matt.*, **537** (2018) 116-126.

[24] M. Tabassum and M. Mustafa, A numerical treatment for partial slip flow and heat transfer of non-Newtonian Reiner-Rivlin fluid due to rotating disk, *Int. J. Heat Mass Transf.*, **123** (2018) 979-987.

[25] A.C. Emslie, F.D. Bonner and L.G. Peck, Flow of a viscous liquid on a rotating disk, *J. Appl. Phys.*, **29** (1958) 858–862.

[26] B.G. Washo, Rheology and modeling of the spin coating process, *IBM J. Res. Dev.,* **21** (1977) 190-198 .

[27] S.A. Jenekhe, Effects of solvent mass transfer on flow of polymer solutions on a flat rotating disk, *Ind. Eng. Chem. Fundam.*, **23** (1984) 425-432.

[28] W.W. Flack, D.S. Soong, A.T. Bell and D.W. Hess, A mathematical model for spin coating of polymer resists, *J. Appl. Phys.*, **56,** (1984) 1199.

[29] C.Y. Wang, L.T. Watson and K.A. Alexander, Spinning of a liquid film from an accelerating disc, *IMA J. Appl. Math.*, **46** (1991) 201-210.

[30] H.I. Andersson, B. Holmedal, B.S. Dandapat and A.S. Gupta, Magnetohydrodynamic melting flow from a horizontal rotating disk, *Math. Models Methods Appl. Sci.,* **3** (1993) 373-393.

[31] M. Kumari and G. Nath, Unsteady MHD film flow over a rotating infinite disk, *Int. J. Eng. Sci.,* **42** (2004) 1099-1117.

[32] B.S. Dandapat, S. Maity and S.K. Singh, Two-layer film flow on a rough rotating disk in the presence of air shear, *Acta. Mech.,* **228** (2017) 4055–4065.

[33] G.K. Batchelor, Note on a class of solutions of the Navier-Stokes equations representing steady rotationally symmetric flow, *Q. J. Mech. Appl. Math.,* **4** (1951) 29-41.

[34] G.N. Lance and M.H. Rogers, The axially symmetric flow of a viscous fluid between two infinite rotating disks, *Proc. R. Soc. A.,* **266** (1962) 109-121.

[35] M. Turkyilmazoglu, Flow and heat simultaneously induced by two stretchable rotating disks, *Phys. Fluids,* **28** (2016): 043601.

[36] T. Hayat, S. Qayyum, M. Imtiaz, F. Alzahrani and A. Alsaedi, Partial slip effect in flow of magnetite-Fe_3O_4 nanoparticles between rotating stretchable disks, *J. Magn. Magn. Mat.,* **413** (2016) 39-48.

[37] T. Hayat, S. Qayyum, M. Imtiaz and A. Alsaedi, Homogeneous-heterogeneous reactions in nonlinear radiative flow of Jeffrey fluid between two stretchable rotating disks, *Res. Phy.,* **7** (2017) 2557-2567.

[38] A. Das and B. Sahoo, Flow and heat transfer of a second grade fluid between two stretchable rotating disks, *Bull. Braz. Math. Soc., New Series,* **49** (2018) 531–547.

[39] P. Keblinski, J.A. Eastman and D.G. Cahill, Nanofluids for thermal transport, *Mater. Today,* **8** (2005) 36–44.

[40] M. Salavati-Niasari, P. Salemi and F. Davar, Oxidation of cyclohexene with *tert*-butylhydroperoxide and hydrogen peroxide catalysted by Cu(II), Ni(II), Co(II) and Mn(II) complexes of N,N$^/$ -bis-(α-methylsalicylidene)-2,2-dimethylpropane-1, 3-diamine, supported on alumina, *J. Mol. Catal. A: Chem.,* **238** (2005) 215-222.

[41] M. Salavati-Niasari, Nanoscale microreactor-encapsulation of 18-membered decaaza macro-cycle nickel(II) complexes, *Inorg. Chem. Commun.,* **8** (2005) 174-177.

[42] F. Mohandes and M. Salavati-Niasari, Sonochemical synthesis of silver vanadium oxide micro/nanorods: Solvent and surfactant effects, *Ultras. Sonochem.*, **20** (2013) 354-365.

[43] G. Kianpour, M. Salavati-Niasari and H. Emadi, Sonochemical synthesis and characterization of NiMoO$_4$ nanorods, *Ultras. Sonochem.*, **20** (2013) 418-424.

[44] A. Trokhmchuk, D. Henderson, A. Nikolov and D.T. Easan, A simple calculation of structural and depletion forces for fluids/suspensions confined in a film, *Langmuir*, **17** (2001) 4940-4947.

[45] S. Biswas, S. Gawande, V. Bromberg and Y. Sun, Deposition dynamics of inkjetprinted colloidal drops for printable photovoltaics fabrication, *J. Sol. Energy Eng.*, **132** (2010) 021010.

[46] A.S. Joshi and Y. Sun, Wetting dynamics and particle deposition for an evaporating colloidal drop: a lattice Boltzmann study, *Phys. Rev. E*, **82** (2010) 041401.

[47] S.U.S. Choi, Enhancing thermal conductivity of fluids with nanoparticles, *ASME Fluids Eng. Div.*, **231** (1995) 99-106.

[48] J. Buongiorno, Convective transport in nanofluids, *ASME J. Heat Transf.*, **128** (2006) 240-250.

[49] R.K. Tiwari and M.K. Das, Heat transfer augmentation in a two-sided lid-driven differentially heated square cavity utilizing nanofluids, *Int. J. Heat Mass Transf.*, **50** (2007) 2002-2018.

[50] A.V. Kuznetsov and D.A. Nield, Natural convective boundary-layer flow of a nanofluid past a vertical plate, *Int. J. Therm. Sci.*, **49** (2010) 243-247.

[51] H.F. Oztop and E.A. Nada, Numerical study of natural convection in partially heated rectangular enclosures filled with nanofluids, *Int. J. Heat Fluid Flow*, **29** (2008) 1326-1336.

[52] Y. Lin and Y. Jiang, Effects of Brownian motion and thermophoresis on nanofluids in a rotating circular groove: A numerical simulation, *Int. J. Heat Mass Transf.*, **123** (2018) 569-582.

[53] J.B.J. Fourier, Théorie Analytique De La Chaleur, Paris, 1822.

[54] C. Cattaneo, Sulla conduzionedelcalore, *Atti Semin. Mat. Fis. Univ. Modena Reggio Emilia*, **3** (1948) 83-101.

[55] C.I. Christov, On frame indifferent formulation of the Maxwell–Cattaneo model of finite-speed heat conduction, *Mech. Res. Commun.*, **36** (2009) 481-486.

[56] M. Ciarletta and B. Straughan, Uniqueness and structural stability for the Cattaneo–Christov equations, *Mech. Res. Commun.*, **37** (2010) 445-447.

[57] S. Han, L. Zheng, C. Li and X. Zhang, Coupled flow and heat transfer in viscoelastic fluid with Cattaneo–Christov heat flux model, *Appl. Math. Lett.*, **38** (2014) 87-93.

[58] M. Mustafa, Cattaneo-Christov heat flux model for rotating flow and heat transfer of upper-convected Maxwell fluid, *AIP Adv.*, **5** (2015) 047109.

[59] T. Hayat, S. Ali, A. Alsaedi and H.H. Alsulami, Influence of thermal radiation and Joule heating in the Eyring–Powell fluid flow with the Soret and Dufour effects, *J. Appl. Mech. Tech. Phys.*, **57** (2016) 1051-60.

[60] T. Hayat, R.S. Saif, R. Ellahi, T. Muhammad and B. Ahmad, Numerical study for Darcy–Forchheimer flow due to a curved stretching surface with Cattaneo–Christov heat flux and homogeneous– heterogeneous reactions, *Res. Phys.*, **7** (2017) 2886-92.

[61] V. Nagendramma, C.S.K. Raju, B. Mallikarjuna, S.A. Shehzad and A. Leelarathnam, 3D Casson nanofluid flow over slendering surface in a suspension of gyrotactic microorganisms with Cattaneo-Christov heat flux, *Appl. Math. Mech. -Engl. Ed.*, **39** (2018) 623-638.

[62] S.Z. Alamri, A.A. Khan, M. Azeez and R. Ellahi, Effects of mass transfer on MHD second grade fluid towards stretching cylinder: a novel perspective of Cattaneo–Christov heat flux model, *Phy. Lett A.*, **383** (2019) 276-81.

[63] K. Loganathan, S. Sivasankaran , M. Bhuvaneswari and S. Rajan, Second-order slip, cross-diffusion and chemical reaction effects on magneto-convection of Oldroyd-B liquid using Cattaneo–Christov heat flux with convective heating, *J. Therm. Anal. Calorim.*, **136** (2019) 401–409.

[64] A.A. Khan, S.R. Bukhari, M. Marin and R. Ellahi, Effects of chemical reaction on third-grade MHD fluid flow under the influence of heat and mass transfer with variable reactive index, *Heat Transf. Res.*, **50** (2019)1061–80.

[65] B. Ramadevi , K.A. Kumar, V. Sugunamma , J.V.R. Reddy and N. Sandeep, Magneto-hydrodynamic mixed convective flow of micropolar fluid past a stretching surface using modified Fourier's heat flux model, *J. Therm. Anal. Calorim.*, **139** (2020) 1379–1393.

[66] H. Taheri , Y Shekari and A. Tayebi, Numerical investigation of non-Fourier natural convection of Newtonian nanofluids, *J. Therm. Anal. Calorim.*, **135** (2019) 1921–1929.

[67] A. Zeeshan, N. Shehzad and R. Ellahi, Analysis of activation energy in Couette–Poiseuille flow of nanofluid in the presence of chemical reaction and convective boundary conditions, *Res. Phys.,* **8** (2018) 502-12.

[68] M.A. Chaudhary and J.H. Merkin, A simple isothermal model for homogeneous heterogeneous reactions in boundary layer flow: I. Equal diffusivities, *Fluid Dyn. Res.*, **16,** (1995) 311–333.

[69] J.H. Merkin, A model for isothermal homogeneous-heterogeneous reactions in boundary layer flow, *Math. Comput. Model.*, **24** (1996) 125–136.

[70] W.A. Khan and I. Pop, Effects of homogeneous-heterogeneous reactions on the viscoelastic fluid towards a stretching sheet, *ASME J. Heat Transf.*, **134** (2012) 1–5.

[71] Z. Abbas, Z. Abbas, M. Sheikh and I. Pop, Stagnation-point flow of a hydromagnetic viscous fluid over stretching/shrinking sheet with generalized slip condition in the presence of homogeneousheterogeneous reactions, *J. Taiw. Inst. Chem. Eng.*, **55** (2015) 69–75.

[72] M. Khan, L. Ahmad, W.A. Khan, A.S. Alshomrani, A.K. Alzahrani and M.S. Alghamdi , A 3D Sisko fluid flow with Cattaneo-Christov heat flux model and heterogeneous-homogeneous reactions: A numerical study, *J. Mol. Liq.*, **238** (2017) 19–26.

[73] A. Rauf, Z. Abbas, S.A. Shehzad, A. Alsaedi and T. Hayat, Numerical simulation of chemically reactive Powell-Eyring liquid flow with double diffusive Cattaneo-Christov heat and mass flux theories, *Appl. Math. Mech. -Eng. Edi.*, **39(4)** (2018) 467–476.

[74] Hashim, M. Khan, A.S. Alshomrani and R.U. Haq, Investigation of dual solutions in flow of a non-Newtonian fluid with homogeneous–heterogeneous reactions: Critical points, *Eur. J. Mechanics / B Fluids*, **68** (2018) 30–38.

[75] L.F. Shampine, I. Gladwell and S. Thompson, Solving ODEs with MATLAB, (Ist Edn.), Cambridge University Press, Cambridge, 2003.

Turnitin Originality Report

Flow and Heat Transfer of Non-Newtonian Maxwell Fluid over a Stretchable Rotating Disk by Jawad Ahmed .
From DRSM (DRSM L)

- Processed on 09-Nov-2020 12:31 PKT
- ID: 1440576262
- Word Count: 42724

Similarity Index
16%
Similarity by Source
Internet Sources:
11%
Publications:
11%
Student Papers:
5%

sources:

1

< 1% match (Internet from 03-Oct-2019)
https://link.springer.com/article/10.1007%2Fs10483-018-2368-9

2

< 1% match (Internet from 30-Oct-2020)
https://www.nature.com/articles/s41598-020-61172-2?code=a55065a0-bf15-4704-babb-e71a20b10ced&error=cookies_not_supported

3

< 1% match (publications)
Hashim, Masood Khan, Ali Saleh Alshomrani, Rizwan Ul Haq. "Investigation of dual solutions in flow of a non-Newtonian fluid with homogeneous–heterogeneous reactions: Critical points", European Journal of Mechanics - B/Fluids, 2018

4

< 1% match (Internet from 06-Sep-2010)
http://www.lec.csic.es/~julyan/papers/rkpaper/node4.html

5